

RICE UNIVERSITY

**A Multi-Scale Approach to Study Silicate
Dissolution: Kinetic Monte Carlo Simulations
and Experimental Observations**

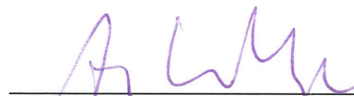
by

Inna Kurganskaya

A THESIS SUBMITTED
IN PARTIAL FULFILLMENT OF THE
REQUIREMENTS FOR THE DEGREE

Doctor of Philosophy

APPROVED, THESIS COMMITTEE:



Andreas Luttge, Chair
Professor, Earth Science and
Professor, Chemistry



Dale Sawyer, Professor, Earth
Science



Kenton H. Whitmire, Professor,
Chemistry



Rajdeep Dasgupta, Associate
Professor, Earth Science

HOUSTON, TEXAS
AUGUST 2013

ABSTRACT

A Multi-Scale Approach to Study Silicate Dissolution: Kinetic Monte Carlo Simulations and Experimental Observations

by

Inna Kurganskaya

Dissolution of silicate minerals is an important part of many geological processes taking place on the Earth's surface as well as in the deep crust. Weathering of rocks and soil formation, metasomatic rock alteration by hydrothermal fluids, and diagenetic transformation of sediments are all controlled by dissolution reactions. Secondary pore space of natural reservoirs can be significantly changed by dissolution and subsequent precipitation of clay minerals. As a consequence, the potential capacity for storage of natural fuels, carbon dioxide or radioactive waste, can be affected. In addition, the stability of rocks hosting potentially hazardous materials largely depends on their dissolution rates.

The development of computational *ab initio* and Molecular Dynamics techniques permits study of dissolution reactions at the molecular scale. At the same time, advanced microscopic techniques allow the study of dissolution process at the nm to micron scale and investigation of spatial and temporal variations of surface reactivity. The combination of these methods has strong potential for tackling fundamental questions of the mechanisms of mineral dissolution.

This thesis presents an integrated, multi-scale approach to the study of silicate dissolution. The work consists of three main parts: experimental studies of the dissolving

mineral surface at the micron scale, Kinetic Monte Carlo (KMC) simulations at the nanometer scale, and the parameterization of KMC models by *ab initio* derived activation energies. Muscovite mica and quartz were chosen as study materials. These two minerals represent “2-dimensional” (phyllosilicates) and 3-dimensional (tectosilicates) structural templates of silicates as well as “complex” and “simple” chemical bond networks.

The first part of my muscovite dissolution studies is based on experimental observations of the reacted surface with vertical scanning interferometry. This approach was used to quantify the distribution of surface reactivity in terms of surface roughness and mean height levels, and also measure the dissolution rate. Additional investigations of the detailed surface structure were done using the AFM. KMC simulations of muscovite dissolution constitute the second part of this work. I developed KMC models that simulate the dissolution of mica structures. By varying the number of the basic reaction types in the system, a satisfactory match was achieved between modeling results and experimental observations. These results show how KMC methods can be used as a tool for testing hypotheses regarding the role of surface reactions on the overall reaction mechanism.

The third part of the work is dedicated to the problems of complexity and parameterization of KMC models. Four models of quartz dissolution of varying complexity are presented. The capabilities of the models to predict experimentally observed dissolution features were shown for prismatic, rhombohedral, and pinacoid quartz faces. These simulation results demonstrate the basic role of topology in the recognition of key surface sites, and are used to derive basic dissolution mechanisms for the three faces.

Acknowledgments

The entire work of this thesis would have been less successful were it not for the help and support of many people accompanying me through my PhD studies. I am very grateful to my advisor, Dr. Andreas Lutge for his constant moral support and intellectually stimulating scientific discussions about various aspects of crystal dissolution kinetics. His wide interdisciplinary background in both earth science and chemistry provided me with a great and extremely valuable research experience. Much of my research progress was strongly guided by his detailed and profound feedback to my work, studies and papers. He also taught me a lot about the pedagogical process in geological sciences during my work as a teaching assistant for his Earth Science 101 class.

I am very thankful to Dr. Rolf Arvidson, who introduced me to the details of designing and setting up laboratory experiments and performing optical interferometry measurements, encouraged my scientific curiosity in testing important kinetic problems both in the laboratory and as computational experiments, became a dedicated co-author of my first paper and carefully read all other papers and parts of this thesis. I enjoyed a lot by our long-hour discussions about a wide range of topics, from the fundamental problems of crystal dissolution and statistical physics to the problem of Universe formation.

Warm thanks go to Dr. Cornelius Fischer for his comments to my papers, supportive discussions and e-mails. His amazing knowledge of very complex prob-

lems in mineral dissolution kinetics and profound feedbacks to my work has helped me a lot.

I also would like to thank my committee members, Dr. Julia Morgan (Earth Science), Dr. Rajdeep Dasgupta (Earth Science), Dr. Dale Sawyer (Earth Science), and Dr. Kenton Whitmire (Chemistry), for their interest in my work, discussions and questions at annual research progress meetings, qualifying exams and thesis defense.

Special thanks are dedicated to James Keenan, Emily Chin, Dr. Glenn Snyder and Clint Miller for their proofreading of my papers and making corrections to English and writing style. My office mates, Lizette Leon-Rodrigues, Fernando Mazuera, James Keenan, Tao Kai and Guangchi Xing, became my heart-and-soul friends, and provided me with constant moral support, always cheered me up and became role models both as scientists and friends. I am also very thankful to my peers, graduate and undergraduate Earth Science students, who were interested in my studies, attended my presentation and thesis defense, and spent our happy after-work time with me.

My family always provided me with strong emotional support during all my studies. I am especially thankful to my sister, Yana Alexandrovna Pakulina, and to her husband, Kirill Olegovich Pakulin, for their warm and supportive words that I constantly received from them during the all hard times. My parents, Tatiana Yurievna Kurganskaya and Alexandr Alexandrovich Kurganskiy, were always role

models for me, as parents, friends and dedicated professionals, and thus I am dedicate this thesis to them.

I acknowledge the generous financial support from the Global Climate and Energy Project (GCEP) at Stanford University (award # 25580430-48513-A), grant #R64070, Earth Science Department at Rice University for the first-semester tuition waiving and providing me with Teaching Assistantship position, MURI grant #R7B861 and DOE grant #117372 that supported my first laboratory experiments.

Contents

Acknowledgments	iii
Contents.....	vi
List of Figures	ix
List of Tables	xvi
List of Equations.....	xviii
List of symbols and abbreviations.....	xx
Introduction	1
1.1. References	7
Does the stepwave model predict mica dissolution kinetics?.....	12
2.1. Abstract.....	13
2.2. Introduction	14
2.3. Methods.....	16
2.4. Results.....	18
2.4.1. VSI data of etch pit populations	18
2.4.2. VSI Data: Dissolution Rates	25
2.4.3. AFM Data.....	25
2.5. Discussion	26
2.5.1. Etch Pit Morphology, Structure, and Distribution	27
2.5.2. Distribution of dissolution rates and their control by the phyllosilicate structure.....	30
2.5.3. Application of the stepwave model.....	34
2.6. Summary.....	36
2.7. Acknowledgements	37
2.8. References	37
A comprehensive stochastic model of phyllosilicate dissolution: structure and kinematics of etch pits formed on muscovite basal face	45
3.1. Abstract.....	46
3.2. Introduction	47

3.3. Methods.....	52
3.3.1. Crystal chemistry of sheet silicates.....	53
3.3.2. Kinetic models of mica dissolution	56
3.3.2.1. Basic equations and model assumptions.....	56
3.3.2.2. First coordination sphere (FCS): lattice resistance effect.....	60
3.3.2.3. Second coordination sphere (SCS) influence	61
3.3.2.4. Corrections for Al-O-(H)-Al or hydroxyl accessibility.....	63
3.3.2.5. Lattice defects	64
3.3.2.6. System size	65
3.3.2.7. Simulation algorithm	66
3.3.3. Model parameterization by experimental data	68
3.4. Results.....	71
3.4.1. Etch pit structure: general features.....	72
3.4.1.1. Monolayer pits	72
3.4.1.2. Multilayer pits	74
3.4.2. Step morphology, orientation and stability	79
3.4.2.1. First coordination sphere level of complexity	79
3.4.2.2. Second coordination sphere level of complexity.....	81
3.5. Discussion	82
3.5.1. {hk0} face stability.....	82
3.5.2. Topology of ledge and kink sites	83
3.5.3. Morphology of etch pits.....	89
3.5.4. Applications of the KMC model.....	90
3.6. Conclusions	91
3.7. Acknowledgements	92
3.8. References	93
Kinetic Monte Carlo simulations of silicate dissolution: model complexity and parameterization	102
4.1. Abstract.....	103
4.2. Introduction	104
4.3. Kinetic Monte Carlo models	109
4.3.1. The First Coordination Sphere (FCS) Model.....	110
4.3.2. The Second Coordination Sphere (SCS) Models.....	111

4.3.2.1. Linear Approximation 1 (SCS-L1) model	114
4.3.2.2. Linear Approximation 2 (SCS-L2) Model	114
4.3.2.3. The “Direct” Parameterization (SCS-D) Model	116
4.3.2.4. Model parameters	116
4.3.3. Surface stabilization and relaxation effects	118
4.4. Results and discussion	120
4.4.1. Pinacoid (001) face.....	121
4.4.1.1. Surface morphologies	121
4.4.1.2. Etch pit structure	124
4.4.1.3. Surface stabilization effects: etch pits and hillocks.....	125
4.4.2. Rhombohedral (101) face.....	128
4.4.2.1. Surface structure	128
4.4.2.2. Hollow cores and etch tubes.....	132
4.4.2.3. Dissolution mechanism: 2D and 3D stepwave movement.....	132
4.4.3. Prism (100) face	134
4.4.3.1. Dissolution scenario I: striations	134
4.4.3.2. Dissolution scenario II: rectangular stepwaves.....	135
4.4.3.3. Surface stabilization effect: dissolution scenario III.....	138
4.4.4. Model complexity: conclusions and prospective	142
4.5. Conclusions	147
4.6. Acknowledgements	147
4.7. References	148
Summary and Conclusions	156
5.1. References	162

List of Figures

Figure 2-1. VSI data for muscovite (001) surface. (A) 189×189 μm field of view showing irregular etch pit distributions after 360 hours of reaction. (B) Inset area (35 × 35 μm) from A showing submicron-sized pits appearing after 220 hours together with larger earlier-formed coalescent pits. (C) An area (69 × 69 μm) at the 100 h time step showing formation of pit chains and trenches. (D) An area (135 × 135 μm) characterized by formation of linear structures. The lines are oriented in two principal directions intersecting at 120°.....19

Figure 2-2. Evolution in frequency distributions of roughness (A) and height (B) from time steps t_1 to t_6 (initial condition = t_0). Insets show expanded detail of complex changes involving nucleation and growth of etch pits. See text for discussion.....20

Figure 2-3. Determination of dissolution rates from VSI data. (A) Etch pit (dia. ~ 4 μm) formed through probable coalescence of individual pits (10 × 10 μm field of view). (B) Time series of cross sections through red line at A. (C) Boundary of temporarily masked (upper left) and permanently exposed (lower right) regions (189 × 189 μm field of view) used to calculate normal surface retreat. Left side had been masked between 220 and 500 hours of experiment. (D) Cross section through the area shown on (C).....21

Figure 2-4. AFM data of muscovite (001) surface, 500 h. (A) Note common shape and orientation of etch pits; (B) Etch pit penetrating five layers showing irregular,

curved step of shallowest layer and hexagonal outlines of deeper layers; (C) Etch pit structure: profile C1 traverses zigzag steps (see text), profile C2 traverses parallel steps; (D) Detail of central pit in (A), showing opening of new pit in bottommost layer (arrow).....23

Figure 2-5. AFM image of muscovite (001) surface after 500 h showing etch pit development.....24

Figure 2-6. Schematic illustration of stepwave formation on muscovite {001} surface. (A) Consecutive steps moving outwards from a dislocation center. (B) Steps emanating from two major etch pits (linear defects) and surrounding monolayer pits (point defects) form a single stepwave of complex morphology. (C) Multilayer etch pit formation, showing layer-by-layer dissolution in two principal directions.....33

Figure 3-1. Crystal chemistry of muscovite. (a) Polyhedral model of muscovite structure. (b) Bridging bonds in muscovite lattice: Al(T)-O-Si(T), Si(T)-O-Si(T), Si(T)-O-Al(O), Al(T)-O-Al(O) and Al(O)-O-Al(O).....55

Figure 3-2. Second order coordination spheres for tetrahedral (a,b) and octahedral (c,d) reactive centers. (a) Tetrahedral sphere for tetrahedral center. (b) Octahedral sphere for tetrahedral center. (c) Tetrahedral sphere for octahedral center. (d) Octahedral sphere for octahedral center.....62

Figure 3-3. Geometric accessibility of basal plane hydroxyls (red spheres represent H-atoms): a semi-transparent circle refers to a “hardly accessible” state; an

open circle refers to an “accessible” state. (a) Polyhedral representation. (b) “Ball and stick” model.....64

Figure 3-4. An illustration to Kinetic Monte Carlo algorithm. (a) Dissolution probabilities assigned to the different surface sites of muscovite. (b) Schematic structure of the probability interval used to make a decision about reaction type selection. The length of an each subinterval corresponds to P_i probability value. A random number $0 < x < 1$ falling into subinterval P_i defines a reaction type i to happen at the given iteration step.....67

Figure 3-5. Two principal orientations of monolayer etch pits. (a) Experimentally obtained AFM data (Kurganskaya et al., 2012). Blue arrows show main pit orientations. Red lines refer to etch pit profiles A1-A2, A3-A4 and A5-A6 shown on (d). (b) Contours of etch pits obtained in KMC simulations: pits of the upper type appear in the 1st type of TOT layer; pits of the lower type appear in the 2nd type of TOT layer (SFCS version of model is used, energetic parameters are shown in Table 3-3). (c) Models of the two TOT layers in muscovite structure. Red arrows show directions of the fastest etch pit growth. (d) Profiles through the three pits shown on (a), letters A1-A6 mark the ends of the profiles.....73

Figure 3-6. Etch pit morphology with (b) and without (a) $\text{Al(O)}=\text{O}=\text{Al(O)}$ bond orientation corrections (see in text). Activation energy parameters ($\Delta E_a/kT$) are provided in Table 3-3. (a) The result of the KMC simulation without “hydroxyl orientation” corrections (SFCS version). The geometric center of the pit matches to the dislocation core position. (b) KMC simulation result for SFCS-H version. (c) A colormap of a

two-layered etch pit on muscovite (001) face dissolved in water with pH=9.4, T=155°C (AFM data, Kurganskaya et al., 2012). White line marks C1-C2 profile through the pit.....75

Figure 3-7. Zigzag pattern formed on the muscovite (001) face. (a),(b) Patterns observed on the muscovite surface dissolved in water (pH=9.4; T=155°C, Kurganskaya et al., 2012). (c) An etch pit with the four zigzag patterns produced in KMC simulations of muscovite dissolution (SCS-H version). Activation energies for bond breaking, second order neighbor and hydroxyl orientation corrections are presented in Table 4, the first order corrections are $\Delta E^{1_{T-T}}/kT = 6$, $\Delta E^{1_{T-O}}/kT = 6$, $\Delta E^{1_{O-T}}/kT = 6$, $\Delta E^{1_{O-O}}/kT = 4$. (d) Enlarged inset of the rectangular area shown on (c). (e) Zigzag pattern with curved steps obtained in KMC simulations (enlarged inset from Fig. 3-9a). Parameter values for this simulation are shown in Table 3-4.....77

Figure 3-8. Etch pits obtained in KMC simulations (FCS-H version) (a) Structure of an etch pit produced with SFCS-H version; (b) A pit produced with the same parameters using WFCS-H version. (c) Inset from Fig. 3-8b showing detailed step morphology. Modeling parameters are shown in Table 3-3.....80

Figure 3-9. Morphology of a multilayer pit growing on muscovite (001) face. (a) A polygonal etch pit produced in KMC simulations (SCS-H version), see Table 3-4 for energetic parameters. (b) A mul-tilayer etch pit obtained from experiments (AFM data, Kurganskaya et al., 2012). White line marks B1-B2 etch pit profile.....82

Figure 3-10. Ledge (step) and kink sites at (110), (11 $\bar{0}$), and (100) faces of muscovite. The example sites are labeled by semitransparent squares, yellow and red for

the kink sites, light gray for the ledge sites. The front kink sites are labeled as k_1 , the back kink sites are labeled as k_2 . (a) Tetrahedral sites. Upper kink sites are highlighted by yellow squares, lower kink sites are highlighted by red squares. (b) Octahedral sites.....85

Figure 4-1. Differentiation of the Si (N_1, N_2, N_3) reactive sites (red circles) on the quartz surface used in KMC models. Only Si atoms are shown. N_1 is the number of first order Si-O-Si neighbors, N_2 and N_3 are the numbers of second-order “connected” and “disconnected” (green circle) neighbors. (A) and (B) show the difference between “connected” and “disconnected” neighbors, (C) and (D) illustrate two possible bond configurations for a (2,4,0) site. (A) (2,6,0) site ; (B) (2,6,1) site; (C) Q2-Q4;Q2-Q2 configuration ; (D) Q2-Q3;Q2-Q3 configuration.....112

Figure 4-2. KMC simulation of a dissolving (001) quartz face in pure water, neutral pH, $T = 25^\circ\text{C}$ (modeling parameters are shown in Table 4-1, a single screw dislocation intersects the surface at the center). Results from: (A) the FCS model; (B) the SCS-L1 model; (C) the SCS-L2 model ($\Delta E_{2g} = 0 \text{ kT}$), and (D) the SCS-L2 model ($\Delta E_{2g} = 2 \text{ kT}$); (E) the SCS-L2 model ($\Delta E_{2g} = 4 \text{ kT}$); (F) the SCS-D model ($\Delta E_{2g} = 0 \text{ kT}$); (G) the SCS-D model ($\Delta E_{2g} = 2 \text{ kT}$); (H) SCS-D model ($\Delta E_{2g} = 4 \text{ kT}$); in case of I and J the surface is stabilized by adding weight coefficients to the terrace sites (S1 method); (I) SCS-D ($\Delta E_{2g} = 0 \text{ kT}$; S1); (J) SCS-D ($\Delta E_{2g} = 2 \text{ kT}$; S1) model.....122

Figure 4-3. (A)-(E): KMC simulations of the formation and dissolution of quartz hillocks starting from a “frozen” (stabilized) (001) face of quartz. The SCS-L2 ($\Delta E_{2g} = 0 \text{ kT}$) model is used for this illustration, 5 screw dislocations parallel to the c^* axis

intersect the starting surface. A $(\text{SiO}_4)^{4-}$ -group is removed from the surface during each iteration. (A) $8 \cdot 10^6$ iterations; (B) $16 \cdot 10^6$ iterations; (C) $24 \cdot 10^6$ iterations; (D) $32 \cdot 10^6$ iterations; (E) $40 \cdot 10^6$ iterations. (F)* Hillocks formed on a dissolving quartz surface observed in experiments by Neumann and Lutge (1995).....126

Figure 4-4. (A)-(C): Results of KMC simulations: Etch pits formed on the rhombohedral (101) quartz face in pure water, neutral pH, $T = 25^\circ\text{C}$ (energetic parameters are shown in Table 4-1) (blue highlights (3,7) sites), subfigures labeled by “1” present the front views, subfigures labeled by “2” present the side views with hollow cores. (A) Surface produced by using the FCS model, 10^6 molecules removed; (B) A pentagonal pit developed at the junction between the triangular pit and the hollow core, SCS-D ($\Delta E_{2g} = 0$) model, $2 \cdot 10^6$ molecules removed. (C) Polygonal pits formed at the walls of the original triangular pit, SCS-L2 ($\Delta E_{2g} = 0$) model; $12 \cdot 10^6$ molecules removed. (D)* Triangular pits observed on the surface of naturally weathered quartz grains (Brantley et al., 1986). (E)** Polygonal etch pits observed on rhombohedral quartz surface etched by KOH (Patel et al., 1965).....130

Figure 4-5. (A)-(D): Structures of the dissolving (100) prism face of quartz obtained from KMC simulations (starting from Q3 termination; pure water, neutral pH, $T=25^\circ\text{C}$, parameters are shown in Table 4-1). Label “1” refers to the front view, label “2” refers to the side view with the etch tubes. (A)-(C)- Surfaces simulated using SCS-D ($\Delta E_{2g} = 0$) model (blue highlights (3,7) sites)), (A) Etch pit opening at the beginning of the simulation (10^4 molecules removed). (B) “Striations” and V-shaped pits appeared at a later stage of the simulation (10^6 molecules removed). (C) The

same surface with developed V-shaped pits and rhombohedral faces, $6 \cdot 10^6$ molecules removed. (D) The surface obtained by using SCS-L2 ($\Delta E_{2g} = 4$ kT units) model, with the surface stabilization effect (S2 method) and parameter values $\Delta E_1=20$ kJ/mol, $\Delta E_{21}=1$ kJ/mol; $\Delta E_{2g} = 10$ kJ/mol. (E)* Striations formed on the quartz surface dissolved at hydrothermal conditions. The face and direction could not be identified (Luttge, 1995).....136

Figure 4-6. (A)-(N): KMC simulations: Etch pits formed at a (100) prism face (starting from Q_2 termination, top layer is frozen, 10^6 atoms removed in each case, the length of the screw dislocation hollow core is 200 unit cells). A-H: "Pure water", various models used (see text); (A) FCS model; (B) SCS-L1 model; (C) SCS-L2 model ($\Delta E_{2g} = 0$ kT); (D) SCS-L2 model ($\Delta E_{2g} = 6$ kT) model; (E) SCS-L2 model ($\Delta E_{2g} = 10$ kT); (F) SCS-D model ($\Delta E_{2g} = 0$ kT); (G) SCS-D model ($\Delta E_{2g} = 2$ kT); (H) SCS-L2 model ($\Delta E_{2g} = 4$ kT); I-N: low activation energy, or "catalyzing" environment, various models used. (I) FCS model; (J) SCS-L1 model; (K) SCS-L2 model ($\Delta E_{2g} = 0$ kT); (L) SCS-L2 model ($\Delta E_{2g} = 2$ kT); (M) SCS-L2 model ($\Delta E_{2g} = 4$ kT); (N) SCS-L2 model ($\Delta E_{2g} = 6$ kT); (O)* Rectangular-pyramidal pits formed on the prism faces of quartz etched by KOH (Gratz et al., 1990).....139

List of Tables

Table 2-1. Roughness parameters. Properties (p) computed as weighted means, $\sum (n \times p)_i / \sum n_i$ in nm.....	24
Table 3-1. Basic types of bridging bonds in phyllosilicate structures.....	54
Table 3-2. Numbers of dissolution rate coefficients for different elements in four layered silicates.....	59
Table 3-3. Energetic parameters used in the First Coordination Sphere (FCS) complexity level of the KMC model.....	70
Table 3-4. Energetic parameters used in SCS complexity level of the KMC model.....	71
Table 3-5. Coordination numbers for the muscovite “kink” and “step” sites shown on Fig. 3-10. The numbers are shown in order NT1,NO1,NT2, NO2, or the number of first tetrahedral nearest neighbors, the number of first octahedral nearest neighbors, the number of second tetrahedral neighbors and the number of the second octahedral neighbors correspondingly.....	86
Table 4-1. Activation energies of bond hydrolysis and other energetic parameters used in the KMC models, in [kJ/mole].....	118
Table 4-2. Morphological characteristics (shape and composing faces) of polyhedral etch pits formed on Q2 termination of prism (100) quartz face in KMC simulations. The initial surface was stabilized by S2 method (see description in text), mod-	

eling parameters are shown in Table 1. R-rhombohedral; m-prism faces (a) “pure water” conditions; (b) “catalyzing” conditions.....142

List of Equations

Equation 2-1.....	32
Equation 3-1.....	56
Equation 3-2.....	56
Equation 3-3.....	57
Equation 3-4.....	57
Equation 3-5.....	57
Equation 3-6.....	58
Equation 3-7.....	58
Equation 3-8.....	60
Equation 3-9.....	60
Equation 3-10.....	60
Equation 3-11.....	61
Equation 3-12.....	61
Equation 3-13.....	61
Equation 3-14.....	62
Equation 3-15.....	64

Equation 3-16.....66

Equation 3-17.....67

Equation 3-18.....68

Equation 4-1.....110

Equation 4-2.....110

Equation 4-3.....111

Equation 4-4.....114

Equation 4-5.....115

Equation 4-6.....116

List of symbols and abbreviations

Eq(s).	Equation(s)
Fig(s).	Figure(s)
VSI	Vertical Scanning Interferometry
AFM	Atomic Force Microscopy
HF(1)	Hartree-Fock
HF(2)	hydro-fluoric acid
MP[2]	Møller-Plesset
DFT	Density functional theory
KMC	Kinetic Monte Carlo
BET	Brunauer-Emmett-Teller
BCF	Burton-Cabrera-Frank
Sq	surface root mean square roughness
t0-t6	time steps
h(1)	hours
h(2)	height
T(1)	temperature
T(2)	tetrahedral
O	octahedral
TO	tetrahedral-octahedral
TOT	tetrahedral-octahedral-tetrahedral
ESA	edge surface area

NMR	nuclear magnetic resonance
k	Boltzmann constant
ΔE	energy barrier
ΔE_a	activation energy
P_i	probability
TST	transition state theory
SEM	secondary electron microscopy
FCS	first coordination sphere
SCS	second coordination sphere

Chapter 1

Introduction

Silicate minerals constitute most of the crustal rocks and terrestrial sediments. Silicate dissolution is a rate-limiting step in geochemical processes, such as weathering and soil formation, metasomatic and hydrothermal rock alteration, formation of secondary pore space in siliciclastic rocks, and many others. The interest in silicate dissolution is driven by its basic importance for various scientific and engineering problems, such as carbon sequestration and disposal of radioactive waste. Both problems are related to long-term stability of rocks used as carbon dioxide or waste storage sites. Rock porosity and permeability characteristics depend on the history of basin development, rock composition and environmental conditions, which in turn control (and are controlled by) rates of mineral dissolution and precipitation reactions. Nuclear waste storage safety is defined by the risk of the radioactive element's leakage into the natural aquifers, which may happen due to the rock dissolution and formation of channels and cavities. Lastly, knowledge of silicate

dissolution kinetics is of fundamental importance in industrial and environmental applications. Geochemical exploration of metal deposits and estimation of toxic elements' release from mine tailings requires the use of reactive transport models. Silicate minerals are also a major component of cements, ceramics, insulators and materials for nanocomposite manufacturing.

Silicate dissolution process can be investigated using experimental methods as well as theoretical calculations and models. We can distinguish two main experimental approaches used to evaluate dissolution mechanisms and rates: analysis of reacted solvent composition and microscopic observations of the mineral surface. The first method provides values of the macroscopic (bulk) rate for various silicate minerals and environmental conditions (Brantley, 2008). However, there are two problems associated with this method. First, the use of this method requires proper rate normalization by the number or density of reactive surface sites. The reactive site density is not a constant parameter, because it depends on the environmental conditions. Second, the rates obtained by the different laboratories for the same environmental conditions may vary over 2-3 orders of magnitude. Interestingly, Fischer et al. (2012) obtained similar rate variation by analyzing spatial rate distribution for calcite systems. Luttge et al. (2013) considered this variance as an intrinsic property of all crystalline systems. Therefore, the information about reactivity distribution over the surface is critically important for the studies of mineral dissolution kinetics. Microscopic observations allow us to measure dissolution rates directly, as normal surface retreat or velocity of atomic step movement. In these cases, we do not need a prior estimate of reactive site density. Another great advantage of this

method is its capability to assess dissolution mechanisms by analyzing surface structure at different scales. The Vertical Scanning Interferometer (VSI) has a large field of view (from 10,000 μm^2 to mm^2) that allows us to quantify reactivity distribution over the surface and access spatial and temporal rate variations (Arvidson et al., 2003; Fischer et al., 2012). This method has been successfully used to study dissolution of feldspars (Luttge et al., 1999; Arvidson et al., 2004) and silicate glasses (Icenhower et al., 2002) as well as non-silicate minerals, such as calcite (Arvidson et al., 2003; Fischer et al., 2012), dolomite (Luttge et al., 2003), pyrite (Asta et al., 2008). Atomic Force Microscopy (AFM) is another technique used to measure rates and reveal detailed structure of surface features at the nm-level of lateral resolution. For example, Yanina et al. (2006) described structure of etch pits formed on dissolving quartz surface and also measured dissolution rates for various quartz faces.

Computer simulations and theoretical calculations also can be employed for mineral dissolution studies. Ab initio and Molecular Dynamics techniques substantially have advanced the understanding of silicate dissolution controls at the molecular level. The first calculations were made for the simple molecular clusters used as representatives for the silicate bonds. Xiao and Lasaga (1994; 1996) explored the influence of bond chemistry and pH conditions on the mechanisms of bond hydrolysis reactions using Hartree-Fock (HF) and Møller-Plesset (MP2) levels of theory. The development of Density Functional Theory (DFT) enabled the use of more complex models, involving larger clusters, periodic crystal structures and interface water. The DFT studies of cristobalite clusters revealed the strong influence of the long-range order neighbors and bond topologies on Si site reactivity (Pelmenschikov et

al., 2000; Criscenti et al., 2006). The hydrogen bonding network at the mineral-water interface was shown to substantially influence on surface reactivity by stabilizing the surface (Murashov, 2005; Yang and Wang, 2006; Nangia and Garrsion, 2010). Moreover, Kubicki et al. (2012) showed how Na⁺ ions may control dissolution rate by changing the structure of the surface hydrogen bonding network. All these studies high-light the complexity of silicate dissolution reactions at the molecular level. An important conclusion from these findings is that the dissolution process cannot be explained by the kinetics of one or limited number of simple surface reactions. Since the number of possible reactions and controls can be large, a technique bridging these reactions and the overall dissolution kinetics at the bigger scales is required. Kinetic Monte Carlo (KMC) simulations are thus commonly used as a powerful solution to this problem.

The history of KMC method use for mineral dissolution studies is not very long, in con-trast to very similar models for crystal growth (Gilmer and Bennema, 1972; Haan et al., 1974; Gilmer., 1980). Wehrli (1986) formulated KMC model for oxide dissolution at far-from-equilibrium conditions. Blum and Lasaga (1987) developed this method further including molecular attachment, detachment and surface diffusion reactions. They provided formulas of dissolution probabilities for individual surface sites belonging to perfect as well as strained parts of crystals. This model was adapted for A3B (Lasaga and Luttge, 2004a) and AB (Lasaga and Luttge, 2004b) structures, which later served as analogues for feldspars (Zhang and Luttge, 2007; 2008; 2009a;b). Zhang and Luttge modified these models and applied them to realistic feldspar structures. They studied a wide range of problems in kinetics of

feldspar dissolution, such as dissolution rate dependence on the saturation state and chemical compositions of feldspars (Zhang and Luttge, 2007; 2008), the influence of the Si-O-Si and Si-O-Al bond network topology on the dissolution mechanisms (Zhang and Luttge, 2007;2008), leached layer formation (Zhang and Luttge, 2009a). Also, they studied nano-grain morphology as a function of the saturation state and grain size (Zhang and Luttge, 2009b).

Since both microscopic and computational techniques can provide important insights into dissolution mechanisms at the different scales, their simultaneous use opens a great possibility for better understanding of the dissolution process and prediction of dissolution rates at various conditions. The aim of my thesis work is to develop the multi-scale approach to study silicate dissolution kinetics. The approach combines experimental methods, KMC simulations and data derived from electronic structure and Molecular Dynamics (MD) calculations. The ultimate goal is to create a comprehensive method capable revealing dissolution mechanisms and controls, as well as predicting surface structure and reactivity at the scales from nanometers to microns. Development of the KMC models powered by the knowledge derived from *ab initio* and MD data is at the center of this approach. Experimental studies supply the data for model parameterization and verification, and are also used as an independent means of assessing dissolution mechanisms at the micron scale.

I used muscovite and quartz as the primary structures in this study. These minerals represent two silicate groups with contrasting structures and composition: phyllo- and tectosilicates. Phyllosilicates have a layered 2-dimensional structure and

quite complex chemical composition, where Si^{4+} , Al^{3+} , Al^{6+} , Mg^{2+} , Fe^{2+} form layers and Li^+ , Na^+ , K^+ , $(\text{OH})^-$ fill interlayer space. On contrast, tectosilicates has framework 3-dimensional structure and simpler composition: Si^{4+} , Al^{3+} form a framework with Na^+ , K^+ and Ca^+ in the framework's cavities. Both minerals are common in crustal rocks and terrestrial sediments. Muscovite also can serve as an analogue for clay minerals common in soils, riverine sediments and siliciclastic sedimentary rocks.

The widespread hypothesis of phyllosilicate dissolution mechanisms postulated that their laminated structure is responsible for the existence of the two types of surface areas: "reactive" edges and "unreactive" basal faces. Dissolution was assumed to occur only at the edge faces, while basal faces were excluded from consideration (Kuwahara, 2006; 2008). The validity of this hypothesis was tested in the first part of this thesis using experimental methods. In this work I quantified spatial and temporal distribution of the mean surface heights and roughness using VSI and measured detailed structure of etch pits and steps using AFM. The stepwave model (Lasaga and Luttge, 2001) was used to provide a mechanistic explanation for the observed dissolution scenarios and surface morphology. This work is presented in Chapter 2. In order to understand formation of the observed etch pit structures and step orientation, I developed and tested several KMC models that differ in terms of parameterization. In Chapter 3 these models are described together with their simulation results. A discussion of reactive site topology for muscovite structure is also included. In Chapter 4 a set of KMC models for quartz structure is presented, where

more details for surface site differentiation are provided, and surface stabilization effects induced by the hydrogen bonding network are considered.

1.1. References

Arvidson R.S., Ertan I.E., Amonette J.E. and Luttge A. (2003) Variation in calcite dissolution rates: A fundamental problem? *Geochim. Cosmochim. Acta* **67**, 1623–1634.

Arvidson R.S., Beig M. S. and Luttge A. (2004) Single-crystal plagioclase feldspar dissolution rates measured by vertical scanning interferometry. *Am. Miner.* **89**, 51–56.

Asta M.P., Cama J., Soler J.M., Arvidson R.S. and Luttge A. (2008) Interferometric study of pyrite surface reactivity in acidic conditions. *Am. Miner.* **93**, 508–519.

Blum A.E. and Lasaga A.C. (1987) Monte Carlo Simulations of Surface Reaction Rate Laws, in *Aquatic surface chemistry* (John Wiley & Sons, 1987), 255-292.

Brantley S. L. (2008) Kinetics of mineral dissolution, in *Kinetics of water-rock interaction* (eds. Brantley S. L., Kubicki J.D. and White A.F.), Springer Science+Business Media, LLC, pp. 151-210.

Criscenti L. J., Kubicki J.D. and Brantley S.L. (2006) Silicate glass and mineral dissolution: calculated reaction paths and activation energies for hydrolysis of a Q³Si by H₃O⁺ using ab initio methods. *J. Phys. Chem. A* **110**, 198-206.

Fischer C., Arvidson R.S. and Luttge A. (2012) How predictable are dissolution rates of crystalline material? *Geochim. Cosmochim. Acta* **98**, 177-185.

Gilmer G.H. and Bennema P. (1972) Computer simulation of crystal surface structure and growth kinetics *J. Cryst. Growth* **13/14**, 148-153.

Gilmer G.H. (1980) Computer models of crystal growth. *Science* **208**, 355-363.

Haan S.W.H., Meeussen V.J.A., Veltman B.P., Bennema P., Van Leeuwen C. and Gilmer G.H. (1974) Simulation of a crystal growth with a special purpose computer. *J. Cryst. Growth* **24/25**, 491-494.

Icenhower J.P., Lüttge A., McGrail B.P, Beig M.S., Arvidson R.S., Rodriguez E.A., Steele J.L. and Baum S.R. (2002) Results of vertical scanning interferometry (VSI) of dissolved borosilicate glass: evidence for variable surface features and global surface retreat. 2002 MRS Fall Meeting, *MRS Proceedings* **757**, II5.1, doi:10.1557/PROC-757-II5.1.

Kubicki, J.D., Sofo, J.O., Skelton, A.A. and Bandura, A.V. (2012) A new hypothesis for the dissolution mechanism of silicates. *J. Phys. Chem. C*, **116**, 17479-17491.

Kuwahara Y. (2006) In-situ AFM study of smectite dissolution under alkaline conditions at room temperature. *Am. Mineral.* **91**, 1142-1149 .

Kuwahara Y. (2008) In situ observations of muscovite dissolution under alkaline conditions at 25-50°C by AFM with an air/fluid heated system. *Am. Mineral.* **93**, 1028-1033.

Lasaga A. C. and Luttge A. (2001) Variation of crystal dissolution rate based on dissolution stepwave model. *Science* **23**, 2400-2404.

Lasaga A.C. and Luttge A. (2004a) Mineralogical approaches to fundamental crystal dissolution kinetics-Dissolution of an A3B structure. *Eur. Jour.Mineral.* **16**, 713-729.

Lasaga A.C. and Luttge A. (2004b) Mineralogical approaches to fundamental crystal dissolution kinetics. *Amer. Mineral.* **89**, 527-540.

Luttge A., Arvidson R.S. and Fischer C. (2013) A stochastic treatment of crystal dissolution kinetics. *Elements*, **9**, 177-182.

Luttge A., Bolton E.W. and Lasaga A.C. (1999) An interferometric study of the dissolution kinetics of anorthite: the role of reactive surface area. *Am. J. Sci.*, **299**, 652-678.

Luttge A., Winkler U. and Lasaga A.C. (2003) Interferometric study of the dolomite dissolution: a new conceptual model for mineral dissolution. *Geochim. Cosmochim. Acta* **67**, 1099-1116.

Murashov V.V. (2005) Reconstruction of pristine and hydrolyzed quartz surfaces. *J. Phys. Chem. B* **109**, 4144-4151.

Nangia S. and Garrison B. J. (2010) Role of intrasurface hydrogen bonding on silica dissolution. *J. Phys. Chem. C* **114**, 2267-2272.

Pelmenschikov A., Strandh H., Pettersson L.G.M. and Leszczynski J. (2000) Lattice Resistance to Hydrolysis of Si-O-Si bonds of silicate minerals: *ab initio* calculations of a single water attack onto the (001) and (111) β -cristobalite surfaces. *J. Phys. Chem. B* **104**, 5779-5783.

Wehrli B. (1989) Monte Carlo Simulations of Surface Morphologies during Mineral Dissolution. *J. Colloid Interface Sci.* **132**, 230-242.

Xiao Y. and Lasaga A. C. (1994) Ab initio quantum mechanical studies of the kinetics and mechanisms of silicate dissolution: H⁺(H₃O⁺) catalysis. *Geochim. Cosmochim. Acta* **58**, 5379-5400.

Xiao, Y. and Lasaga, A.C. (1996) Ab initio quantum mechanical studies of the kinetics and mechanisms of quartz dissolution: OH⁻ catalysis. *Geochim.Cosmochim.Acta.* **60**, 2283-2295.

Yanina S.V., Rosso K. M. and Meakin P. (2006) Defect distribution and dissolution morphologies on low-index surfaces of α -quartz. *Geochim.Cosmochim.Acta.* **70**, 1113-1127.

Yang J. and Wang E.G. (2006) Water adsorption on hydroxylated α -quartz (0001) surfaces: From monomer to flat bilayer. *Phys. Rev. B* **73**, 035406.

Zhang L. and Luttge A. (2007) Al,Si order in albite and its effect on albite dissolution process: A Monte Carlo study. *Amer. Mineral.* **92**, 1316-1324.

Zhang L. and Luttge A. (2008) Aluminosilicate dissolution kinetics: A general stochastic model. *J. Phys. Chem. B* **112(6)**, 1736-1742.

Zhang L. and Luttge A. (2009a) A general kinetic model of plagioclase dissolution, *Geochim. Cosmochim. Acta* **73**, 2832-2849.

Zhang L. and Luttge A. (2009b) Morphological evolution of dissolving feldspar particles with anisotropic surface kinetics and implications for dissolution rate normalization and grain size dependence: A kinetic modeling study. *Geochim. Cosmochim. Acta* **73**, 6757-6770.

Does the stepwave model predict mica dissolution kinetics?

Inna Kurganskaya¹, Rolf S. Arvidson^{1,2}, Cornelius Fischer^{1,2}, and Andreas Luttge^{1,2,3}

¹Department of Earth Science, Rice University, Houston TX 77005 USA

²MARUM / FB 5 - Geowissenschaften, Universität Bremen, Klagenfurter Str. D-28359 Bremen, Germany

³Department of Chemistry, Rice University, Houston TX 77005 USA

This paper is published in Geochimica et Cosmochimica Acta: Kurganskaya I., Arvidson R.S., Fischer C. and Luttge A. (2012) Does the stepwave model predicts mica dissolution kinetics? Geochimica et Cosmochimica Acta Vol. 97, pp. 120-130. A permission to reuse is obtained from Elsevier, Copyright (2012).

2.1. Abstract

The micas are a unique class of minerals because of their layered structure. A frequent question arising in mica dissolution studies is whether this layered structure radically changes the dissolution mechanism. We address this question here, using data from VSI and AFM experiments involving muscovite to evaluate crystallographic controls on mica dissolution. These data provide insight into the dissolution process, and reveal important links to patterns of dissolution observed in framework minerals. Under our experimental conditions (pH 9.4, 155°C), the *minimal global* rate of normal surface retreat observed in VSI data was 1.42×10^{-10} mols/m²/s ($\sigma = 27\%$) while the *local* rate observed at deep etch pits reached 416×10^{-10} mols/m²/s ($\sigma = 49\%$). Complementary AFM data clearly shows crystallographic control of mica dissolution, both in terms of step advance and the geometric influence of interlayer rotation (stacking periodicity). These observations indicate that basal/edge surface area ratios are highly variable and change continuously over the course of reaction, thus obviating their utility as characteristic parameters defining mica reactivity. Instead, these observations of overall dissolution rate and the influence of screw dislocations illustrate the link between atomic step movement and overall dissolution rate defined by surface retreat normal to the mica surface. Considered in light of similar observations available elsewhere in the literature, these relationships provide support for application of the stepwave model to mica dissolution kinetics. This approach provides a basic mechanistic link between the dissolu-

tion kinetics of phyllosilicates, framework silicates, and related minerals, and suggests a resolution to the general problem of mica reactivity.

2.2. Introduction

Is the dissolution of phyllosilicates fundamentally different from that of framework silicates such as quartz and feldspars? Current debate and observations suggest the answer is yes (e.g., Turpault and Trotignon, 1994; Rufe and Hochella, 1999; Bickmore et al., 2001; Hodson, 2006; Kuwahara, 2006, 2008; Oelkers et al., 2008), i.e., that the strong anisotropy of phyllosilicates is responsible for large differences between the dissolution rate of the basal (001) surface versus the (hk0) surfaces normal to it. Part of the motivation to quantify these differences is tied to the long-standing uncertainty of the relationship between bulk rates and total (BET) surface area. Our view is that this approach to the kinetics of mica dissolution is a distraction, and is potentially misleading as well. First, as we have discussed elsewhere (Luttge et al., 1999, 2003; Luttge, 2005), the normalization of bulk rates with respect to (“reactive”) surface area is inherently ambiguous and generally problematic. Secondly, there is substantial early work showing that the mica group’s structural diversity (e.g., polytypism) arises during growth through nucleation of screw dislocations (Baronnet, 1972, 1975; Baronnet et al., 1981; Pandey et al., 1982; Nespolo, 2001). The propagation and persistence of spiral defects during mica growth is critical, because it implies a common link to framework silicates in terms of possible mechanisms of dissolution. In complementary importance to their role in crystal growth (identified by Frank, Burt, Cabrera in the classic BCF papers (Frank,

1949; Burton et al., 1949, 1951), screw dislocations also play a fundamental role in dissolution. This role was reevaluated in the stepwave model (Lasaga and Luttge, 2001), which established the link between the opening of hollow cores, the subsequent nucleation of etch pits, and the periodic generation of trains or waves of surface steps. The transit of these stepwaves over the surface progressively reduces its height, and is thus the primary means of bulk removal during dissolution. This link, together with expressions calibrating step velocity with free energy, advanced a general and quantitative model for crystal dissolution kinetics, illustrated with diverse phases of silicate, carbonate, and other compositions (Luttge et al., 2003; Arvidson et al., 2004; Vinson and Luttge, 2005; Asta et al., 2008).

In this paper, we ask whether mica dissolution can be understood in the same way. In this context, differentiation of reaction rates on various surfaces is only of derivative value, as our purpose is ultimately to understand phyllosilicate surface reaction mechanism. To this effort we present vertical scanning interferometry (VSI) and atomic force microscopy (AFM) observations of mica (muscovite) dissolution under simple fixed conditions (pH 9.4, 155°C) far from equilibrium. Philosophically, the paper is organized in the following way. First, we shall show that these new observations are entirely consistent with published data from similar phases, and moreover that this consistency is to be expected in light of central structural considerations. We shall examine the relevance of the aforementioned “basal plane versus edge face reactivity” issue in this context. Second, and more importantly, we shall use these observations to test the application of the stepwave model, heretofore applied primarily to framework minerals. If this application is correct, it estab-

lishes a powerful means of understanding the problem of phyllosilicate dissolution kinetics in a general way, and the distribution of rates that result.

2.3. Methods

Muscovite samples taken from a common stock (Ward's Natural Science #49 V 5882) were prepared by cutting and cleaving with a clean razor into specimens 3×1 cm in area and ~1 mm in thickness. Samples were fixed parallel to the (001) cleavage on a titanium sample holder with silicone polymer, yielding exposed (001) surfaces of very low roughness ($S_q < 2.5$ nm). Additional polymer was also applied at select locations on the exposed (001) surface for the purpose of maintaining reference areas excluded from fluid contact (see below). Exposed edge faces were also sealed with the same compound. The sample holder was then mounted in a stirred, flow-through, titanium autoclave modified from Arvidson and Luttge (2010) to limit the wetted reaction volume to ~3.5 mL. Input solutions were composed from borax buffer mixtures (0.010 m $\text{Na}_2\text{B}_4\text{O}_7 \cdot 10\text{H}_2\text{O}$ + 0.022 m NaOH) to give an input pH of 11.42 ± 0.01 , measured at 22°C with a combination calomel glass electrode. The in situ reactor pH at temperature was computed from EQ3/6 (Wolery and Jarek, 2003) was 9.41. Temperatures within the reactor were measured by internal chromel-constantan (type E) thermocouple, and heating rate fixed by a microprocessor-controlled furnace.

Far-from-equilibrium conditions were maintained by pumping prepared input solution at a constant rate (0.2 mL/min) through the reactor volume with tem-

perature fixed at $155 \pm 0.5^\circ\text{C}$. The mica sample was reacted for an initial time step of 12 h, removed from the reactor, allowed to cool, briefly washed in deionized water, air dried, and mounted on the AFM or VSI instrument stage for surface analysis. After analysis the sample was returned to the reactor and run conditions were reestablished, a process that was repeated at 27, 100, 220, 360, and 500 hours cumulative reaction time.

The interferometer was a Zometrics Zemapper equipped with 2000×2000 pixel CCD camera, tunable LED light source, $10\times$, $20\times$, $50\times$, and $100\times$ Mirau objectives and $1.6\times$ upper ocular, and a field of view at $10\times$ of 1.5×1.5 mm. Rates were measured by analysis of surface height relative to polymer-protected reference areas at each time step. The application of VSI to the measurement of reaction rates and characterization of surface topography is now well-established in the literature (see, e.g., Luttge et al., 1999, 2003; Arvidson et al., 2003); details regarding this specific instrument and associated physical principles are available in Luttge and Arvidson (2010).

At the conclusion of the experiments, samples were also examined with a Nanoscope III AFM instrument in tapping mode. Scan area was 515×512 pixels, with fields of view ranging from $20 \times 20 \mu\text{m}$ to $2 \times 2 \mu\text{m}$ with a scan rate (lines/sec) of 1 Hz. Additional high resolution (1024×1024 pixels) data of selected reacted surfaces were also obtained using a Bruker MultiMode 8 AFM. Data were acquired in ScanAsyst-HR (self-optimizing AFM mode) based on Peak Force Tapping Mode. The scan rate was 1.4 Hz for a $10 \times 10 \mu\text{m}$ image and 3.6 Hz for a $2 \times 2 \mu\text{m}$ image.

2.4. Results

2.4.1. VSI data of etch pit populations

The development and distribution of etch pits on the mica surface was complex and heterogeneous. Etch pits were observed at the first (12 h) time step. These pits were round or oval in shape, ranging from 4 to 7 μm in diameter and 50 to 300 nm in depth. Their diameter and depth continued to increase over the course of the entire experiment. Pits were distributed over the (001) surface either as isolated pits or clusters of variable density and association (Figs. 2-1A and 2-1B). They were also distributed along organized tracks, creating trench-like features (Fig. 2-1C). Pits with diameters $>5 \mu\text{m}$ also formed by the successive coalescence and cannibalization of smaller pits; maximum pit diameter observed after 500 h was 20 μm . A second generation of pits appeared at the 100 h time step and was widespread by 220 h, with initial diameters of ~ 0.5 to 1.5 μm (the minimum diameter is close to the limits of lateral detection for this instrument) and depths of 20-30 nm. These pits were thus smaller than those observed initially, and were frequently annihilated by coalescence of adjoining, larger pits. However, these smaller pits characterized more than half of the (001) surface, yielding minimum height variations of 20 nm for these areas (see also Table 2-1).

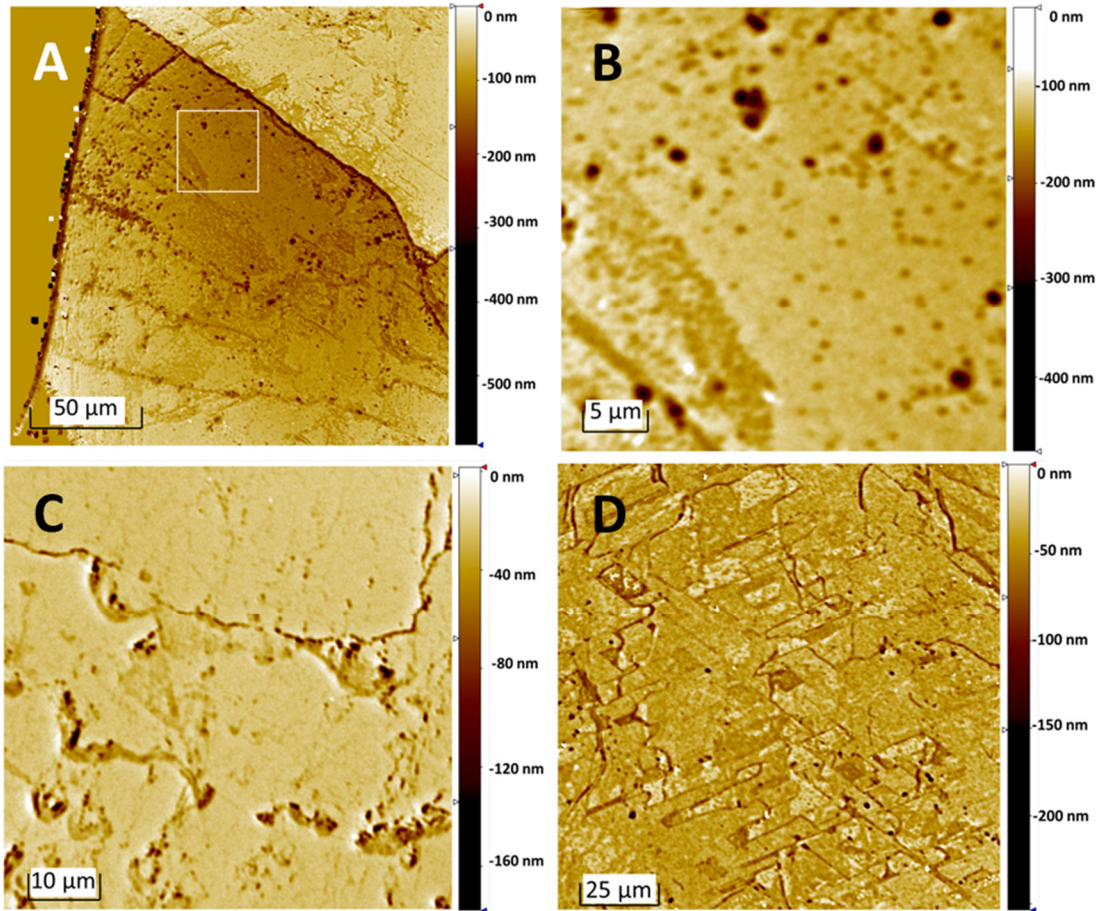


Figure 2-1. VSI data for muscovite (001) surface. (A) 189×189 μm field of view showing irregular etch pit distributions after 360 hours of reaction. (B) Inset area (35 × 35 μm) from A showing submicron-sized pits appearing after 220 hours together with larger earlier-formed coalescent pits. (C) An area (69 × 69 μm) at the 100 h time step showing formation of pit chains and trenches. (D) An area (135 × 135 μm) characterized by formation of linear structures. The lines are oriented in two principal directions intersecting at 120°.

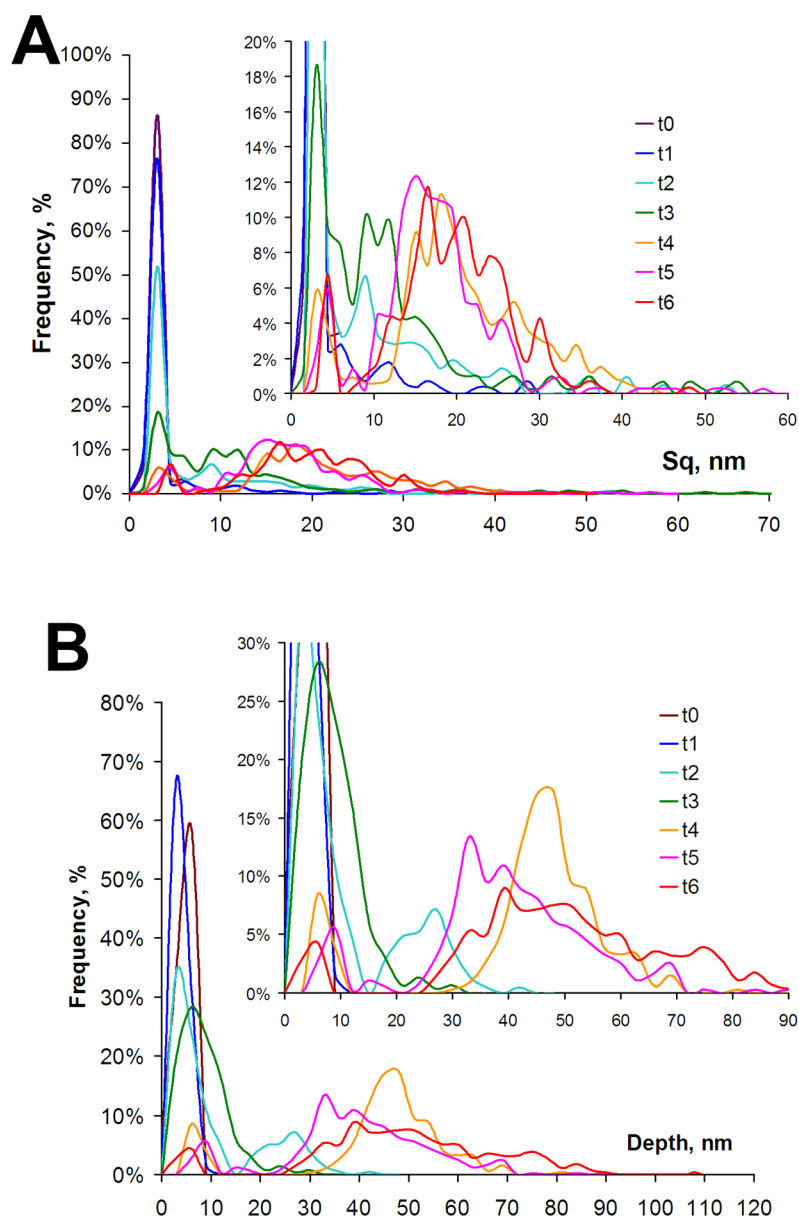


Figure 2-2. Evolution in frequency distributions of roughness (A) and height (B) from time steps t_1 to t_6 (initial condition = t_0). Insets show expanded detail of complex changes involving nucleation and growth of etch pits. See text for discussion.

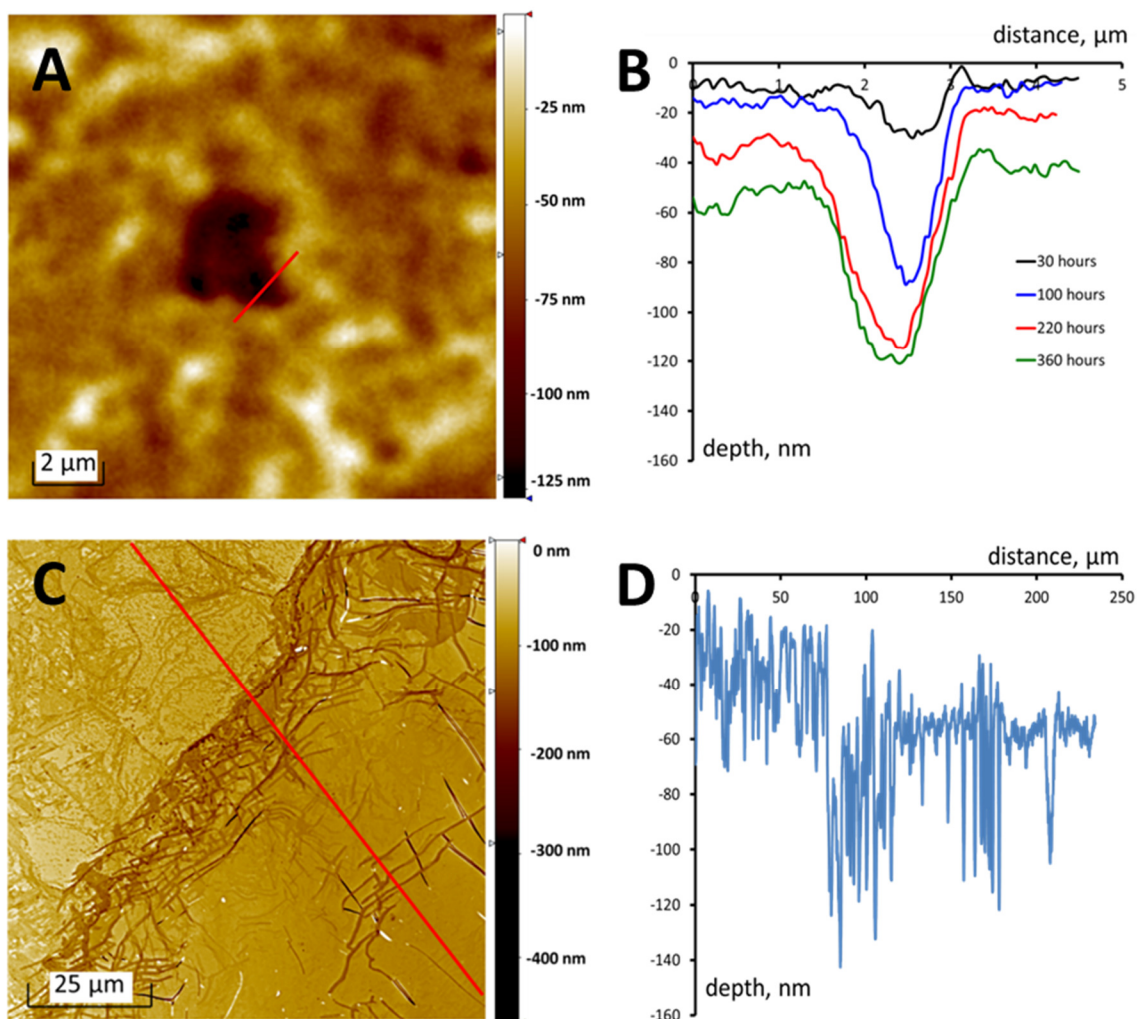


Figure 2-3. Determination of dissolution rates from VSI data. (A) Etch pit (dia. $\sim 4 \mu\text{m}$) formed through probable coalescence of individual pits ($10 \times 10 \mu\text{m}$ field of view). (B) Time series of cross sections through red line at A. (C) Boundary of temporarily masked (upper left) and permanently exposed (lower right) regions ($189 \times 189 \mu\text{m}$ field of view) used to calculate normal surface retreat. Left side had been masked between 220 and 500 hours of experiment. (D) Cross section through the area shown on (C).

Surface root mean square roughness (Sq), computed as

$$Sq = \sqrt{\frac{1}{MN} \sum_i^M \sum_j^N (z(x_i, y_j))^2} \quad (2-1)$$

generally increased over the course of the experiment, from 2.0 (0 h) to 18.9 (500 h). The evolution of surface roughness and height distributions are shown in Table 2-1 and Fig. 2-2.

Surveys of large areas of the mica surface after 500 hours of reaction also indicated broadly organized areas of etch pit distributions forming mosaics delineated by boundaries at angles of 120°. The height difference between these areas was 5 to 10 nms (500 h time step, Fig. 2-1D).

Although individual pits were approximately circular in outline, the slope of pit walls varied with respect to direction (Figs. 2-3A and 2-3B), and this morphology was maintained over time despite increases in pit diameter and depth. Comparison with time-invariant landmarks over the course of reaction showed that this slope asymmetry corresponded to differences in the speed with which one side of the pit moved relative to the opposing side. The approximate ratio of these speeds varied between 2 and 3, and the observed cumulative rate of increase in diameter was 3-4 nm/h. The rate of increase in etch pit depth is substantially less, ~ 0.5 nm/h. This pattern of increasing etch pit depth and diameter was interrupted at the 360 h time step, when the local depth of pits measured from immediately adjacent terraces ac-

tually decreased relative to the preceding measurement, synchronous with the appearance of the second generation of pits described above.

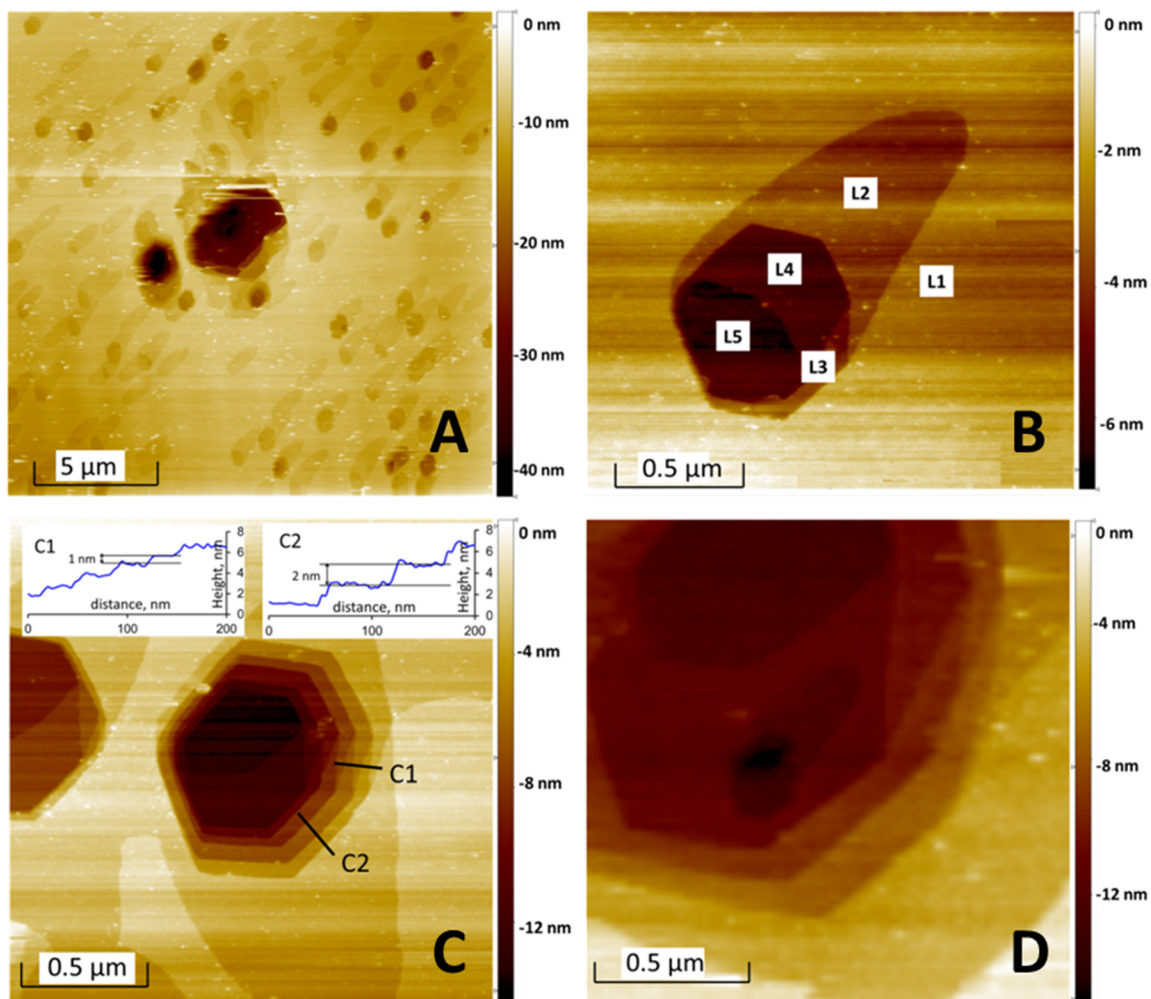


Figure 2-4. AFM data of muscovite (001) surface, 500 h. (A) Note common shape and orientation of etch pits; (B) Etch pit penetrating five layers showing irregular, curved step of shallowest layer and hexagonal outlines of deeper layers; (C) Etch pit structure: profile C1 traverses zigzag steps (see text), profile C2 traverses parallel steps; (D) Detail of central pit in (A), showing opening of new pit in bottommost layer (arrow).

Table 2-1. Roughness parameters. Properties (p) computed as weighted means, $\sum (n \times p)_i / \sum n_i$ in nm.

Time step	Hours after t_0	Total area sampled (mm ²)	Height(depth)	Roughness (Sq)	Peak-to-valley
0	0	0.0174	5.7 ± 1.9	2.3 ± 0.8	15.9 ± 9.8
1	12	0.1772	5.1 ± 1.3	2.9 ± 2.4	275.6 ± 100.3
2	27	0.1307	11.7 ± 9.5	7.9 ± 8.9	176.7 ± 106.8
3	100	0.1847	9.6 ± 4.7	11.2 ± 10.9	308.5 ± 237.2
4	220	0.2047	44.2 ± 15.3	19.7 ± 8.8	236.1 ± 77.3
5	360	0.2230	40.5 ± 14.6	18.1 ± 9.3	193.1 ± 87.1
6	500	0.1745	49.9 ± 19.0	18.9 ± 7.1	249.6 ± 214.5

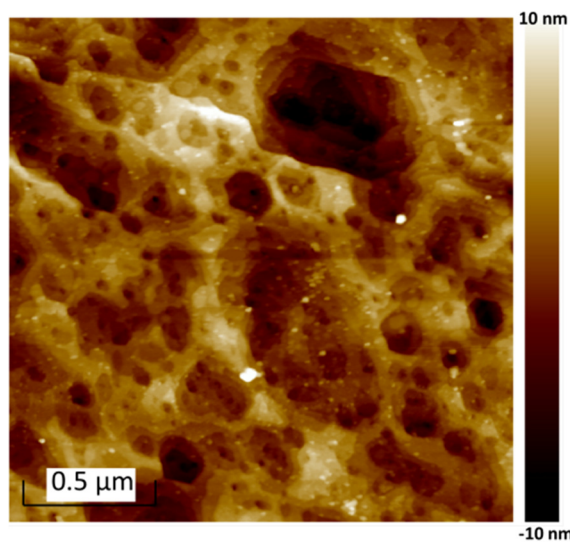


Figure 2-5. AFM image of muscovite (001) surface after 500 h showing etch pit development.

2.4.2. VSI Data: Dissolution Rates

The dissolution rate quantified by comparison of height differences of previously masked reference areas with those continuously exposed is 1.42×10^{-10} mols/m²/s ($\sigma = 27\%$; see Figs. 2-3C and 2-3D). In some cases, masks were applied over areas that had been previously reacted, and thus the reference region contained significant surface roughness (Fig. 2-3D). Here surface normal retreat was not always measurable, because the difference in mean height of reference versus reacted regions was smaller than the surface roughness. This rate is also substantially slower than that computed from the change in etch pit depths (see peak-to-valley means, Table 2-1), 416.36×10^{-10} mols/m²/s ($\sigma = 49\%$), measured prior to the widespread nucleation of new pits observed after 220 h.

2.4.3. AFM Data

Etch pits were also observed at the final (500 h) time step with the atomic force microscope. The diameter of the smallest of these pits is close to the minimum of objects that can be reliably resolved with the interferometer ($\sim 0.5 \mu\text{m}$). These pits are asymmetric in shape but are clearly organized, with the shallowest depths of the pit oriented along two common directions (Fig. 2-4A) disposed at 120° to one another. The layers penetrated by these pits consist of distinct steps 2.0 nm in height (Figs. 2-4B, 2-4C). Pits that penetrate multiple layers also exhibit a characteristic zigzag pattern at one of the walls, with a spacing of 1.0 nm between the steps constituting the zigzag pattern. This zigzag pattern is also observed in the larger

(and less abundant) pits. Initial development of new pits can also be seen within the floors of these features (Fig. 2-4D).

Within areas of the surface populated by small pits (Figs. 2-1B, 2-3A, 2-4A), imaging with the Bruker AFM revealed pits of even smaller diameter (Fig. 2-5) covering the (001) surface. These pits are 50-200 nm in diameter and show densities of >100 pits per μm^2 in select areas.

2.5. Discussion

Our observations of mica dissolution can be strictly summarized as: 1) dissolution of the (001) face proceeds in part by the development of etch pits that reach tens to hundreds of nanometers in depth after several hundred hours of reaction; 2) the diameter of these pits (on the order of microns) is substantially greater than their depth at any given stage in development; 3) in addition to the obvious mass removal at deep etch pits, there is also an overall reduction in surface height at a surface-normal rate that is $\sim 350\times$ slower than that measured at these pits; 4) when observed at high resolution (AFM), etch pits show clear evidence of crystallographic control in the form of hexagonally disposed (60°) step boundaries, with “zigzag” structures connecting adjacent layers. Some of these observations are new, while others are similar to or consistent with specific results available in the literature, as discussed below.

2.5.1. Etch Pit Morphology, Structure, and Distribution

Etch pits are common basal plane dissolution features of phyllosilicates, including clay minerals, as has been shown in previous interferometer and AFM/SEM studies (Patel and Tolyansky, 1957; Patel and Ramanathan, 1962; Johnsson et al., 1992; Rufe and Hochella, 1999; Rufe, 2000; Maurice et al., 2002; Brandt et al., 2003; Aldushin et al., 2006a;b; Shao et al., 2010, 2011). What we wish to focus on here is the unique structure and bonding in these minerals, how these physical properties are expressed in the morphology of the observed dissolution features such as etch pits, and in turn how the organization and distribution of these features control the overall dissolution rate. Finally, we shall illustrate and summarize these relationships via their connection to the step wave model.

The structure of framework silicates is characterized by strong, covalent Si-O-Si and Si-O-Al bonding propagating in three dimensions. Phyllosilicates, in contrast, are distinguished by their layered structure. This structure consists of repetitive tetrahedral (T) and octahedral (O) layers composing TO (kaolinite, lizardite) or TOT (pyrophyllite, talc, muscovite) sheets. The sheets are connected by weak van der Waals or Coulomb bonds. This class of minerals is an end-member case of structural anisotropy common in silicates in general. In most cases, pits were composed by TOT steps. The movement of a TOT step has been identified as a major dissolution mechanism (Rufe and Hochella, 1999; Brandt et al., 2003; Kuwahara, 2008). The distribution of bond energies within TOT layers generates anisotropy in dissolution rates for different $\{hk0\}$ faces (Bickmore et al., 2001). The crystallographic

control of mica thus manifests itself in the two major ways: dependence of step velocities within TOT layers on their crystallographic orientation and mutual influence of the steps in adjacent layers (discussed below). Although adjacent TOT layers are weakly bonded, their geometric juxtaposition controls etch pit morphology and dissolution kinetics. The interlaced zigzag patterns (Figs. 2-4C and 2-4D) reflect stacking periodicity characteristic of polytypism in micas (Baronnet, 1975), and have been observed previously for both illite and apophyllite. Illite has a structure similar to muscovite: both minerals typically possess a $2M_1$ polytype structure characterized by periodic rotation of adjacent layers by 120° and single nm spacing between TOT layers. Kuwahara (1998, 2001) observed this zigzag pattern in polygonal illite growth spirals having single nm spacing between interlaced steps and two nm spacing between parallel steps. Aldushin et al. (2006b) observed these patterns in dodecahedral etch pits on the basal face of apophyllite, and showed that slight rotation between layers caused rotation of dissolution fronts from one layer to another.

Our key point is that this rotation *inhibits* overall step movement. In the absence of this rotation, step edges in the juxtaposed layers of an etch pit have identical structure and orientation. A given etch pit wall is thus composed of parallel $\{hk0\}$ step edges dissolving at a given rate. However, in the case of polytype micas with rotated layers (see Fig. 2-6), the slower rate in adjacent layers determines the overall rate of that step system (see also Fig. 2-4C).

Our data show also significant variation in terms of etch pit density. Similar variations (from < 1 to > 100 pits μm^{-2}) have been reported for the basal face of

phlogopite (> 40 pits μm^{-2} , Aldushin, 2006a) and muscovite (0.07 pits μm^{-2} , Patel and Tolansky, 1957). Other published data give rough estimates of > 60 pits μm^{-2} for muscovite (Maurice et al., 2002) and > 4 pits μm^{-2} for phlogopite (Shao et al., 2010). Reported etch pit depths range from single nanometer, unit TOT layer (Johnsson et al., 1992; Maurice et al., 2002; Brandt et al., 2003) to 50 nm (Aldushin et al., 2006b). In early studies with the interferometer, Patel and Ramanathan (1962) observed large (up to 97 μm in diameter) pits on muscovite, phlogopite and biotite (001) faces with depths of up to 5.5 μm .

Etch pits of monolayer depth are most likely related to simple point defects. In contrast, deep pits having well-defined step edges (Fig. 2-4) likely originate from screw dislocations. Moreover, their presence in muscovite under these conditions is to be expected, as development of screw dislocations have been widely documented during experimental growth of phyllosilicates (Baronnet, 1972; Sunagawa and Koshino, 1975; Sun and Baronnet, 1989; Kuwahara et al., 1998; 2001) and discussed on both a theoretical and experimental basis (Amelinckx, 1952; Baronnet, 1972; Corny et al., 1976; Pandey et al., 1982; Hoche et al., 1999; Nespolo, 2001; Kogure and Inoue, 2005). Other dissolution features observed in this study, such as channels, trenches and chains of etch pits (Figs. 2-1C, 2-1D) are also common on basal faces of other phyllosilicates, such as kaolinite (Brandt et al., 2003) and phlogopite (Shao et al., 2010; 2011).

As reaction proceeds, growth of the above features leads to the development of complex patterns of surface roughness quantified in Fig. 2-2. Similar observations

were made by Brandt et al. (2003) who noted that the dissolved surface of kaolinite consisted of monolayer steps with peak-to-valley value of 7 nm (versus the range observed in Fig. 2 of 20 to > 80 nm).

2.5.2. Distribution of dissolution rates and their control by the phyllosilicate structure

Because the dissolution of muscovite observed here proceeds from a near-atomically flat surface, the distribution of etch pit depths defines the dissolution rate of a given local area. In contrast to the normal surface retreat from absolute (masked) rate measurements (220 -500 h, 1.42×10^{-10} moles $\text{m}^{-2} \text{s}^{-1}$), rates measured simply by analysis of etch pit depths without the absolute reference provided by masked areas show a much larger range and are *minimum* local rates, as the upper terrace surrounding an etch pit may itself suffer a reduction in height as steps move across the surface.

The role of TOT step movement in dissolution has been previously recognized by Wieland and Stumm (1992), Ganor et al. (1995), and Huertas et al., (1999), among others, who have pointed out that the cleavage of Si-O-Al(O) bonds is a rate-controlling step. In comparison, cleavage of basal Si-O-Si or Si-O-Al(T) bonds is energetically unfavorable (Fortier et al., 1994). This observation underlies the assumption of substantial differences between edge and basal face reactivity, restated in many subsequent papers related with phyllosilicate dissolution (Turpault and Trotignon, 1994; Rufe and Hochella, 1999; Bickmore et al., 2001; Hodson, 2006; Kuwahara, 2006, 2008; Oelkers et al., 2008). The common approach to resolve “edge

versus basal face” problem in measured bulk rates has been to normalize material fluxes to edge surface area (ESA) estimated prior to experiment (Turpault and Trotignon, 1994; Bickmore et al., 2001; Hodson, 2006). Rufe and Hochella (1999), Brandt et al. (2003) and Kuwahara (2008), who observed dissolution as a process of step movement originating from etch pit walls, also performed *in situ* normalization to ESA. However, we doubt that the step density (which defines the ESA value) is a parameter that is constant in space and time. Our AFM observations (Figs. 2-4 and 2-5) show complex surfaces with marked variation in step density. Masked VSI measurements show dynamic changes in surface morphology, with etch pits present over a given time interval being subsequently removed to yield comparatively flat terraces (Fig. 2-3C). Detailed AFM data of dissolved chlorite surfaces collected by Brandt et al. (2003) also showed pitted areas terminated by flat terraces.

In addition, we observe a complex evolution in the distribution of surface depth and roughness that is at odds with any description by static, invariant parameters (Table 2-1 and Fig. 2-2). These roughness data, treated using convergence analysis (Fischer and Luttge, 2007), reflect the cumulative effect of coupled processes operating simultaneously over the surface: nucleation of defects and the growth, coalescence, and ultimate annihilation of etch pits. The integrated effect of these processes produces a complex and constantly changing surface with no apparent steady state configuration over the course of reaction.

These observations lead us to conclude that the common approach of normalizing bulk dissolution rates by BET, geometric, or edge surface area should be

abandoned, as the relationship between any of these parameters and the absolute rate is not fixed in time and space. The dissolution mechanisms of mica cannot be reduced to a problem of “edge versus basal face” reactivity, because the basal face *itself* is a source of constantly creating edge faces.

The surprising result is that dissolution mechanism of mica may not be fundamentally different from minerals such as feldspars, calcite, etc., in which point and line defect centers serve as the foci of step movement. In muscovite, these defects serve as the centers of TOT step propagation; bulk removal of material then occurs by step movement at etch pit walls. Local variation in the frequency of step coalescence, partly a function of local defect density, gives rise to a complex, three dimensional surface, whose roughness may in turn be annihilated by the arrival of steps from distant defects. The cumulative effect of these processes leads to the global removal of material from the surface. These observations are consistent with the stepwave model. More importantly, they imply a global applicability of this model, and thus have potential implications for general crystal dissolution. These issues are explored in detail in the following section.

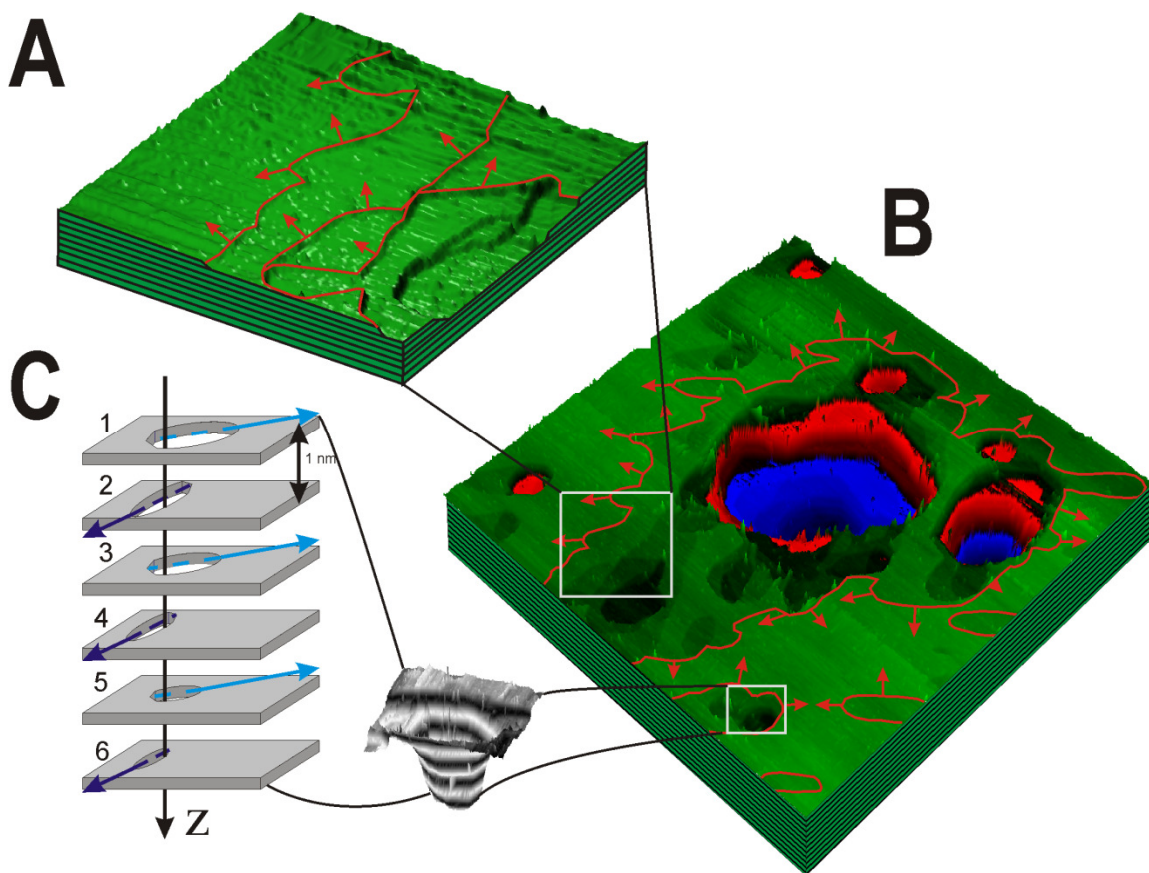


Figure 2-6. Schematic illustration of stepwave formation on muscovite {001} surface. (A) Consecutive steps moving outwards from a dislocation center. (B) Steps emanating from two major etch pits (linear defects) and surrounding monolayer pits (point defects) form a single stepwave of complex morphology. (C) Multilayer etch pit formation, showing layer-by-layer dissolution in two principal directions.

2.5.3. Application of the stepwave model

In 2001 Lasaga and Luttge introduced the so-called stepwave model (compare also Lasaga and Luttge, 2003). A critical aspect of this model involves the role of etch pits, which had previously been understood mainly as the locations of the fastest mass removal in a crystal dissolution process. Terraces between pits, in contrast, were believed to be significantly less reactive and, therefore should contribute to the overall dissolution rate in only a minor way. While the model still recognizes the critical role of etch pits, particularly those formed by screw dislocations, it redefines their mechanistic function in an important way, i.e., as the source for trains of steps that dissolve the crystal lattice layer by layer. The model asserts that the pit wall actually serves as the source for stepwaves, and thus predicts these stepwaves are responsible for the majority of the overall dissolution rate.

The importance of this change in our understanding can be demonstrated best if we undertake a simple thought experiment. We assume a large crystal surface with just one or two etch pits. The conventional model would predict a very slow dissolution rate that is driven mainly by the expansion of these features. However, the stepwave model would predict a significantly faster rate in this same scenario. In the model, the rate is controlled mainly by the velocity of the progressing steps that are generated at the pit walls, while the cumulative rate of mass removal contributed by etch pits themselves remains insignificant. Only in cases of very high defect density would the relative contribution of etch pits become significant compared to stepwave removal.

Subsequent work has focused a) on the description of how steps move across a crystal surface (e.g., Lasaga and Luttge, 2003) and b) developing the model for complete three dimensional crystal structures of feldspars (e.g., albite – anorthite; see Zhang and Luttge, 2008; 2009a,b). In parallel, several experimental studies reported the stepwave mechanism for minerals such as calcite (Vinson and Luttge, 2005), barite (Fewless et al., 2005), albite (Arvidson et al., 2004), pyrite (Asta et al., 2008) and fluoride (Cama et al., 2010).

As a result, there is increasing experimental and theoretical evidence that suggests that the stepwave model provides an accurate description of the dissolution process of tectosilicates as well as other important minerals. However, a critical unanswered question is whether the stepwave model can be used to conceptually describe the dissolution of all crystalline matter.

In this light the present study is of great importance, because phyllosilicates represent not only groups of important minerals, i.e., micas and clays but they are also structurally the most anisotropic members of crystalline matter. While the Si-O-Si and Si-O-Al bonds in the TO- and TOT-layers are strongly covalent in character, the interlayer connections formed by van der Waals and Coulomb bonds are very weak. The results of this experimental study, however, demonstrate that even the anisotropic muscovite structure produces etch pits that initiate stepwaves that subsequently move across the crystal surface (Figs. 2-4 and 2-6). Therefore, it is the kinetics of stepwave formation, their progress and interaction that ultimately define the overall rate of muscovite dissolution.

We argue that the stepwave model can in principle be applied to the dissolution of all phyllosilicates, and basis for this assertion is the abundance of screw dislocations in the highly anisotropic structures of micas. By demonstrating the abundance of pits opening along screw dislocations in phyllosilicates (e.g., Patel and Ramanathan, 1962; Rufe, 2000; Brandt et al., 2003; Aldushin et al., 2006a;b; Shao et al., 2010, 2011) we provide evidence for the most important prerequisite and an important argument that the stepwave model can describe the dissolution of crystalline matter in a general form. This fact might be also one explanation for the otherwise puzzling fact that Burton, Cabrera and Frank developed their theory only for the special case of dissolution at screw dislocations.

2.6. Summary

We have shown that the diversity and distribution of muscovite dissolution rates on numerous scales are consistent with published data for related phyllosilicates. This study reinforces earlier evidence of the key role of screw dislocations in both mica growth and dissolution. Regardless of whether changes in solution composition (e.g., lower pH) generate site-specific differences in step movement, the same bonds need to be broken regardless of the direction of attack. This central truth casts doubt over the utility of debates over edge versus basal plane mechanisms, and the evidence here is that step movement drives the overall dissolution process. The observed link between defects, step movement, and the diversity of rates is consistent with application of the stepwave model, a treatment that allows a

standard approach to the general problem of dissolution of all crystals, layered or framework.

2.7. Acknowledgements

We thank DOE and Dr. Dawn M. Wellman for collaboration and generous support under grant # 117372. We also acknowledge generous support from the Global Climate and Energy Project (GCEP) at Stanford University. An earlier draft of this paper was also improved by the comment of two anonymous reviewers.

2.8. References

Aldushin K., Jordan G. and Schmahl W.W. (2006a) Basal plane reactivity of phyllosilicates studied in situ by hydrothermal atomic force microscopy (HAFM). *Geochim. Cosmochim. Acta* **70**, 4380–4391.

Aldushin K., Jordan G. and Schmahl W.W. (2006b) Kinematics of apophyllite leaching-A terrace-ledge-link process within phyllosilicate interlayers. *J. Cryst. Growth* **297**, 161–168.

Amelinckx S. (1952) Screw dislocations in mica. *Nature* **169**, 580.

Arvidson R.S., Ertan I.E., Amonette J.E. and Luttge A. (2003) Variation in calcite dissolution rates: A fundamental problem? *Geochim. Cosmochim. Acta* **67**, 1623–1634

Arvidson R.S., Beig M. S. and Luttge A. (2004) Single-crystal plagioclase feldspar dissolution rates measured by vertical scanning interferometry. *Am. Miner.* **89**, 51–56.

Arvidson R.S. and Luttge A. (2010) Mineral dissolution kinetics as a function of distance from equilibrium – New experimental results. *Chem. Geol.* **269**, 79–88.

Asta M.P., Cama J., Soler J.M., Arvidson R.S. and Luttge A. (2008) Interferometric study of pyrite surface reactivity in acidic conditions. *Am. Miner.* **93**, 508–519.

Baronnet A. (1972) Growth mechanisms and polytypism in synthetic hydroxyl-bearing phlogopite. *Am. Miner.* **57**, 1272–1293.

Baronnet A. (1975) Growth Spirals and Complex Polytypism in Micas. I. Polytypic structure generation. *Acta Cryst.* **A31**, 345–355.

Baronnet A., Pandey D. and Krishna P. (1981). Application of the faulted matrix model to the growth of polytype structures in mica. *J. Cryst. Growth.* **52**, 963–968.

Bickmore B.R., Bosbach D., Hochella Jr., M.F., Charlet L., Rufe E. (2001) In situ atomic force microscopy study of hectorite and nontronite dissolution: implications for phyllosilicate edge surface structures and dissolution mechanisms. *Am. Miner.* **86**, 411–423.

Brandt F., Bosbach D., Krawczyk-Bärsch E., Arnold T. and Bernhard G. (2003) Chlorite dissolution in the acid pH-range: A combined microscopic and macroscopic approach. *Geochim. Cosmochim. Acta* **67**, 1451–1461.

Burton W.K., Cabrera N., and Frank F.C. (1949) Role of dislocations in crystal growth. *Nature* **163**, 398–399.

Burton W.K., Cabrera N., and Frank F.C. (1951). The growth of crystals and the equilibrium nature of their surfaces. *Phil. Trans. Royal Soc. London, Ser. A, Math. Phys. Sci.* **243**, 299 – 358.

Cama, J., Zhang, L., de Giudici, G., Soler, J.M., Arvidson R.S. and Luttge, A. (2010) Dissolution of fluorite (111) cleavage surface in acid pH: VSI, AFM and Monte Carlo simulations. *Geochim. Cosmochim. Acta* **74**, 4298-4311.

Corny F., Baronnet A. and Jourdan C. (1976) X-ray topographic studies of as-grown defects in natural muscovite. *J. Cryst. Growth* **34**, 304–315.

Fewless T.A., Zhang L., and Luttge A. (2005) Barite Dissolution: Computer Simulations and Experimental Results (15th Annual Goldschmidt Conference, Moscow, Idaho, USA, 20–25 May 2005), *Geochim. Cosmochim. Acta* **69** [Suppl. 1:A] A779.

Fischer C. and Luttge A. (2007) Converged surface roughness parameters—A new tool to quantify rock surface morphology and reactivity alteration. *Am. J. Sci.* **307**, 955–973.

Fortier S.M., Luttge A., Satir M., and Metz P. (1994) Oxygen isotope fractionation between fluorophlogopite and calcite: an experimental investigation of temperature dependence and F-/OH- effects. *Eur. J. Min.* **6**, 53–65.

Frank F.C. (1949) The influence of dislocations on crystal growth. *Discuss. Faraday Soc.* **5**, 48 – 54.

Ganor J., Mogollon J. L. and Lasaga A. C. (1995) The effect of pH on kaolinite dissolution rates and on activation energy. *Geochim. Cosmochim. Acta* **59**, 1037-1052

Hodson M.E. (2006) Searching for the perfect surface area normalizing term—a comparison of BET surface area-, geometric surface area- and mass-normalized dissolution rates of anorthite and biotite. *J. Geochem. Explor.* **88**, 288–291

Hoche T., Habelitz S. and Avramov I. (1999) Crystal morphology engineering in SiO₂-Al₂O₃-MgO-K₂O-Na₂O-F⁻ mica glass-ceramics. *Acta Mater.* **47**, 735-744

Huertas F. J., Chou L., and Wollast R. (1999) Mechanism of kaolinite dissolution at room temperature and pressure Part II: Kinetic study. *Geochim. Cosmochim. Acta* **63**, 3261-3275.

Johnsson P.A., Hochella M.F., Parks. Jr and George A., Blum A.E. and Sposito G (1992) Direct observation of muscovite basal-plane dissolution and secondary phase formation: An XPS, LEED, and SFM study. In *Water-Rock interaction* (eds. Y.K. Kharaka and A.S. Maest). A.A. Balkema, Rotterdam. pp.159–162.

Kogure T. and Inoue A. (2005) Stacking defects and long-period polytypes in kaolin minerals from a hydrothermal deposit. *Eur. J. Miner.* **17**, 465–473.

Kuwahara, Y., Uehara, S. and Aoki, Y. (1998) Surface microtopography of lath-shaped hydrothermal illite by Tapping Mode and Contact Mode AFM. *Clays Clay Miner.* **46**, 547–582.

Kuwahara Y., Uehara S. and Yoshikazu A. (2001) Atomic Force Microscopy study of hydrothermal illite in Izumiyama pottery stone from Arita, Saga Prefecture, Japan. *Clays Clay Miner.* **49**, 301–309.

Kuwahara Y. (2006) In-situ AFM study of smectite dissolution under alkaline conditions at room temperature. *Am. Miner.* **91**, 1142–1149 .

Kuwahara Y. (2008) In situ observations of muscovite dissolution under alkaline conditions at 25-50°C by AFM with an air/fluid heated system. *Am. Miner.* **93**, 1028–1033.

Lasaga A. C. and Luttge A. (2001) Variation of crystal dissolution rate based on dissolution stepwave model. *Science* **23**, 2400–2404.

Lasaga A. C. and Luttge A. (2003) A model for crystal dissolution. *Eur. J. Miner.* **15**, 603–615.

Luttge A., Bolton E.W. and Lasaga A.C. (1999) An interferometric study of the dissolution kinetics of anorthite: the role of reactive surface area. *Am. J. Sci.*, **299**, 652–678.

Luttge A., Winkler U. and Lasaga A.C. (2003) Interferometric study of the dolomite dissolution: a new conceptual model for mineral dissolution. *Geochim. Cosmochim. Acta* **67**, 1099–1116.

Luttge A. (2005) Etch pit coalescence, surface area and overall mineral dissolution rates. *Am. Miner.* **90**, 1776–1783.

Luttge A. and Arvidson R.S. (2010) Reactions at surfaces: A new approach integrating interferometry and kinetic simulations. *J. Am. Ceram. Soc.* **93**, 3519–3530.

- Maurice P.A., McKnight D.M., Leff L., Fulghum J.E. and Gooseff M. (2002) Direct observations of aluminosilicate weathering in the hyporheic zone of an Antarctic Dry Valley stream. *Geochim. Cosmochim. Acta* **66**, 1335–1347.
- Nespolo M. (2001). Perturbative theory of mica polytypism. Role of the M2 layer in the formation of inhomogeneous polytypes. *Clays Clay Miner.* **49**, 1–23.
- Oelkers E.H., Schott J., Gauthier J.-M., Herrero-Roncal T. (2008) An experimental study of the dissolution mechanism and rates of muscovite. *Geochim. Cosmochim. Acta* **72**, 4948–4961.
- Pandey D., Baronnet A. and Krishna P. (1982) Influence of stacking faults on the spiral growth of polytype structures in mica. *Phys. Chem. Minerals* **8**, 268–278.
- Patel A. R. and Tolansky S. (1957) The Etching of crystal cleavages. I. Mica. *Proc. Royal Soc. London. A, Math. Phys. Sci.* **243**, 33–40.
- Patel A.R. and Ramanathan S. (1962) Etching of mica cleavages. *Acta Cryst.* **15**, 860.
- Rufe E and Hochella M. (1999) Quantitative assessment of reactive surface area of phlogopite during acid dissolution. *Science* **285**, 874–876.
- Rufe E. S. (2000) Assessing the reactive surface area of phlogopite during acid dissolution: an atomic force microscopy, X-ray photoelectron spectroscopy and low energy electron diffraction study. M.S. Thesis, 28 pp, Virginia Polytechnic Institute and State University.

Shao H., Ray J.R. and Jun Y.-S. (2010) Dissolution and precipitation of clay minerals under geologic CO₂ sequestration conditions: CO₂-brine-phlogopite interactions. *Environ. Sci. Technol.* **44**, 5999–6005.

Shao H., Ray J.R. and Jun Y.-S. (2011) Effects of salinity and the extent of water on supercritical CO₂-induced phlogopite dissolution and secondary mineral formation. *Environ. Sci. Technol.* **45**, 1737–1743.

Sun B.N. and Baronnet A. (1989) Hydrothermal growth of OH-phlogopite single crystals. I. Undoped growth medium. *J. Cryst. Growth* **96**, 265–276.

Sunagawa I. and Koshino Y. (1975). Growth spirals on kaolin group minerals. *Am. Miner.* **60**, 407–412.

Turpault M.-P. and Trotignon L. (1994) The dissolution of biotite single crystals in dilute HNO₃ at 24°C: Evidence of an anisotropic corrosion process of micas in acidic solutions. *Geochim. Cosmochim. Acta* **58**, 2761–2775.

Wieland E. and Stumm W. (1992) Dissolution kinetics of kaolinite in acidic aqueous solutions at 25 °C. *Geochim. Cosmochim. Acta* **56**, 1645–1662.

Wolery T.J. and R. L. Jarek (2003) EQ3/6, Version 8.0, Software's user manual, Software Document Number: 10813-UM-8.0-00, U.S. Department of Energy, Office of Civilian Radioactive Waste Management, Office of Repository Development, 1261 Town Center Drive, Las Vegas, NV, 89144.

Vinson M. and Luttgge A. (2005) Multiple length-scale kinetics: an integrated study of calcite dissolution rates and strontium inhibition. *Am. J. Sci.* **305**, 119–146.

Zhang L. and Luttge A. (2008) Aluminosilicate dissolution kinetics: A general stochastic model. *J. Phys. Chem. B* **112**, 1736–1742.

Zhang L. and Luttge A (2009a) A general kinetic model of plagioclase dissolution. *Geochim. Cosmochim. Acta* **73**, 2832–2849.

Zhang L. and Luttge A. (2009b) Morphological evolution of dissolving feldspar particles with anisotropic surface kinetics and implications for dissolution rate normalization and grain size dependence: A kinetic modeling study. *Geochim. Cosmochim. Acta* **73**, 6757–6770.

Chapter 3

**A comprehensive stochastic model of
phyllosilicate dissolution: structure
and kinematics of etch pits formed on
muscovite basal face**

Inna Kurganskaya¹ and Andreas Luttge^{1,2,3}

¹Department of Earth Science, Rice University, Houston TX 77005 USA

²MARUM / FB 5 - Geowissenschaften, Universität Bremen, Klagenfurter Str. D-
28359 Bremen, Germany

³Department of Chemistry, Rice University, Houston TX 77005 USA

In press, Geochimica et Cosmochimica Acta

3.1. Abstract

Accurate modeling of phyllosilicate dissolution kinetics is a complex problem involving recognition of the influence of structure, chemical composition, lattice defects, and surface topography on local and global dissolution mechanisms. Previous research has provided a wealth of experimental observations that illustrate the dominant role of etch pits in formation of the steps on the basal face of mica during the dissolution reaction. The shape of the etch pits bears important information on surface reactivity and dissolution rate anisotropy at given environmental conditions. In order to understand the influence of various kinetic factors on etch pit and step morphology, as well as the overall dissolution mechanisms, we have developed a new Kinetic Monte Carlo model simulating dissolution of these minerals. The model considers the effects of chemical composition, structural position, the number of first and second-order nearest neighbors and the steric hindrance of surface atoms on the etch pit morphology and step reactivity. We describe several complexity levels of the model which are characterized by the different ranges of the effects considered. These levels were developed in order to find the most optimal model capable of predicting experimentally observed etch pit morphologies. Our simulation results show that the models based on the sole consideration of the first coordination sphere in general can predict etch pit shape and orientation, while recognition of the site reactivity difference imposed by the steric factors helps us to explain the geometry of monolayer pit superposition. However, the distinction of the ledge and kink sites at all the experimentally observed surface steps is possible only with

the use of the second-order neighbors. Based on these findings, we propose a mechanistic scheme explaining the role of the first and second-order coordination numbers in step stabilization and correct prediction of the etch pit structure.

3.2. Introduction

Phyllosilicates are often distinguished as minerals that have unique dissolution mechanism due to their layered structure. The extreme difference in basal (001) and edge (hk0) face reactivity is typically cited as a primary explanation for the specific dissolution kinetics of these minerals (Turpault and Trotignon, 1994; Rufe and Hochella, 1999; Bickmore et al., 2001; Hodson, 2006; Kuwahara, 2006, 2008). However, the occurrence of etch pits on basal faces undermines the general assumption of low (001) reactivity (Patel and Tolyansky, 1957; Patel and Ramathan, 1962; Johnsson et al., 1992; Rufe and Hochella, 1999; Maurice et al., 2002; Brandt et al., 2003; Aldushin et al., 2006a;b; Shao et al., 2010, 2011; Kurganskaya et al., 2012). The presence of the etch pits provides a basic explanation for crystal dissolution mechanisms proceeding via the generation of steps at etch pit walls, their propagation and coalescence, and, thus, the gradual retreat of the dissolving surface (Lasaga and Lutge, 2001; 2003). Putative differences in reactivity of basal versus edge faces have little relevance to etch pits associated with c^* -oriented screw dislocations (Amelinckx, 1952; Baronnet, 1972;1975; Sunagawa and Koshino, 1975; Pandey et al., 1982). In addition, published data indicate that the layered structure is responsible for a range of other important kinetic effects in phyllosilicate dissolution. For example, the surface step, which typically has one atomic thickness in other

minerals, is made of two or three atomic (tetrahedral and octahedral) layers in phyllosilicates (Rufe and Hochella, 1999; Brandt et al., 2003; Stübner et al., 2008). Another important phenomenon is the specific step interlacing, or “zigzag” patterns, caused by the interlayer rotation common for this class of minerals (Snowden-Ifft et al., 1993; Nagahara et al., 1994; Kuwahara et al., 1998; 2001; Aldushin et al., 2006b). Thus obtaining a more complete understanding of phyllosilicate dissolution mechanisms requires us to integrate the mechanisms common for all minerals and the specific influences of the layered structure. In our previous study (Kurganskaya et al., 2012) we discussed these issues in detail. Particularly, we used experimental observations of reacted surface topography to demonstrate that the stepwave model explains mechanisms of phyllosilicate dissolution. The differential “basal vs. edge” reactivity is not a unique feature characterizing sheet silicates since the other minerals have differential reactivity between the terrace, step and kink sites. We thus treated phyllosilicates in a very general way, explaining their dissolution through kink site and step propagation, step coalescence, etch pit growth and normal surface retreat. Although our previous experimental data demonstrated the structure of etch pits on (001) muscovite face, it was inadequate in describing smaller surface features. These smaller features are presumably influenced by kink site structures, mechanisms of dissolution at these sites, dissolution anisotropy within the mica layers, and etch pit morphology, all of which are integrated into our present model.

The formulation of a KMC model for mineral dissolution based on elementary surface reactions (e.g., atomic attachment, detachment, and surface diffusion) has a relatively short but successful history. Blum and Lasaga (1987) used KMC methods

to define dissolution rates in the presence of a strain field induced by dislocations. They used a simple cubic or Kossel model to reveal the mechanisms of etch pit formation around screw dislocations and the formation and movement of steps at various saturation states. Although such simple models can predict general dissolution mechanisms they lack the kinetic insight of important chemical and structural effects specific for certain minerals. Thus, Wehrli (1989) proposed a KMC model for the dissolution of oxides with complex compositions. More than a decade later, Lasaga and Luttge (2004a;b) formulated a general KMC model, with kink site-based dissolution rate laws applied to very simple AB and A_3B crystal structures. Despite their simplifications, these studies demonstrated the capabilities of the KMC method to extract important mechanistic information, e.g., statistics of the reactive sites, rate dependence on saturation state, the effect of net activation energy, and more. Particularly, the A_3B model served as a precursor template for the study of albite dissolution. Zhang and Luttge (2008; 2009a;b) expanded this basic model by introducing complete feldspar structures and studied the dissolution mechanisms of the entire plagioclase series. Their work addressed order-disorder influences on dissolution rate, the influence of Al concentration in plagioclase feldspars, saturation state dependencies, and temporal evolution of feldspar nanograin morphology and reactivity. Each of the surface reactions considered in these models (dissolution, surface diffusion and adsorption) can be viewed as an integrated result of the bond breaking and formation taking place at any given surface site, and can be characterized as a “site-centered” approach. An alternative “bond-centered” method, based on the explicit incorporation of bond-breaking-forming reactions in the simulation algorithm,

has also been developed. According to this approach, a “reactive event” performed at each iteration step can be either bond breaking or formation, instead of departure or arrival of molecules from and to surface lattice sites as it simulated using “site-centered” method. In 1995, Lasaga had introduced such a model for kaolinite dissolution, where the bond hydrolysis reactions were used instead of dissolution or molecular detachment reactions mentioned above. The results demonstrated that kaolinite dissolves through a layer-by-layer mechanism. It is important to note that the latter mechanism differ from the stepwave mechanism of micas described by Kurganskaya et al. (2012). Nangia and Garrsion (2009) developed another method in which they utilized the reactive potential function to calculate the probabilities of bond breaking-forming reactions. An important breakthrough was the consideration of the influence of long-range order effects of second and third order neighbors on the dissolution probabilities. The strong influence of site topology effect on dissolution rate from surface sites was previously demonstrated already by using electronic structure calculations (Pelmenschikov et al., 2000; Criscenti et al., 2006). However, these “bond-centered” models provide more realistic and accurate results than the “site-centered” models, molecular detachment is an extremely rare event due to the large number of bond-healing reactions competing with the hydrolysis reactions (Pelmenschikov et al., 1992). As a consequence, the typically simulated time-scale and system size are too small to be compared to microscopic observations of surface features and measured dissolution rates. Moreover, simulations involving small systems (such as nanoclusters or nanograins) do not capture all spati-

otemporal variability of surface reactivity that is inherent to natural and synthetic crystals.

On contrast, the “site-centered” approach allows us to simulate dissolution of crystal surfaces that are large enough to produce at least etch pits that are commonly observed in experiments. This approach also allows us to capture spatiotemporal reactivity and surface roughness variations as the most ambitious goal. Currently, the combination of this approach and an effective simulation algorithm allows the simulations of complex pitted surfaces that in the case of Kossel crystal may have lateral sizes of 4000x4000 atoms (Meakin and Rosso, 2008).

Thus, we aim to expand previous “site-centered” approaches further in order to create an effective up-to-date KMC model on phyllosilicate dissolution. We seek to achieve this goal by combining them with the novel findings of site reactivity controls, such as bond topology (Criscenti et al., 2006). Our goal here is to demonstrate the capabilities of a new model to reveal important mechanistic controls of phyllosilicate dissolution. We introduce a KMC model for the dissolution of such minerals. Furthermore, we also make an attempt to treat the complexities inherent in their crystal structure through consideration of second nearest neighbors, steric controls, and the combined influence of defect distribution and system size. Initially we formulate the model at far-from-equilibrium conditions, but it can be expanded for saturation states closer to equilibrium. We next apply the model to simulate muscovite dissolution as a case study. Muscovite is an appropriate template due to its simple chemical composition and ubiquity in crustal rocks. The experimental AFM results

obtained in our previous study (Kurganskaya et al., 2012) serve as a comparison and test for the model verification and parameterization. We report all results here in a step by step approach with increasing model complexity.

In this investigation, we first formulate the stochastic model for phyllosilicate dissolution and describe the simulation algorithm. Second, we briefly describe the potential of the model to explain various kinetic effects and mechanisms. Third, we show how the different versions of the model can be used to simulate etch pit and step morphology on the muscovite (001) face. Finally, we propose a simple mechanistic explanation of etch pit and step structures as have been observed in both experiments and simulations.

3.3. Methods

We developed a new KMC model specifically for phyllosilicates that considers a wide range of effects important for this group of minerals. These effects primarily arise from the unique properties of sheet silicates, including their anisotropic structure, chemical composition, bond orientation, layer stacking sequences, and interlayer diffusion. We describe in this section the important prerequisites for the model (e.g., crystal chemistry and bond topology) and the model itself. The stochastic formulation of corrections for secondary effects, our choices of modeling parameters, system size, the influence of defects, and the simulation algorithm are also outlined and discussed below.

3.3.1. Crystal chemistry of sheet silicates

Phyllosilicates belong to a class of silicate minerals that form “infinite” sheets parallel to each other. The sheets can be of two types: tetrahedral and octahedral, according to the coordination number of the cationic centers, four or six. Tetrahedral (Si^{4+} , Al^{3+}) atoms are arranged in a planar network, in which each tetrahedron is bonded to three other neighbors through common basal oxygen atoms. A fourth oxygen atom (apical) coordinates to octahedral cations (Al^{3+} , Mg^{2+} , $\text{Fe}^{2+}/\text{Fe}^{3+}$) forming an octahedral layer. An octahedral sheet can be connected to either one (1:1 or TO structures) or two (2:1 or TOT structures) tetrahedral sheets (mica group). Depending on chemical composition, micas can be dioctahedral (where each O(OH) atom is surrounded by two 3-valent cations; e.g., Al^{3+}) or trioctahedral (where each O(OH) atom is surrounded by three 2-valent cations; e.g., $\text{Mg}^{2+}/\text{Fe}^{2+}$).

The number of possible TO or TOT layer arrangements in a phyllosilicate crystal is large, giving rise to polytypism. Each of the arrangement possibilities produces a particular polytype structure. Any ideal structure belongs to one of six (1M, 2M1, 3T, 2O, 2M2 and 6H) simple polytypes with 1-6 layers in a unit cell. More complex or “stacking disordered” polytypes may have much longer periods: for instance, Fregola and Scandale (2011) described a 94-layered polytype for kaolinite.

The number of basic bridging bond types in phyllosilicate structures varies from five (muscovite, kaolinite) to 15 (biotite, phengite) (Table 3-1). These types of bonds refer to the most common phyllosilicate compositions and exclude Li, Ti, Mn, and other cations. Only intralayer bonds or bonds within a stable TO or TOT layer

are considered here. Interlayer cations (K, Ca, Na etc.), are excluded from consideration, as they dissolve much faster than the main framework cations.

Table 3-1. Basic types of bridging bonds in phyllosilicate structures.

Ele- ment _(Coordination)	Si	Al(T)	Al(O)	Mg(O)	Fe(O)
Si _(T)	Si-O-Si	Si-O-Al _(T)	Si-O-Al _(O)	Si-O-Mg _(O)	Si-O-Fe _(O)
Al _(T)		Al _(T) -O-Al _(T)	Al _(T) -O-Al _(O)	Al _(T) -O-Mg _(O)	Al _(T) -O-Fe _(O)
Al _(O)			Al _(O) -OH-Al _(O)	Al _(O) -O-Mg _(O)	Al _(O) -O-Fe _(O)
Mg _(O)				Mg _(O) -O-Mg _(O)	Mg _(O) -O-Fe _(O)
Fe _(O)					Fe _(O) -O-Fe _(O)

There are two types of bonds in the tetrahedral layer and 1-3 types in the octahedral layer. The distribution of these bonds within the layers produces varying degrees of order/disorder. Higher disorder leads to greater heterogeneity, creating variations in bonding networks and, thus, in crystal reactivity. The ordering can be of a long-range or short-range type. Long-range ordering of tetrahedral cations is not typical for common micas such as muscovite and biotite (Bailey, 1984); however, some polytypes, such as 3T, tend to be completely ordered. The degree of ordering is correlated to the stoichiometric Si:Al ratio in tetrahedral layers. Short-range ordering, expressed as “Al-Al avoidance” or Loewenstein’s rule (Loewenstein, 1954) is obeyed for micas as for other aluminosilicates. In contrast, octahedral cations exhibit much higher ordering (Bailey, 1984). For instance, Mg and Fe in an Al matrix tend to form Mg or Fe enriched clusters, chains, or domains (Sainz-Diaz et al., 2003).

Muscovite belongs to the 2:1 phyllosilicate group. The stoichiometric formula of this mineral is $\text{KAl}_2(\text{AlSi}_3\text{O}_{10})(\text{F,OH})_2$. A typical muscovite possesses a $2M_1$ polytype structure (Bailey, 1984), which has two TOT layers in one period (Fig. 3-1a).

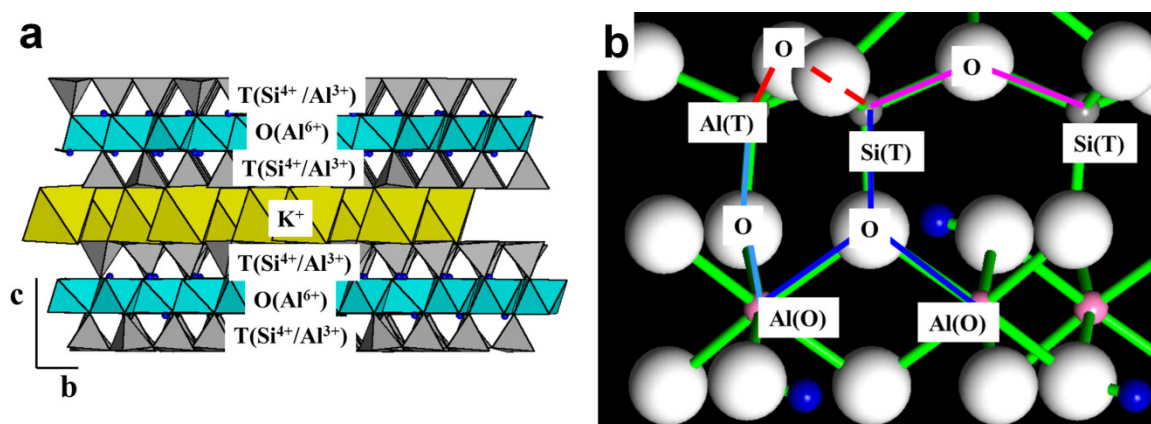


Figure 3-1. Crystal chemistry of muscovite. (a) Polyhedral model of muscovite structure. (b) Bridging bonds in muscovite lattice: Al(T)-O-Si(T), Si(T)-O-Si(T), Si(T)-O-Al(O), Al(T)-O-Al(O) and Al(O)-O-Al(O).

The stoichiometric Si:Al ratio in T layers is 3:1. Tetrahedral Al is randomly distributed in T positions according to NMR studies (Herrero *et al.*, 1987). The unit cell parameters are $a = 5.1918 \text{ \AA}$, $b = 9.0153 \text{ \AA}$, $c = 20.0457 \text{ \AA}$, $\alpha = 90^\circ$, $\beta = 95.735^\circ$, $\gamma = 90^\circ$ (Rothbauer, 1971). The basal (001) face of muscovite is formed by a network of tetrahedral rings capping the underlying network of octahedral 6-membered rings. The vertices of octahedrons are either shared with the tetrahedrons or capped by hydrogen, forming basal hydroxyl groups. The hydroxyls are inclined towards the center of a hexagonal ring (cavity) at an angle $\rho = 8.5^\circ$ (Diego Gatta *et al.*, 2011) to the basal plane. The atoms at the basal faces are fully connected, and, thus possess extremely low reactivity (Fortier *et al.*, 1994). In contrast, muscovite edges or $\{hk0\}$ faces have unsaturated or “dangling” bonds, which substantially increase

the surface site reactivity. The types of the bridging bonds in the muscovite structure are shown in Fig. 3-1b.

3.3.2. Kinetic models of mica dissolution

3.3.2.1. Basic equations and model assumptions

Our approach shares the same assumptions as all other KMC models; i.e., that the probability of a given event has a Boltzmann distribution defined by the formula (3-1):

$$P = \exp\left(-\frac{\Delta E}{kT}\right) \quad (3-1),$$

where ΔE is activation energy of the process. The probability P is equal to the fraction of successful attempts to break the bond over the total number of trials ν (frequency factor). Any surface atom that has n nearest neighbors can dissolve only when all n bonds are broken (hydrolyzed). The probability of this event is scaled by the number of bonds connecting the atom to the surface:

$$P_n = \exp\left(-\frac{n\Delta E}{kT}\right) \quad (3-2).$$

The chemistry and structural positions of atoms forming a bond largely determine the activation energy of bond hydrolysis. We can distinguish at least three different types of bonds in the phyllosilicate structure: 1) bonds within the tetrahedral layer T-O_{br}-T; 2) bonds within the octahedral layer O-O_{br}-O; and 3) bonds con-

necting atoms in different layers, i.e., T-O_{br}-O. Various elements in T and O positions create a range of different bond types.

The application of the KMC approach to the muscovite structure is fairly straightforward, because there are only three major cations (tetrahedral Si/Al and octahedral Al) and only five types of bonds (recall that the bond between tetrahedral Al atoms is excluded from consideration according to the “Al-Al avoidance” rule (Loewenstein, 1954)). Because the tetrahedral positions can be occupied by either Si or Al, each tetrahedral Si atom has n T-O_{br}-Si, m T-O_{br}-Al(T) and l T-O_{br}-O bonds ($n + m \leq 3, l \leq 2$). The dissolution probabilities for this atomic type are calculated as follows:

$$P^{\text{Si}} = \exp\left(-n \frac{\Delta E_{\text{Si-O-Si}}}{kT}\right) \cdot \exp\left(-m \frac{\Delta E_{\text{Si-O-Al(T)}}}{kT}\right) \cdot \exp\left(-l \frac{\Delta E_{\text{Si-O-Al(O)}}}{kT}\right) \quad (3-3).$$

As we discussed above, tetrahedral Al (denoted by Al(T)) atoms have no other Al(T) as first neighbors. Therefore, the probability of dissolution of an Al(T) atom can be simplified to

$$P^{\text{Al(T)}} = \exp\left(-n \frac{\Delta E_{\text{Al(T)-O-Si}}}{kT}\right) \cdot \exp\left(-l \frac{\Delta E_{\text{Al(T)-O-Al(O)}}}{kT}\right) \quad (3-4).$$

Correspondingly, the probability of dissolution of an octahedral Al atom with n Si-O-Al(O), m Al(T)-O-Al(O), and l Al(O)-O-Al(O) bonds is defined b

$$P^{\text{Al(O)}} = \exp\left(-n \frac{\Delta E_{\text{Si-O-Al(O)}}}{kT}\right) \cdot \exp\left(-m \frac{\Delta E_{\text{Al(T)-O-Al(O)}}}{kT}\right) \cdot \exp\left(-l \frac{\Delta E_{\text{Al(O)-O-Al(O)}}}{kT}\right) \quad (3-5).$$

In the case of an arbitrary phyllosilicate mineral the probabilities are calculated as follows:

$$P^{M(O)} = \prod_{i=0}^4 \exp\left(-a_i \frac{\Delta E_{M(O)-O-M_i(T)}}{kT}\right) \prod_{j=0}^N \exp\left(-b_j \frac{\Delta E_{M(O)-O-M_j(O)}}{kT}\right) \quad (3-6),$$

$$P^{M(T)} = \prod_{i=0}^3 \exp\left(-a_i \frac{\Delta E_{M(T)-O-M_i(T)}}{kT}\right) \prod_{j=0}^L \exp\left(-b_j \frac{\Delta E_{M(T)-O-M_j(O)}}{kT}\right) \quad (3-7),$$

where $M(O)$ and $M(T)$ are octahedral and tetrahedral metal centers, respectively, a_i and b_j are Boolean coefficients (0/1); N is the maximum number of octahedral neighbors for an octahedral atom (three for dioctahedral structures and six for trioctahedral), L is the maximum number of octahedral neighbors for a tetrahedral atom (two for dioctahedral and three for trioctahedral structures). The size of the probability set for an individual mineral depends both on the chemical and structural complexity of that mineral (Table 3-2). For instance, kaolinite, whose structure consists of Si and Al atoms arranged into TO sheets only, has 62 possible rate coefficients (probabilities) according to this model. Biotite, whose structure is formed by Si, Al, Mg, and Fe cations, has 1010 possible rate coefficients. Generally, trioctahedral structures have larger numbers of nearest neighbors and therefore larger probability sets.

Table 3-2. Numbers of dissolution rate coefficients for different elements in four layered silicates.

Element(Coordination)	Si	Al(T)	Al(O)	Mg(O)	Fe(O)	Total number of possible rates
kaolinite	30	12	20	-	-	62
muscovite	30	12	60	-	-	102
phlogopite	40	16	-	105	-	161
biotite	100	40	-	435	435	1010

Although the KMC models of mineral dissolution may include precipitation and surface diffusion events (e.g., Lasaga and Luttge, 2004a; b included terms for precipitation and surface diffusion), we do not consider these events in this model. In its present state our model does not apply to near-equilibrium conditions where precipitation may play an important role, although such processes will be accommodated in later revisions. Although surface diffusion is a common process, it does not influence the overall dissolution kinetics unless the detached complex will bind to another active surface site (kink site, etc.). Regardless of these details, the surface structure and active site distribution defining the overall kinetics behavior may remain unchanged.

The primary assumption underlying the model described above is that the probability of bond rupture depends mostly on factors previously described; that is, the number of the first and second-order neighbors, the bond accessibility imposed by the steric factors, and so on. In this work we will explore the effects of these factors on the morphology of surface features.

3.3.2.2. First coordination sphere (FCS): lattice resistance effect

The activation energy for hydrolysis of a given bond is dependent not only on the bonded atoms but also on longer range contributions from the lattice itself. This “lattice resistance effect” (Pelmenschikov *et al.*, 2000) gives rise to complex relationships between activation energy and the overall bonding environment. For example, hydrolysis of the first Si-O-Si bond in a cluster with four Si-O-Si links requires overcoming a barrier of 49 kcal/mol. In contrast, hydrolysis of the last remaining bond requires only 17.5 kcal/mol (Pelmenschikov *et al.*, 2000). Incorporation of this concept in our model requires that the connectivity number (number of connecting M-O_{br}-M links) of surface Si/Al groups *influence the probabilities of each successive hydrolysis event*. Therefore eq. (3-1) must be corrected by inclusion of terms representing the energy contribution of each additional bond. We have thus introduced weighting coefficients (eqs. 3-8 – 3-10) to the probability formulae according to the number and structural position (tetrahedral or octahedral) of the first nearest neighbors:

$$P_i' = W_i P_i \quad (3-8),$$

$$W_T(n, l) = \exp\left(-\frac{n\Delta E_{TT}^1 + l\Delta E_{TO}^1}{kT}\right) \quad (3-9),$$

$$W_O(n, l) = \exp\left(-\frac{n\Delta E_{OT}^1 + l\Delta E_{OO}^1}{kT}\right) \quad (3-10),$$

where $W_T(n,l)$ and $W_O(n,l)$ are weighting coefficients for tetrahedral and octahedral atoms corresponding to nT neighbors and lO neighbors; ΔE_{ij} is the corresponding energy correction between the bond in a bimolecular cluster and the bond constrained by the lattice.

3.3.2.3. Second coordination sphere (SCS) influence

Similar corrections were applied to correct for the influence of the second coordination sphere on the probability expressions (see also Kohli and Ives, 1972) through the introduction of additional weighting coefficients $Q(j,k)$. These coefficients are calculated as functions of the number and structural position of second nearest neighbors:

$$P_{ijk} = W_i P_i \times Q(j,k) \quad (3-11),$$

$$Q_T(j,k) = \exp\left(-\frac{j\Delta E_{TT}^2 + k\Delta E_{TO}^2}{kT}\right) \quad (3-12),$$

$$Q_O(j,k) = \exp\left(-\frac{j\Delta E_{OT}^2 + k\Delta E_{OO}^2}{kT}\right) \quad (3-13).$$

Second nearest neighbors are defined as the tetrahedral and octahedral groups directly connected to the first coordination sphere neighbors through M-O_{br}-M bonds (Fig. 3-2). The exponential form of the coefficients arises from the assumption that the activation energy can be approximated as a linear function of the numbers of first and second neighbors (Kohli and Ives, 1972):

$$E(n_1, n_2) = n_1 \cdot \Delta E_1 + n_2 \cdot \Delta E_2 \quad (3-14).$$

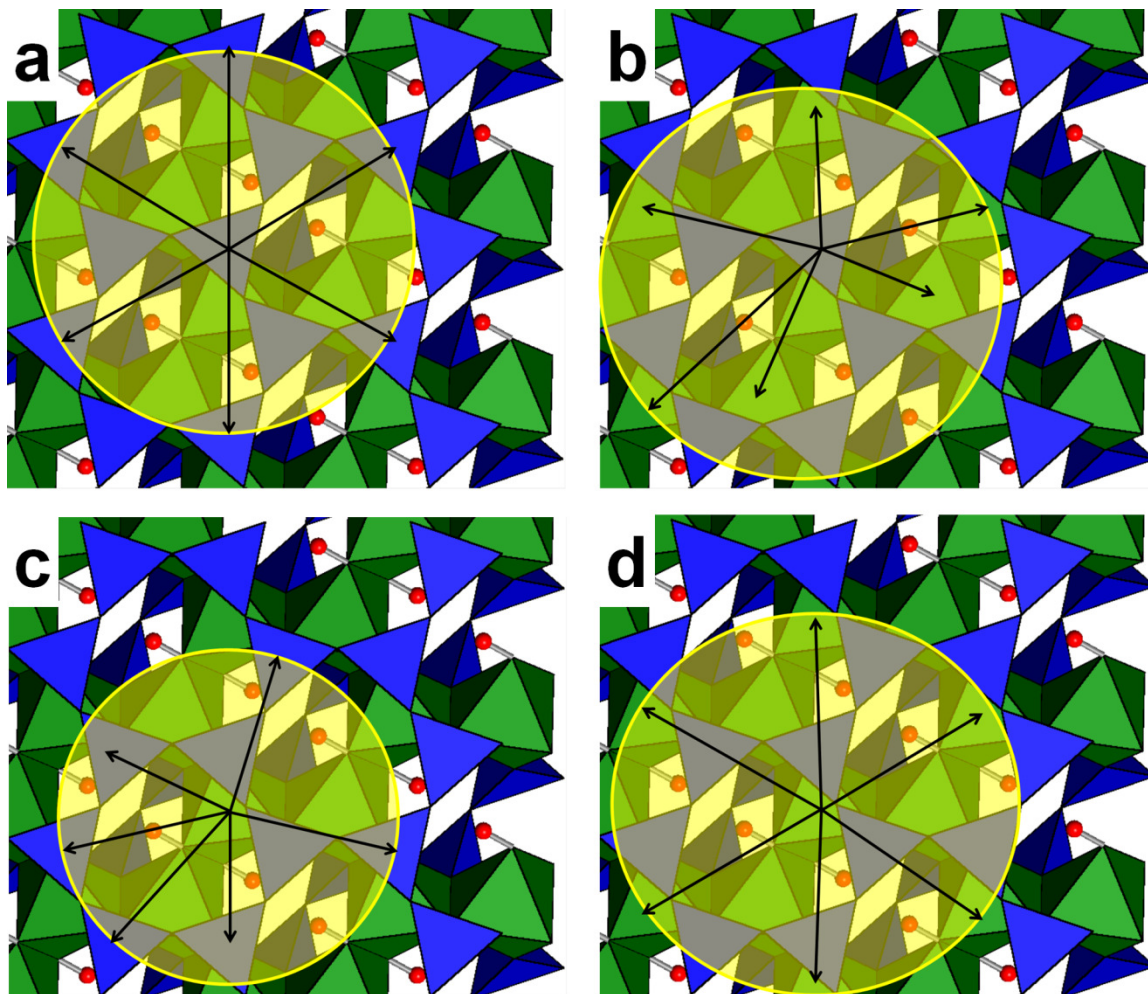


Figure 3-2. Second order coordination spheres for tetrahedral (a,b) and octahedral (c,d) reactive centers. (a) Tetrahedral sphere for tetrahedral center. (b) Octahedral sphere for tetrahedral center. (c) Tetrahedral sphere for octahedral center. (d) Octahedral sphere for octahedral center.

3.3.2.4. Corrections for Al-O-(H)-Al or hydroxyl accessibility

The steric accessibility of reactive sites and bonds introduces additional conformational dependencies. A water or hydronium molecule can directly attack an $M-O_{br}-M$ bond only if it is not shielded and stabilized by overlying atoms, and thus the energy involved in its successful hydrolysis increases with the number of shielding atoms. The weighting coefficients for the first and second neighbors partially resolve this effect by gradually increasing the probability of dissolution as a function of solvent accessibility. However, we also need to recognize special situations where atoms may induce significant steric hindrance of particular bonds. In the structure of dioctahedral micas the bond $Al_{oct}-OH-Al_{oct}$, which does not involve tetrahedral atoms, is inclined to the center of the TOT ring cavity (Fig. 3-3a). The connecting oxygen atom is capped by a proton, so the resulting hydroxyl group is oriented towards to the oxygen atom bridging two adjacent tetrahedral cations (Figs. 3-3a, 3-3b). If one of these cations is removed, the shielding oxygen atom gains some flexibility, thus increasing the likelihood of the shielded O(H) group's removal. When both tetrahedral atoms are removed, the bond of interest becomes even more accessible.

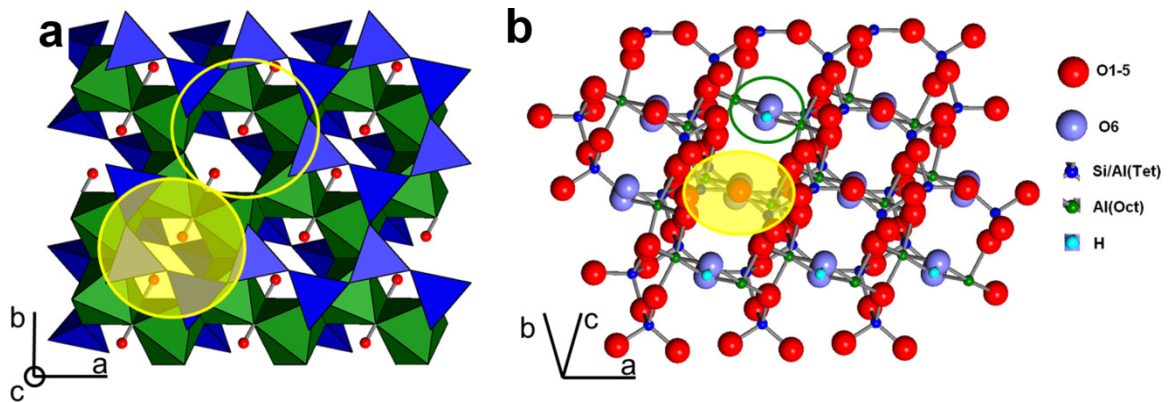


Figure 3-3. Geometric accessibility of basal plane hydroxyls (red spheres represent H-atoms): a semi-transparent circle refers to a “hardly accessible” state; an open circle refers to an “accessible” state. (a) Polyhedral representation. (b) “Ball and stick” model.

Therefore the dissolution probabilities corresponding to the different steric accessibility states are corrected according to the number of “shielding” tetrahedral atoms (0-2):

$$P_{OH_i} = P_i \cdot W_{OH}(n); n = 0,1,2 \quad (3-15).$$

3.3.2.5. Lattice defects

A large variety of lattice defects are present in micas, including planar defects (stacking faults, grain boundaries), point defects, edge and screw dislocations (Ame-linckx, 1952; Baronnet, 1972; 1975; Sunagawa and Koshino, 1975; Corny et al., 1976; Baronnet et al., 1981; Pandey et al., 1982; Sun and Baronnet, 1989; Hoche et al., 1999; Nespolo, 2001; Kogure and Inoue, 2005). These crystal imperfections induce lattice strain and promote preferential dissolution of the atoms in the vicinity

of a dislocation. Morphology of dissolution features may indicate the nature of the dislocation. For example, monolayer pits frequently observed on the mica surface can arise from point defects, while multilayer pits can be formed from the screw dislocations running along the c^* direction. Thus in the algorithm procedure the removal of a few atoms from one TOT layer simulates opening of an atomic-sized hole, while their sequential removal along a suggested screw dislocation line simulates opening of a hollow core. We applied this strategy to introduce point defects and screw dislocations through the hollow core opening performed before the simulation's start.

3.3.2.6. System size

The size of the model system is an important parameter for any atomistic simulation. The relationship between length, scale, and distribution of reactivity is a critical aspect of understanding surface reactivity at the microscopic scales. Observations of reacting mineral surfaces made with AFM and VSI (Brandt et al., 2003; Kurganskaya et al., 2012) show significant heterogeneity in the distribution of reactivity and related surface features (dislocations, etch pits, steps, etc.). Thus the choice of the system size is important for proper characterization of mineral dissolution kinetics. Ideally, the larger the system, the better it can represent the macroscopic surface. This model addresses these issues by significantly increasing the size of the modeled system compared to earlier simulations for silicate structures (Zhang and Luttge, 2008; 2009a;b) from $60 \times 60 \times 60$ unit cells to $700 \times 700 \times 7$ unit cells (since the length of the translational vectors along a^* and b^* directions is not

equal, this number can be modified to 1000x500x7, if there is a need to simulate a square surface). This size is consistent with the distribution of surface features most frequently observed with AFM (Kurganskaya et al., 2012): etch pits of 0.5-1 microns in diameter and 1-15 nm in depth.

3.3.2.7. Simulation algorithm

A Kinetic Monte Carlo program simulates a series of discrete reaction events in the atomic system. The simulations presented here employ so-called “divide and conquer” (Meakin and Rosso, 2008) or “N-fold” (Bortz et al., 1975) algorithm. In this approach, all surface sites are divided into i types (Fig. 3-4a).

The number of the atoms (surface sites) belonging to each dissolution reaction type is followed as N_i during the simulations. If the probability of an atom in the state i to dissolve is P_i , then the probability of a reaction i to happen in the whole system (or “integrated probability”) is equal to

$$INTP_i = \frac{N_i \cdot P_i}{\sum_{i=1}^n N_i \cdot P_i} \quad (3-16).$$

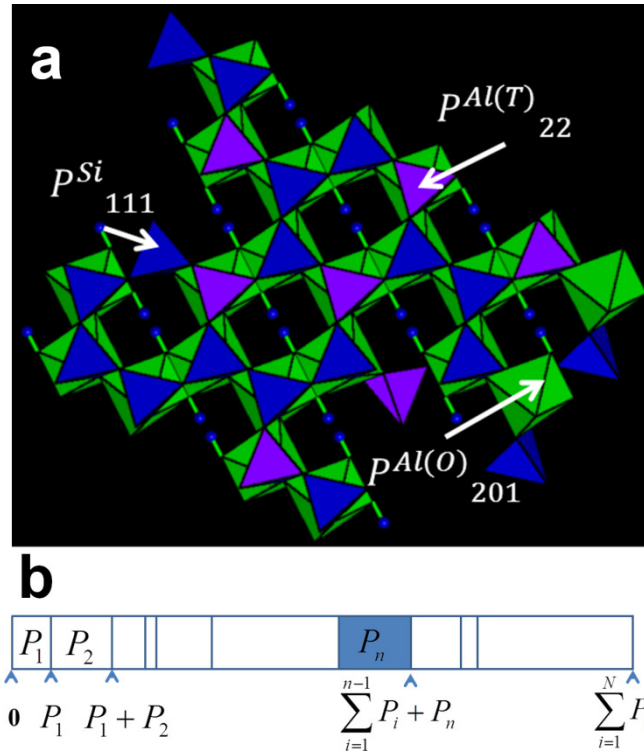


Figure 3-4. An illustration to Kinetic Monte Carlo algorithm. (a) Dissolution probabilities assigned to the different surface sites of muscovite. (b) Schematic structure of the probability interval used to make a decision about reaction type selection. The length of an each subinterval corresponds to P_i probability value. A random number $0 < x < 1$ falling into subinterval P_i defines a reaction type i to happen at the given iteration step.

Each P_i refers to the one reaction type defined by the chemistry, structural position, and coordination numbers of a surface site (Fig. 4A). At each iteration step the reaction type i is chosen if the inequality

$$\sum_{j=1}^{i-1} INTP_j < x < \sum_{j=1}^i INTP_j \quad (3-17)$$

is satisfied. Here x is a random number ($0 < x < 1$) generated at each iteration step. Graphically this scheme of reaction type selection can be represented by a bar (probability interval) divided into the vertical stripes (Fig. 3-4b). The width of each stripe represents the P_i value. The i^{th} interval that contains the random number generated (a selection criterion is given by eq. 3-3 – 3-17) defines the i^{th} reaction type at the given iteration time step. Once the reaction type is defined, an atom belonging to it is randomly chosen and removed from the system. The time interval Δt separating these two consecutive events is not constant, and depends on the current surface configuration:

$$\Delta t = -\frac{1}{v \sum_{i=1}^n N_i \cdot P_i} \ln(x) \quad (3-18).$$

Algorithms of this type are referred to as adaptive time step methods, and probabilities which have already been normalized to the reaction attempt frequencies (v , eqs. 3-1 – 3-15) have to be renormalized (eq. 3-16) at each iteration step. In the simulation, the duration of the selected reaction type is computed according to eq. 3-18 and is thus an “integrated” probability, in contrast to probabilities timed by $1/v$ interval (eqs. 3-1–3-15).

3.3.3. Model parameterization by experimental data

The formulation of the dissolution probabilities used in this study assumes a transition state theory (TST) formulation for bond hydrolysis reactions. Thus, activation energy parameters ideally should be derived from the corresponding elec-

tronic structure calculations of the energetic difference between the reactants and the transition state. These calculations must be done for each type of bond. However, such studies are scarce and activation energy values can be found in only a few papers (e.g., Pelmenchikov et al., 2000; Criscenti et al., 2006; Nangia and Garrison, 2008; Morrow et al., 2009). In order to overcome this problem, we used the following strategies. For the FCS class of models we used fixed *ab initio* - derived energies for the available bond types and obtained the rest through an empirical approach, i.e., the systematic variation of the values and subsequent comparison of the simulated results, specifically, the calculated etch pit structures with the experimentally observed ones. The values of the weighting coefficients were found by using the same fitting procedure. The parameter values for the SCS class of models were obtained through a similar process, i.e., the iterative variation of all parameters that had been conducted until the desired match between simulated and experimentally observed etch pit morphologies was reached.

For the KMC model parameterization comparison, we used the topography of the reacted muscovite surface measured using the AFM (Kurganskaya et al., 2012). The dissolution probabilities for the KMC model were calculated for following settings: $T=155^{\circ}\text{C}$, $\text{pH}=9.4$, far-from-equilibrium conditions.

Acidity of the aqueous environment is one of the important factors that control the dissolution rate. The charge of the reactive surface groups depends critically on the pH, i.e., low values favor protonation of bridging oxygen atoms and induce positive charge, while high pH values favor deprotonation of surface groups that be-

come negatively charged. For our modeling we assume an alkaline pH in which all dangling M-O- bonds are completely deprotonated. Thus, we used the activation energy values of Morrow et al. (2009) calculated for deprotonated sites (Table 3-3). We optimized other model parameters to the values that produce the best fit between simulated and experimentally obtained etch pit structures. The full set of parameters used for FCS complexity level is shown in Table 3-3. Another set obtained through the same procedure for SCS level is presented in Table 3-4.

The optimized parameter values (Tables 3-3 and 3-4) do not necessarily reflect real values of activation energies. However, the fact that we routinely produce morphologies that are in excellent agreement with experimentally observed etch pit morphologies is a strong argument that we used the “correct” ratios between the probabilities of formation of the kinetically important surface sites.

Table 3-3. Energetic parameters used in the First Coordination Sphere (FCS) complexity level of the KMC model.

Bond type	Si-O-Si	Al(T)-O-Si	Si-O-Al(O)	Al(T)-O-Al(O)	Al(O)=O=Al(O)
$\Delta E/kT$	31 ^a	22 ^a	10 ^a	9	15
First coordination sphere	T(center)-T _i	T(center)-O _i	O(center)-T _i	O(center)-O _i	
$\Delta E^1_{M_i-M_j}/kT$	4	3	2	1	
$\Delta E_{OH}/kT$	1				

^aMorrow *et al.*, 2009

Table 3-4. Energetic parameters used in SCS complexity level of the KMC

model.

Bond type	Si-O-Si	Al(T)-O-Si	Si-O-Al(O)	Al(T)-O-Al(O)	Al(O)=O=Al(O)
$\Delta E/kT$	14	8	2	1	5
First coordination sphere	T(center)- T_i	T(center)- O_i	O(center)- T_i	O(center)- O_i	
$\Delta E^1_{Mi-Mj}/kT$	5	5	3	6	
Second coordination sphere					
$\Delta E^2_{Mi-Mj}/kT$	5	2.5	1	3	
$\Delta E_{OH}/kT$	1				

3.4. Results

The model results have been broadly organized as sensitivity tests by selectively combining the various correction terms to highlight their specific roles. These combinations are denoted by abbreviations according to the following scheme: (a) First Coordination Sphere (FCS) level considers only the first nearest neighbors and includes (a1) Simple First Coordination Sphere (SFCS) version ignoring lattice resistance effects (only eqs. 3-1 – 3-7 are applied); (a2) Weighted First Coordination Sphere (WFCS) level considering lattice resistance (eqs. 3-8 – 3-10); (b) Second Coordination Sphere (SCS) level considers effects of first and second nearest neighbors as well as lattice resistance effects (eqs. 3-11–3-14); (c) (SF/WF/S)CS-H denotes versions considering “hydroxyl orientation” effect (eqs. 3-15). These four complexity levels (referred to as (a1),(a2),(c),(d)) thus range from the simplest application of correction to the most complex. The capabilities of each level to reproduce observed etch pit features, which provide insight into their origins, are described below.

3.4.1. Etch pit structure: general features

3.4.1.1. Monolayer pits

Experimentally observed monolayer oval-shaped pits (Fig. 3-5a) were produced in the simulations by restricting dislocation depth to a single TOT layer. The elongated shape of the pit indicates the existence of the fastest dissolution direction. According to the simulation results (Fig. 3-5b), the pits are oriented along [110] direction in the even layers and along the same direction rotated by 120° in the odd layers (Fig. 3-5c). This change of pit orientation from layer to layer is caused by the interlayer rotation in $2M_1$ mica polytype. The particular orientation of the pits is caused by anisotropic step velocities in different crystallographic directions and generally can be considered as a function of the lattice structure and environmental conditions. The orientations shown on Fig. 3-5 are firmly produced using all model versions and the parameters shown in Tables 3-3 and 3-4.

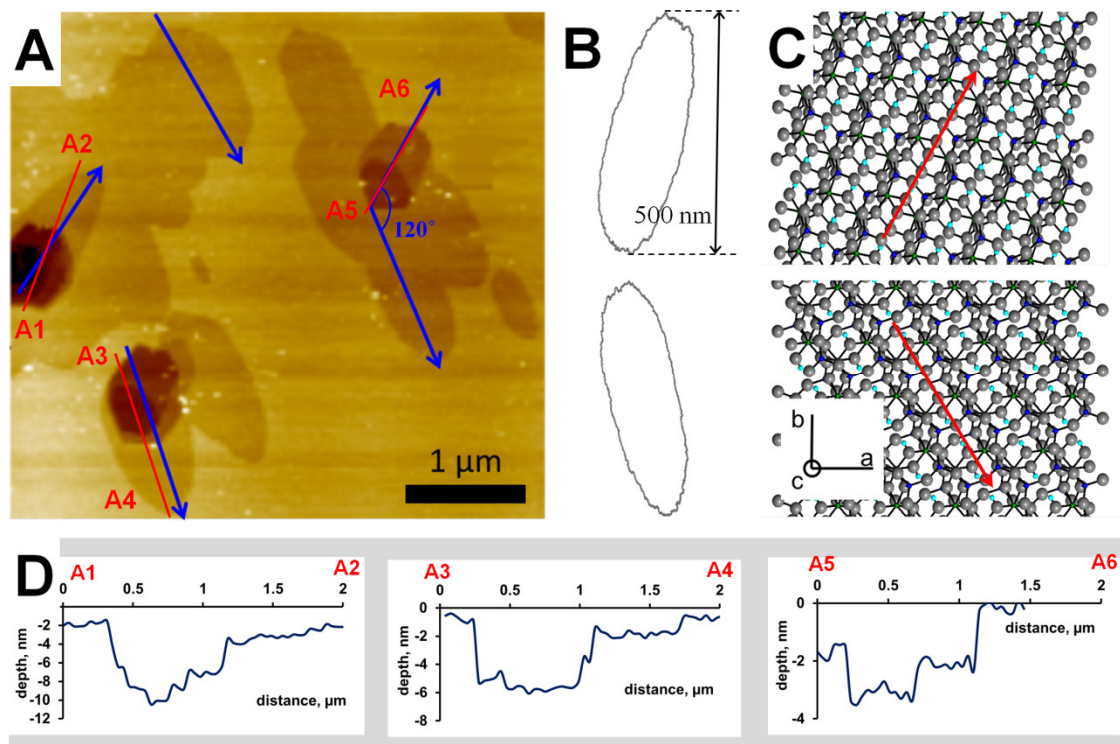


Figure 3-5. Two principal orientations of monolayer etch pits. (a) Experimentally obtained AFM data (Kurganskaya et al., 2012). Blue arrows show main pit orientations. Red lines refer to etch pit profiles A1-A2, A3-A4 and A5-A6 shown on (d). (b) Contours of etch pits obtained in KMC simulations: pits of the upper type appear in the 1st type of TOT layer; pits of the lower type appear in the 2nd type of TOT layer (SFCS version of model is used, energetic parameters are shown in Table 3-3). (c) Models of the two TOT layers in muscovite structure. Red arrows show directions of the fastest etch pit growth. (d) Profiles through the three pits shown on (a), letters A1-A6 mark the ends of the profiles.

3.4.1.2. Multilayer pits

3.4.1.2.1 Shift of the pit center

A characteristic feature found for etch pits having two or more layers is the shift of the deeper pit to one of the corners of an upper pit (Fig. 3-6c). This shift indicates that there is a significant difference in the dissolution rates along the main dissolution direction. As a working hypothesis, we assume that this phenomenon reflects the specific Al-OH-Al bond orientation, which therefore imposes variable restrictions on its accessibility along the main dissolution direction. Results of simulations with and without corrections for geometric Al-O-Al bond accessibility are shown on Fig. 3-6. Without accessibility corrections, pits grow at the same velocities in opposing directions from the pit center. As a result, the steps formed by the sides of the underlying pits have a symmetry center matching the dislocation core (Fig. 3-6a). In contrast, "OH-orientation" corrections made at (SF/WF/S)CS-H levels allow them to reproduce the characteristic shift of the deeper pits to the left lower corner of the uppermost pit (Fig. 3-6b). The shift is caused by the difference in step velocities at the upper and lower ends of pits. Since "shielded" steps are formed at the lower end of the pits in the even layer (Fig. 3-3) and upper end in the odd layer, the pits grow in $[110]$ "+" direction in the even layers and in $[1\bar{1}0]$ "-" direction in the odd layers (see Fig. 3-6b for details). This characteristic shift was also observed using SCS level without "OH-orientation" corrections or setting the corresponding parameter value $\Delta E_{OH}/kT$ to 0, but with the smaller magnitude.

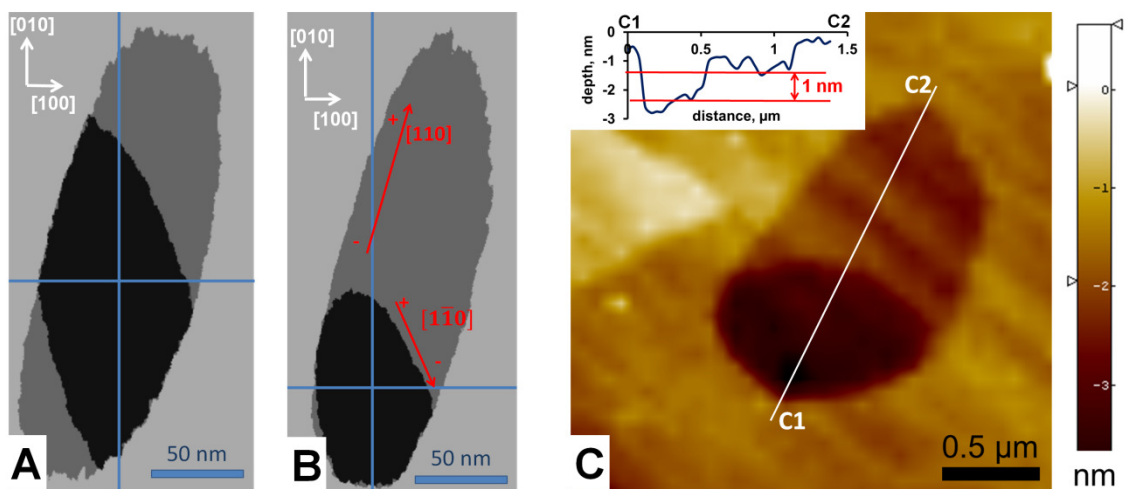


Figure 3-6. Etch pit morphology with (b) and without (a) $\text{Al(O)}=\text{O}=\text{Al(O)}$ bond orientation corrections (see in text). Activation energy parameters ($\Delta E_a/kT$) are provided in Table 3-3. (a) The result of the KMC simulation without “hydroxyl orientation” corrections (SFCS version). The geometric center of the pit matches to the dislocation core position. (b) KMC simulation result for SFCS-H version. (c) A colormap of a two-layered etch pit on muscovite (001) face dissolved in water with $\text{pH}=9.4$, $T=155^\circ\text{C}$ (AFM data, Kurganskaya et al., 2012). White line marks C1-C2 profile through the pit.

This effect happens due to the step velocity difference between the steps at the etch pit's upper and lower ends induced by the use of the second-order neighbors. Thus, the causes of this effect can be understood from the difference in topology and reactivity of the sites along these steps. We assume that both effects of steric accessibility and difference in lattice resistance introduced by the second order neighbors in the opposite directions may influence the enhanced reactivity in one specific direction and the resulting shift of the pit center.

3.1.2.2. Zigzag pattern

Another characteristic feature of multilayered pits observed in experiments is the interlacing of steps, producing a well-defined “zigzag pattern” (Figs. 3-7a, 3-7b). This pattern has been documented in experiments involving phyllosilicate growth and dissolution, for minerals having interlayer rotation in their structure (Snowden-Ifft et al., 1993; Nagahara et al., 1994; Kuwahara et al., 1998; 2001; Al-dushin et al., 2006b; Kurganskaya et al., 2012). Baronnet (1972) studied interlacing patterns formed during spiral growth of different structural polytypes of mica. He showed that growth spirals of minerals belonging to the $2M_1$ group exhibit a zigzag pattern, in which the steps intersect at an angle of 120° . A detailed explanation of the mechanism of this pattern formation was provided by Kuwahara *et al.* 1998; 2001) for spiral growth of illite particles. He concluded that the rotation of odd and even TOT layers by 120° in the $2M_1$ polytype causes a characteristic interlacing of the steps.

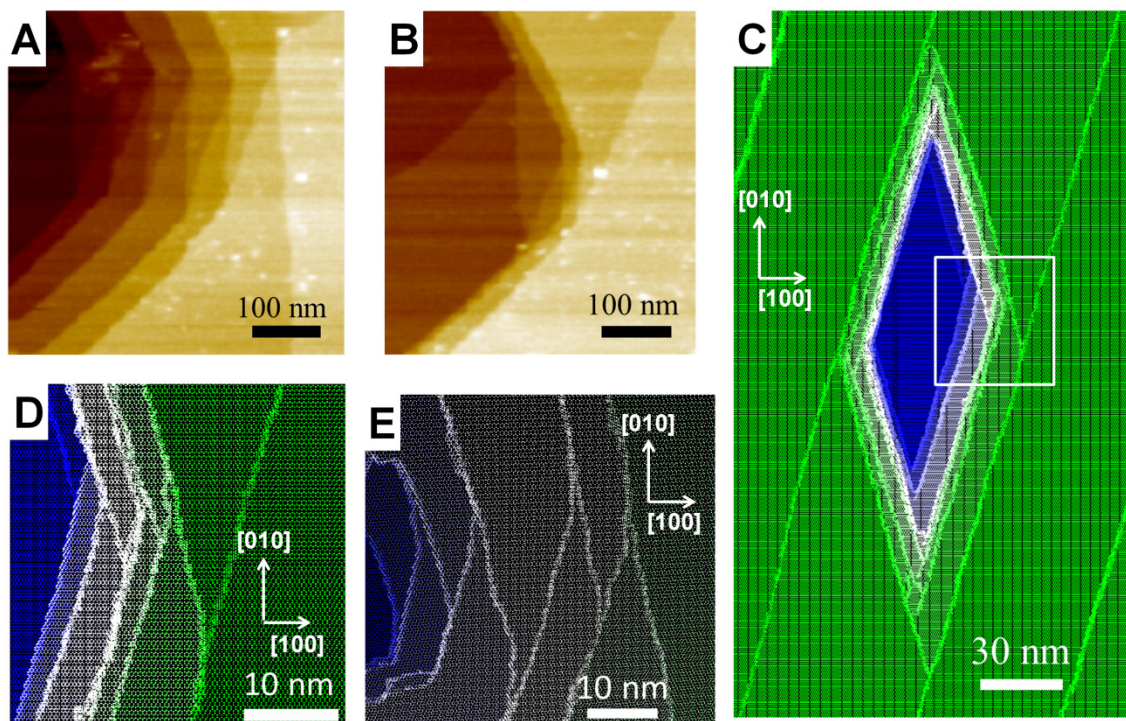


Figure 3-7. Zigzag pattern formed on the muscovite (001) face. (a),(b) Patterns observed on the muscovite surface dissolved in water (pH=9.4; T=155°C, Kurganskaya et al., 2012). (c) An etch pit with the four zigzag patterns produced in KMC simulations of muscovite dissolution (SCS-H version). Activation energies for bond breaking, second order neighbor and hydroxyl orientation corrections are presented in Table 4, the first order corrections are $\Delta E^{1_{T-T}}/kT = 6$, $\Delta E^{1_{T-O}}/kT = 6$, $\Delta E^{1_{O-T}}/kT = 6$, $\Delta E^{1_{O-O}}/kT = 4$. (d) Enlarged inset of the rectangular area shown on (c). (e) Zigzag pattern with curved steps obtained in KMC simulations (enlarged inset from Fig. 3-9a). Parameter values for this simulation are shown in Table 3-4.

According to the mechanism proposed, a polygonal illite particle has hexagonal morphology with the zigzag pattern appearing at four locations. In our experimental observations this pattern is observed only at the one right hand side, primarily because of the pit shift to the lower right corner or upper left corner, depending on the uppermost pit orientation. However, if the shift is quite small, then all four instances can be observed at the corners of parallelogram-shaped pits produced in KMC simulations (Fig. 3-7c).

The detailed structure of this pattern is exactly the same as described by Baronnet (1972) and Kuwahara et al. (1998): two sequences of parallel straight steps intersecting at the crystallographic angle (Fig. 3-7d). The zigzag patterns that we observed in our experiments (Kurganskaya et al., 2012) have a more complex structure (Figs. 3-7a, 3-7b). The two systems of straight parallel steps change their orientation towards one other and form an additional (seventh) short side in a polygonal etch pit (Fig. 3-9b). The same effect is observed in the case where the lateral step separation is extremely small and the steps are visible only in the zigzag pattern area (Fig. 3-7b). This effect can be produced in KMC simulations where polygonal or pseudo-hexagonal pits are formed (Figs. 3-7e, 3-9a). We hypothesize that this feature arises from the specific overlay of six-sided 2D pits, which influence one another during dissolution in such a way that the steps begin to change their orientation from that which is crystallographically controlled in the zigzag region. The process responsible for this 2D pit interaction cannot be identified with precision. However, we can suggest two possible explanations: (i) the pits grow independently in each layer, and their growth is limited only by the overlying TOT layers. The

change of the step orientation is thus caused by the dynamics of independent etch pit growth in its own layer; Alternatively, (ii) the restriction on the pit growth in the “covered” area brings about the change in step orientation, which breaks the “normal” reaction sequence. We favor the latter explanation, as we observed some traces of step orientation change even in the case of parallelogram-shaped pits (Fig. 3-7d), where only one step direction in each layer is possible. In the case of six-sided pits where three directions in each layer are stable, this effect is more pronounced (Fig. 3-7e).

3.4.2. Step morphology, orientation and stability

3.4.2.1. First coordination sphere level of complexity

Simulations made at the first coordination sphere complexity level (FCS) can predict some basic features of the pits; for example, orientation, 2D pit superposition, and zigzag pattern. However, the model at this level have one major disadvantage: straight steps can be formed only along “major” $[110]$ direction, while in the experiments we observed steps oriented along $[1\bar{1}0]$ and $[100]$ directions in the even TOT layers, but rotated by 120° in the odd layers (Kurganskaya et al., 2012). The traces of these steps can definitely be detected, but these pseudo-steps are typically poorly formed (Figs. 3-8a, 3-8b).

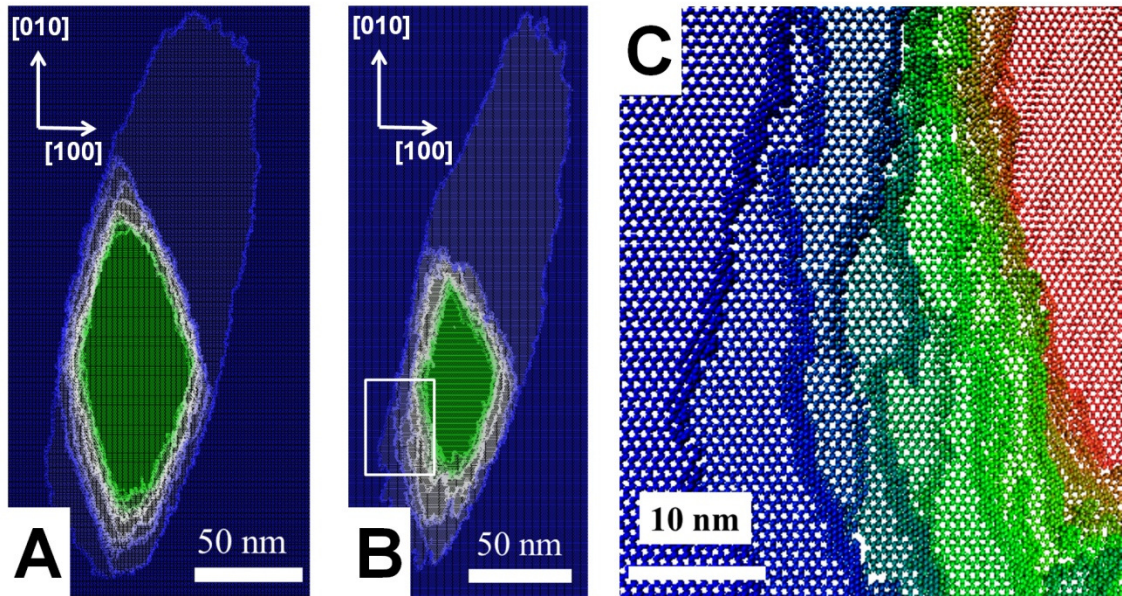


Figure 3-8. Etch pits obtained in KMC simulations (FCS-H version) (a) Structure of an etch pit produced with SFCS-H version; (b) A pit produced with the same parameters using WFCS-H version. (c) Inset from Fig. 3-8b showing detailed step morphology. Modeling parameters are shown in Table 3-3.

Another problem associated with this level is that steps may develop additional roughness due to the formation of elongated clusters and rings along the step edge. As a result, saw-shaped steps with “teeth” and long “peninsulas” are formed (Fig. 3-8c). The size of the “teeth” ranges from 1-2 unit cells (0.5-1 nm) to 10-20 unit cells (5-10 nm). It is interesting that similar step morphology was observed in the experiments with muscovite etched in 48% HF (Snowden-Ifft et al., 1993). Nevertheless, the use of the model at FCS level can (depending on modeling parameters)

lead either to the formation of parallelogram-shaped pits with straight steps (Figs. 3-7c, 3-8a) or to rough, saw-tooth steps forming rounded or pseudo-hexagonal pits. The use of the weighted version (WFCS), which introduces a dependence of bond hydrolysis activation energy on the number of nearest neighbors due to the lattice resistance effect, fails to improve these results. This version generates only simple redistribution of dissolution event probabilities, leading to the same parallelogram-shaped or semi-round pits having rough steps (Figs. 3-8b, 3-8c).

3.4.2.2. Second coordination sphere level of complexity

The use of the SCS level of complexity substantially reduces the formation of saw-teeth or “rings” along the steps, and corrects the problem of stabilization of straight steps along the $[1\bar{1}0]$ and $[100]$ directions. As a result, faceted etch pits resembling those observed in the experiments can be produced (Fig. 3-9a, 3-9b).

The reduction of the step roughness is clearly caused by the difference in dissolution probabilities for the sites at the well-defined steps and small clusters and rings frequently forming along the step. The enhanced dissolution of the smaller clusters is consistent with *ab initio* calculations of bond hydrolysis activation energies for the clusters of different sizes (Criscenti et al., 2006).

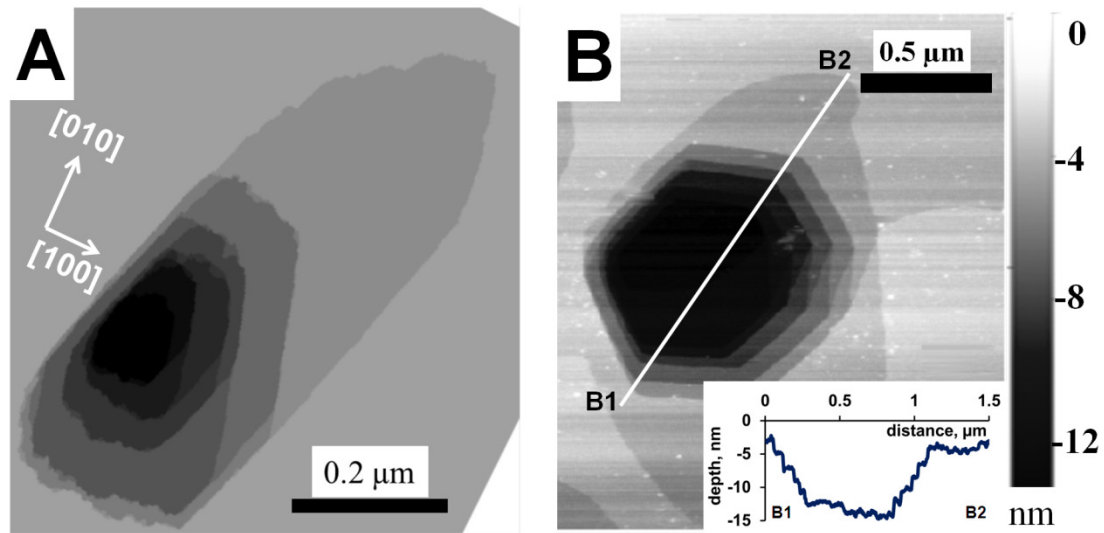


Figure 3-9. Morphology of a multilayer pit growing on muscovite (001) face. (a) A polygonal etch pit produced in KMC simulations (SCS-H version), see Table 3-4 for energetic parameters. (b) A multilayer etch pit obtained from experiments (AFM data, Kurganskaya et al., 2012). White line marks B1-B2 etch pit profile.

3.5. Discussion

3.5.1. $\{hk0\}$ face stability

The problem of differential stability of $\{hk0\}$ phyllosilicate faces in the dissolution process has been investigated previously in a series of theoretical and experimental studies (White and Zelazny, 1988; Bosbach et al., 2000; Bickmore et al., 2001; Bickmore et al., 2003). White and Zelazny (1988) proposed application of the theory of periodic bond chains (PBCs, Hartman and Pedrock 1955a;b;c) to explain the structure of phyllosilicate edges. Bosbach et al. (2000) and Bickmore et al. (2003) developed this approach in order to explain the morphology of dissolving

nontronite and hectorite grains. In PBC theory, the basic idea is that the crystallographic faces that prevail during mineral growth or dissolution are those defined by chains of the strongest bonds. Phyllosilicate edge faces are formed by the PBCs running along $[110]$, $[1\bar{1}0]$, and $[100]$ directions, and occasionally along $[010]$ and $[130]$ (Bickmore et al., 2001). These faces are primarily responsible for the appearance of particles (e.g. nontronite, Bickmore et al., 2001) as well as the shape of etch pits (Kurganskaya et al., 2012) forming on (001) faces of dioctahedral phyllosilicates. In addition, Bleam et al. (1993) calculated surface Coulomb energies of pyrophyllite edge faces and found that the $[110]$ face, defining etch pit orientation, has the minimum energy. The results of our KMC simulations generally are in a good agreement with the predictions for the stable face orientation made using the PBC theory (White and Zelazny, 1988; Bickmore et al., 2001), *ab initio* calculations (Bickmore et al., 2003) and Coulomb energy calculations (Bleam et al., 1993). Based on this agreement we propose an additional explanation for the step stability discussed in the next subsection.

3.5.2. Topology of ledge and kink sites

The energy, stability, and reactivity of faces are determined by the reactivity of their respective sites. The reactivity of a given site is in turn defined by its connectivity number (i.e., number of the first and second order tetrahedral and octahedral nearest neighbors: $N_{T1}, N_{O1}, N_{T2}, N_{O2}$) and its steric factors. The connectivity number of the octahedral sites forming (110) face (and $[110]$ step on the basal face) is $(4,2,6,4)$, while the connectivity number of octahedral sites forming $(1\bar{1}0)$ and (100)

faces is (3,2,5,4) (Fig. 3-10; Table 3-5). The dissolution probability of each site depends not only on connectivity but also on the chemistry of the tetrahedral sites. Because the distribution of tetrahedral Al atoms is random, the fraction of tetrahedral Al sites along the step must be similar for all types of the steps. Therefore, the probability of the octahedral ledge (step) sites to dissolve is generally smaller for the (110) face than for the ($1\bar{1}0$) and (100) faces. The use of the FCS level of the KMC model clearly minimizes the dissolution rate in directions perpendicular to the (110) face, because the first coordination numbers for this face are the largest. As a result, the preferential dissolution direction along the (110) face is established. However, the step site connectivity alone cannot explain preferential stability of some particular steps. Moreover, it cannot explain why ($1\bar{1}0$) and (100) faces become stable only when including second order interactions (SCS level).

The problem of larger diversity of stable steps formed as an outcome of the models considering second coordination sphere has been discussed by Kohli and Ives (1972) in their model dissolution of Kossel crystals. They used (N1,N2) notation to classify surface sites, where N1 and N2 are numbers of the first and second order neighbors. In particular, they pointed out that differentiation between the kink sites with the coordination numbers (3,6) and (3,7) is critical for the formation of the steps other than the “major” $\langle 10 \rangle$.

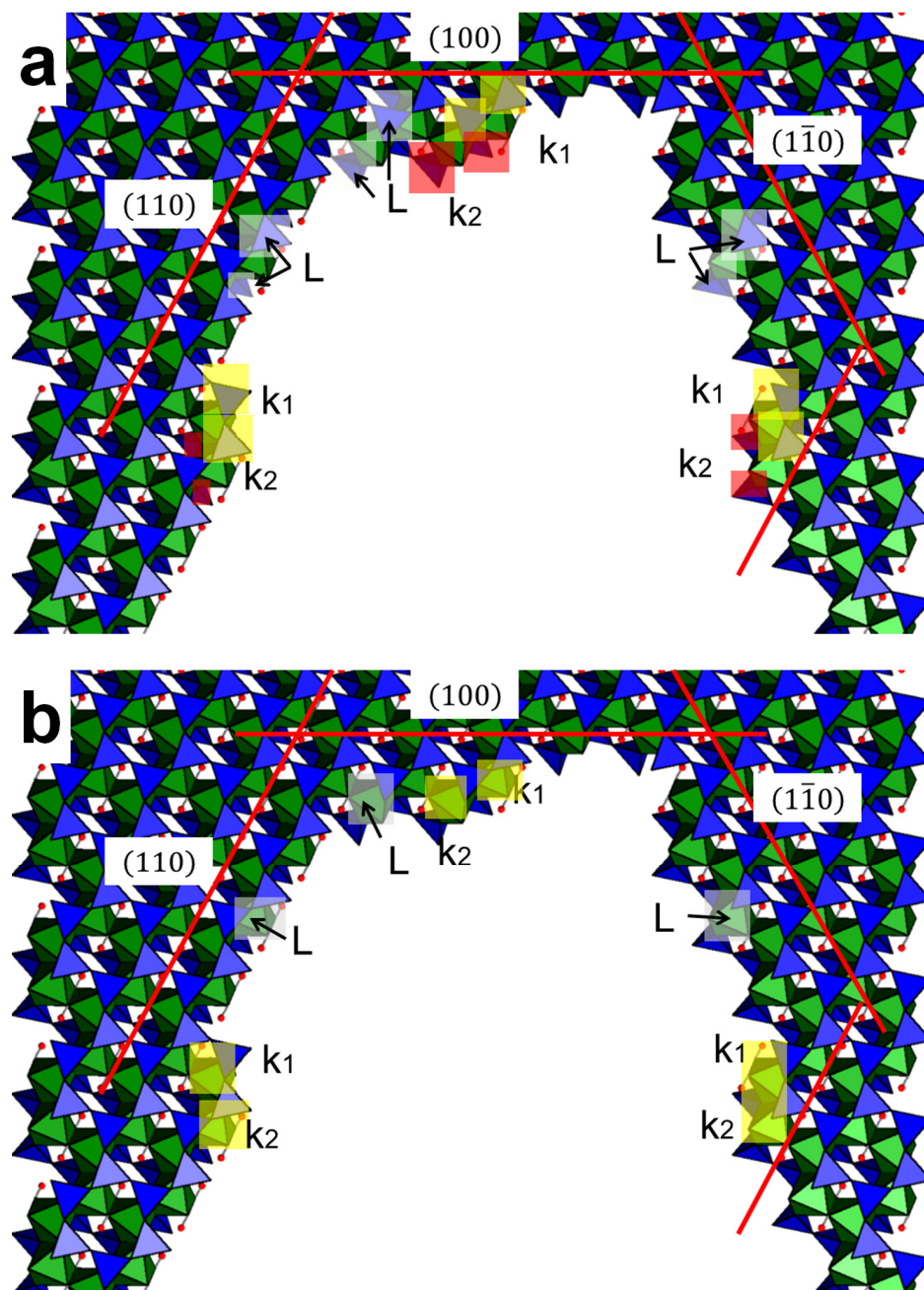


Figure 3-10. Ledge (step) and kink sites at (110) , $(\bar{1}\bar{1}0)$, and (100) faces of muscovite. The example sites are labeled by semitransparent squares, yellow and red for the kink sites, light gray for the ledge sites. The front kink sites are labeled as k_1 , the back kink sites are labeled as k_2 . (a) Tetrahedral sites. Upper kink sites are high-

lighted by yellow squares, lower kink sites are highlighted by red squares. (b) Octahedral sites.

Table 3-5. Coordination numbers for the muscovite “kink” and “step” sites shown on Fig. 3-10. The numbers are shown in order $N_{T1}, N_{O1}, N_{T2}, N_{O2}$, or the number of first tetrahedral nearest neighbors, the number of first octahedral nearest neighbors, the number of second tetrahedral neighbors and the number of the second octahedral neighbors correspondingly.

<i>Layer type</i>	<i>Site type</i>	<i>Face index</i>		
		(110)	($\bar{1}\bar{1}0$)	(100)
Octahedral	Ledge(step) site	4,2,6,4	3,2,5,4	3,2,5,4
	Kink site 1 (front)	3,2,4,3	4,2,5,3	4,2,5,3
	Kink site 2 (back)	4,2,5,3	3,2,4,3	3,2,4,3
Tetrahedral	Upper ledge(step) site	2,2,4,3	2,2,4,3	2,2,4,3
	Lower ledge(step) site	2,2,4,3	2,1,4,2	2,1,4,2
	Upper kink site 1 (front)	2,1,3,2	2,2,3,3	2,2,3,3
	Upper Kink site 2 (back)	2,2,3,2	2,2,3,2	2,2,3,2
	Lower kink site 1 (front)	2,2,3,2	2,2,3,2	2,2,3,2
	Lower Kink site 2 (back)	2,2,3,3	2,1,3,2	2,1,3,2

In a treatment analogous to the Kossel crystal, we can define different “kink” and “ledge” octahedral and tetrahedral sites on muscovite surface. “Ledge” sites are defined as the sites forming a straight step along a PBC. “Kink” sites are defined as the sites belonging to the stable elementary periodic units (clusters) whose removal will not change the number of “kink” sites on the surface nor break the step structure. We refer to these units as kink site groups. These elementary units shown in

Fig. 3-10 consist of two octahedral and four tetrahedral “kink sites,” two upper and two lower. The connectivity numbers for these sites presented in $N_{T1}, N_{O1}, N_{T2}, N_{O2}$ format are provided in Table 3-5. In general, there are two types of kink sites within a kink site group, front (k_1) and back (k_2). The corresponding front and back octahedral kink sites formed along $[110]$ direction have connectivity numbers $(3,2,4,3)$ and $(4,2,5,3)$. Therefore, the front octahedral kink site of the (110) face is more reactive than the back one. Thus the dissolution starts from the front kink site. However, the front octahedral kink sites of the steps $[1\bar{1}0]$ and $[100]$ have connectivity numbers $(4,2,5,3)$, as k_2 for the (110) face does. Because the dissolution begins at the most reactive site, the back-kink for these faces must dissolve first. The situation with the tetrahedral kink sites is quite symmetrical: the most reactive kink having connectivity $(2,1,3,2)$ can be found at the front of the (110) “kink site” group and at the back of the $[1\bar{1}0]$, $[100]$ kink site group. Therefore, the kink site group along $[110]$ steps dissolves from front to back, while this same group dissolves from back to front at $(1\bar{1}0)$ and (100) faces. However, regardless of the order of different kink site dissolution within a one kink site group, it still represents the most reactive cluster that dissolves as a whole unit. The resulting propagation of the kink site groups along the steps is mechanistically analogous to the propagation of the 3-coordinated kink site along the 4-coordinated ledge site in Kossel crystal, since the reactivity of the system does not change.

The kink site groups shown in Fig. 3-10 at (110) and (100) faces refer to the “right” type (oriented at the right hand site looking to the pit center from the step), while the kink site group shown for the $(1\bar{1}0)$ face belong to the “left” type. General-

ly, the removal of a ledge site from a step results in formation of a double kink, or two kink sites: “right” and “left”. The connectivity numbers for the “left” and “right” octahedral kink sites are symmetrically equivalent: “right” k_2 octahedral sites attain connectivity of “left” k_1 and vice versa. The switch of dissolution order within a kink site group for tetrahedral kink sites would be more complex and depend on the crystallographic direction. Regardless of the “kink site group” type, left or right, it would be dissolved as a whole unit. The steps shown on Fig. 10 also have their symmetric counterparts having opposite sign, where step and kink sites have slightly different topology.

The connectivity numbers for the most reactive octahedral kink sites, k_2 , and ledge site for the faces $(1\bar{1}0)/(100)$ are $(3,2,4,3)$ and $(3,2,5,4)$ correspondingly. The numbers for the most reactive tetrahedral sites are the following: $(2,1,4,2)$ for the lower ledge sites and $(2,1,3,2)$ for the lower back kink sites. The kink site differentiation from the step site is ultimately based on the second order connectivity numbers. Generally, the step stabilization is primarily defined by the ratio between the probabilities of “kink site” nucleation and propagation. Consideration of the second order effects is vital for the $[1\bar{1}0]$, $[100]$ step stability, since it induces the important distinction of the kink and ledge sites along these faces. In contrast, octahedral ledge and kink sites along the $[110]$ direction have $(4,2,6,4)$ and $(3,2,4,3)$ connectivity numbers. Therefore, this step is formed in the simulations produced by any version of model and is thus a primary direction for step motion. The second coordination sphere plays a vital role in stabilization of the steps along $[1\bar{1}0]$, $[100]$ directions,

while the stability of the [110] step can be supported if we use only the first order neighbors to describe surface site topology.

3.5.3. Morphology of etch pits

The identification of specific kink and step sites and their role in the kinetic process is crucial for the understanding of step and stepwave propagation mechanisms as well as for the explanation of step roughness and curvature observed in experiments. The anisotropic shape of etch pits (Fig. 3-5A) stems from the difference in step velocities, where the steps oriented along the [110] direction in an even layer and the step oriented along the $[1\bar{1}0]$ direction in an odd layer have the slowest velocity. The step velocity depends on two parameters, i.e., rates of kink site nucleation and propagation. Both rates are defined by the topologies of these sites and the activation energies of the bond breaking processes. The combination of both types of parameters at the simulated conditions leads to the following order of step velocities in the even layer: $[110] < [1\bar{1}0] < [100]$. Another order can be derived for the odd layer: $[1\bar{1}0] < [110] < [100]$. The enhanced coalescence of the pits along the two main dissolution directions ($[110]$ and $[1\bar{1}0]$) is likely to cause the formation of dissolution stripes, observed experimentally in VSI data (Kurganskaya et al., 2012). These stripes intersect at an angle of 120° , as the vectors of etch pit orientation in two different mica layers (Fig. 3-5C).

3.5.4. Applications of the KMC model

The stochastic approach described in this work can be applied to predict and explain a large variety of experimental observations at different scales: from differential reactivity of surface sites to the surface morphologies observed by using microscopic techniques such as SEM, VSI, and AFM. Moreover, the mechanistic connections between the processes taking place at the different scales can be derived from the simulations. In particular, these model results can explain how kinetics of surface reactions at the molecular scale defines dynamics of kink nucleation and propagation, the relative velocity and directions of step movement, the detailed structure of the etch pits, mechanisms of etch pit expansion and coalescence, and related details. By incorporating the topology of surface sites for different faces, we can also access dissolution anisotropy for these faces and understand mechanisms of their interaction. Dissolution of entire particles of clay minerals can be simulated due to their small size. As a result, problems of grain or platelet dissolution morphologies as well as the dissolution kinetics of the small crystals can be better understood.

All stages of surface alteration during the dissolution reaction can be studied, from etch pit formation to retreat of the rough surface formed as a result of multiple pit coalescence.

Another important problem that can be addressed with this model is the dependence of the dissolution rate on a variety of intrinsic and extrinsic parameters (compare Fischer et al., 2012; Luttge et al., 2013): environmental conditions (pH and saturation state), dislocation network, bond topology, structure and chemical

composition of crystal lattice. However, in order to model the influence of additional parameters on the dissolution rate, e.g., saturation state or presence of inhibiting species, the step morphology and kink site statistics should be correctly produced by choosing an adequate level of model complexity and parameter values.

3.6. Conclusions

Dissolution of phyllosilicates can be successfully described and modeled with the use of a stochastic Kinetic Monte Carlo approach predicting dynamics of temporal surface evolution from the kinetics of elementary surface reactions. According to the modeling results, dissolution of these minerals proceeds via formation of etch pits at opened screw dislocation cores through movement and coalescence of step-waves. This dissolution mechanism is common for all minerals and thus enables the application of the stepwave model (Lasaga and Lutge, 2001), describing dissolution in terms of kink site and surface step movement. These conclusions are consistent with results obtained from experimental microscopic observations of reacted muscovite surface topography (Kurganskaya et al., 2012).

The morphology of etch pits observed in experiments can be predicted through consideration of the second coordination sphere, which plays an important role in step stabilization. Stable steps were observed to form along $[110]$, $[1\bar{1}0]$, $[100]$, and in rare cases along $[010]$ directions. When restricted to consideration of the first nearest neighbors only, simulations lead to formation of pits with only two parallel stable steps oriented along the $[110]$ direction. The implementation of the

first-order lattice resistance effect on bond hydrolysis leads only to the redistribution of key site dissolution probabilities but does not seriously change the spectrum of etch pit morphologies that can be formed. Probability corrections made due to the different geometric access to the basal hydroxyl help to reproduce experimentally observed dissolution rate anisotropy along [110] periodic bond chains. In general, these results demonstrate that the KMC model constitutes an effective balance between the degree of surface detail and the system size, and permit an adequate explanation of etch pit and step structure. The predictive power of the model can be optimized if rates of all surface reactions are available from *ab initio* or molecular dynamics studies. However, even in the absence of this information, the complementary use of KMC simulations and experimental data can provide new and important insights into the mechanisms of mineral dissolution.

3.7. Acknowledgements

We thank Dr. Rolf S. Arvidson for a pre-review of this manuscript and in-depth discussion that helped significantly to improve this paper. We thank two anonymous referees for their careful and encouraging reviews. A big thank you goes also to James G. Keenan, Emily Chin, Prof. Julia K. Morgan, Drs. Rolf S. Arvidson and Glenn Snyder for their language editing. We acknowledge generous support from the Global Climate and Energy Project (GCEP) at Stanford University (award # 25580430-48513-A).

3.8. References

- Aldushin K., Jordan G. and Schmahl W.W. (2006a) Basal plane reactivity of phyllosilicates studied in situ by hydrothermal atomic force microscopy (HAFM). *Geochim. Cosmochim. Acta* **70**, 4380-4391.
- Aldushin K., Jordan G. and Schmahl W.W. (2006b) Kinematics of apophyllite leaching-A terrace-ledge-link process within phyllosilicate interlayers. *J. Cryst. Growth* **297**, 161-168.
- Amelinckx S. (1952) Screw dislocations in mica. *Nature* **169**, 580.
- Bailey S.W. (1984) Micas, *Rev. Mineral.*, v. **13**.
- Baronnet A. (1972) Growth mechanisms and polytypism in synthetic hydroxyl-bearing phlogopite. *Am. Miner.* **57**, 1272-1293.
- Baronnet A. (1975) Growth Spirals and Complex Polytypism in Micas. I. Polytypic structure generation. *Acta Crystallogr.* **A31**, 345.
- Baronnet A., Pandey D. and Krishna P. (1981) Application of the faulted matrix model to the growth of polytype structures in mica. *J. Cryst. Growth.* **52**, 963-968.
- Bickmore B.R., Bosbach D., Hochella Jr., M.F., Charlet L., Rufe E. (2001) In situ atomic force microscopy study of hectorite and nontronite dissolution: implications for phyllosilicate edge surface structures and dissolution mechanisms. *Am. Mineral.* **86**, 411-423.

Bickmore B.R., Rosso K.M., Nagy K.L., Cygan R.T., and Tadanier C.J. (2003) Ab initio determination of edge surface structures for dioctahedral 2:1 phyllosilicates: implications for acid-base reactivity. *Clays Clay Miner.* **51**, No. 4, 359–371.

Bleam W.F., Welhouse G.J., and Janowiak M.A. (1993) The surface Coulomb energy and proton Coulomb potentials of pyrophyllite {010}, {110}, {100}, and {130} edges. *Clays Clay Miner.* **41**, 305-316.

Bortz A.B., Kalos M.H., and Lebowitz J.L. (1975) A new algorithm for Monte Carlo simulation of Ising Spin systems. *Jour. Compt. Phys.* **17**, 10-18.

Bosbach D., Charlet L., Bickmore B., and Hochella Jr M.F.. (2000) The dissolution of hectorite: In-situ, real-time observations using atomic force microscopy. *Am. Mineral.* **85**, 1209-1216.

Blum A.E. Lasaga A.C. (1987) Monte Carlo Simulations of Surface Reaction Rate Laws, in *Aquatic surface chemistry* (John Wiley & Sons, 1987), pp. 255-292.

Brandt F., Bosbach D., Krawczyk-Barsch E., Arnold T. and Bernhard G. (2003) Chlorite dissolution in the acid pH-range: A combined microscopic and macroscopic approach. *Geochim. Cosmochim. Acta* **67**, 1451-1461.

Corny F., Baronnet A. and Jourdan C. (1976) X-ray topographic studies of as-grown defects in natural muscovite. *J. Cryst. Growth* **34**, 304—315.

Criscenti L.G., Kubicki J.D., and Brantley S.L. (2006) Silicate Glass and Mineral Dissolution: Calculated Reaction Paths and Activation Energies for Hydrolysis of a Q3 Si by H₃O⁺ Using Ab Initio Methods. *J. Phys. Chem. A* **110**, 198-206.

Diego Gatta G., McIntyre G.J., Sassi R., Rotiroti N., and Pavese A. (2011) Hydrogen-bond and cation partitioning in muscovite: A single-crystal neutron-diffraction study at 295 and 20 K. *Am. Mineral.*, **96**, 34-41.

Fischer C., Arvidson R.S. and Luttge A. (2012) How predictable are dissolution rates of crystalline material? *Geochim. Cosmochim. Acta* **98**, 177-185.

Fortier S.M., Luttge A., Satir M., and Metz P. (1994) Oxygen isotope fractionation between fluorphlogopite and calcite: an experimental investigation of temperature dependence and F-/OH- effects. *Eur. J.Mineral.***6**, 53-65.

Fregola R.A. and Scandale E. (2011) A 94-layer long-period mica polytype: A TEM study. *Am. Mineral.* **96**, 172-178.

Hartman, P., and Perdock, W.G. (1955a) On the relations between structure and morphology of crystals. I. *Acta Crystallogr.* **8**, 49-52.

Hartman, P., and Perdock, W.G. (1955b) On the relations between structure and morphology of crystals. II. *Acta Crystallogr.* **8**, 521-524.

Hartman, P., and Perdock, W.G. (1955c) On the relations between structure and morphology of crystals. III. *Acta Crystallogr.* **8**, 525-529.

Herrero C. P., Gregorkiewitz M., Sanz J., and Serratosa J.M. (1987) ²⁹Si MAS-NMR spectroscopy of mica-type silicates: Observed and predicted distribution of tetrahedral Al-Si. *Phys. Chem. Miner.* **15**, 84-90.

Hodson M.E. (2006) Searching for the perfect surface area normalizing term—a comparison of BET surface area-, geometric surface area- and mass-normalized dissolution rates of anorthite and biotite. *J. Geochem. Explor.* **88**, 288–291.

Hoche T., Habelitz S. and Avramov I. (1999) Crystal morphology engineering in SiO₂-Al₂O₃-MgO-K₂O-Na₂O-F⁻ mica glass-ceramics. *Acta Mater.* **47**, 735-744.

Johnsson P.A., Hochella M.F., Parks. Jr & George A., Blum A.E. and Sposito G (1992) Direct observation of muscovite basal-plane dissolution and secondary phase formation: An XPS, LEED, and SFM study. *Water-Rock interaction*, Kharaka & Maest (eds) Balkema, Rotterdam. ISBN 90 54100753.

Kogure T. and Inoue A. (2005) Stacking defects and long-period polytypes in kaolin minerals from a hydrothermal deposit. *Eur. J. Mineral.* **17**, 465–473.

Kohli, C. S., and Ives, M. B. (1972) Computer Simulations of Crystal Dissolution Morphologies. *J. Cryst. Growth* **16**, 123-30.

Kurganskaya I., Arvidson R.S., Fischer C. and Luttge A. (2012) Does the stepwave model predicts mica dissolution kinetics? *Geochim. Cosmochim. Acta* **97**, 120-130.

Kuwahara, Y., Uehara, S. and Aoki, Y. (1998) Surface microtopography of lath-shaped hydrothermal illite by Tapping Mode and Contact Mode AFM. *Clays Clay Miner.* **46**, 547-582.

Kuwahara Y., Uehara S. and Yoshikazu A. (2001) Atomic Force Microscopy study of hydrothermal illite in Izumiyama Pottery Stone from Arita, Saga Prefecture, Japan. *Clays Clay Miner.* **49**, 301-309.

Kuwahara Y. (2006) In-situ AFM study of smectite dissolution under alkaline conditions at room temperature. *Am. Mineral.* **91**, 1142-1149 .

Kuwahara Y. (2008) In situ observations of muscovite dissolution under alkaline conditions at 25-50°C by AFM with an air/fluid heated system. *Am. Mineral.* **93**, 1028-1033.

Lasaga A. C. and Luttge A. (2001) Variation of crystal dissolution rate based on dissolution stepwave model. *Science* **23**, 2400-2404.

Lasaga A. C. and Lüttge A. (2003) A model for crystal dissolution. *Eur. J. Miner.* **15**, 603-615.

Lasaga A.C. and Luttge A. (2004a) Mineralogical approaches to fundamental crystal dissolution kinetics-Dissolution of an A3B structure. *Eur. Jour.Mineral.* **16**,713-729.

Lasaga A.C. and Luttge A. (2004b) Mineralogical approaches to fundamental crystal dissolution kinetics. *Amer. Mineral.*, **89**, 527-540.

Loewenstein, W. (1954) The distribution of aluminum in the tetrahedra of silicates and aluminates. *Amer. Mineral.*, **39**, 92-95.

Luttge A., Arvidson R. S. and Fischer C. (2013) A stochastic treatment of crystal dissolution kinetics. *Elements* **9** (3), 183-188.

Maurice P.A., McKnight D.M., Leff L., Fulghum J.E. and Gooseff M. (2002) Direct observations of aluminosilicate weathering in the hyporheic zone of an Antarctic Dry Valley stream. *Geochim. Cosmochim. Acta* **66**, 1335-1347.

Meakin P. and Rosso K.M. (2008) Simple kinetic Monte Carlo models for dissolution pitting induced by crystal defects. *J. Chem. Phys.* **129**, 204106.

Morrow C.P., Nangia S., and Garrison B.J. (2009) Ab Initio Investigation of Dissolution Mechanisms in Aluminosilicate Minerals. *J. Phys. Chem. A* **113**, 1343-1352.

Nagahara L. A., Hashimoto K., Fujishima A., Snowden-Ifft D., and Price P. B. (1994) Mica etch pits as a height calibration source for atomic force microscopy. *J. Vac. Sci. Technol. B* **12**, No. 3, May/June 1994, 1694 – 1697.

Nangia S. and Garrison B.J (2008) Reaction rates and dissolution mechanisms of quartz as a function of pH. *J. Phys. Chem. A* **112**, 2027-2033.

Nespolo M. (2001) Perturbative theory of mica polytypism. Role of the M2 layer in the formation of inhomogeneous polytypes. *Clays Clay Miner.* **49**, 1-23.

Pandey D., Baronnet A. and Krishna P. (1982) Influence of stacking faults on the spiral growth of polytype structures in mica. *Phys. Chem. Minerals* **8**, 268-278.

Patel A. R. and Tolansky S. (1957) The Etching of crystal cleavages. I. Mica. *Proc. Royal Soc. London. A, Math. Phys. Sci.* **243**, 33-40.

Patel A.R. and Ramanathan S. (1962) Etching of mica cleavages. *Acta Crystallogr.* **15**, 860.

Pelmenschikov A. G., Paukshtis E. A., Edisherashvili M. O., and Zhidomirov G. M. (1992) On the Loewenstein Rule and Mechanism of Zeolite Dealumination, *J. Phys. Chem.* **96**, 7051-7055.

Pelmenschikov A., Strandh H., Pettersson L.G.M., and Leszczynski J. (2000) Lattice Resistance to Hydrolysis of Si–O–Si Bonds of Silicate Minerals: Ab Initio Calculations of a Single Water Attack onto the (001) and (111) β -Cristobalite Surfaces, *J. Phys. Chem. B* **104**, 5779-5783.

Rothbauer (1971) Untersuchung eines 2M(1)-muscovits mit Neutronenstrahlen, *Neutronenstrahlen: Neues Jahrb. Mineral. Monatsh* ,143-154.

Rufe E., Hochella M. (1999) Quantitative assessment of reactive surface area of phlogopite during acid dissolution. *Science* **285**, 874 – 876.

Sainz-Diaz C.I., Palin E.J., Dove M.T., and Hernandez-Laguna A. (2003) Monte Carlo Simulations of Ordering of Al,Fe, and Mg cations in the octahedral sheet of smectites and illites. *Am. Mineral.* **88**, 1033-1045.

Shao H., Ray J.R. and Jun Y.-S. (2010) Dissolution and precipitation of clay minerals under geologic CO₂ sequestration conditions: CO₂-brine-phlogopite interactions. *Environ. Sci. Technol.* **44**(15), 5999-6005.

Shao H., Ray J.R. and Jun Y.-S. (2011) Effects of salinity and the extent of water on supercritical CO₂-induced phlogopite dissolution and secondary mineral formation. *Environ. Sci. Technol.* **45**, 1737-1743.

Snowden-Ifft D., Price P. B., Nagahara L. A., and Fujishima A. (1993) Atomic-Force-Microscopic Observations of Dissolution of Mica at Sites Penetrated by keV/nucleon Ions. *Phys. Rev. Lett.* **70**, 2348.

Stübner K., Jonckheere R., and Ratschbacher L. (2008) Revelation of nuclear tracks and dislocations: A Monte Carlo simulation of mineral etching. *Geochim. Cosmochim. Acta*, **72**, 3184–3199.

Sun B.N. and Baronnet A. (1989) Hydrothermal growth of OH-phlogopite single crystals. I. Undoped growth medium. *J. Cryst. Growth* **96**, 265-276.

Sunagawa I. and Koshino Y. (1975) Growth spirals on kaolin group minerals. *Am. Mineral.* **60**, 407-412.

Turpault M.-P. and Trotignon L. (1994) The dissolution of biotite single crystals in dilute HNO₃ at 24°C: Evidence of an anisotropic corrosion process of micas in acidic solutions. *Geochim. Cosmochim. Acta* **58**, 2761-2775.

Wehrli B. (1989) Monte Carlo Simulations of Surface Morphologies during Mineral Dissolution. *J. Colloid Interface Sci.* **132**, No. 1, 230-242.

White G.H. and Zelazny L.W. (1988) Analysis and implications of the edge structure of dioctahedral phyllosilicates. *Clays Clay Miner.* **36**, No.2, 141-146.

Zhang L. and Luttge A. (2008) Aluminosilicate dissolution kinetics: A general Stochastic model. *J. Phys. Chem. B* **112(6)**, 1736-1742.

Zhang L. and Luttge A. (2009a) A general kinetic model of plagioclase dissolution. *Geochim. Cosmochim. Acta* **73**, 2832-2849.

Zhang L. and Luttge A. (2009b) Morphological evolution of dissolving feldspar particles with anisotropic surface kinetics and implications for dissolution rate normali-

zation and grain size dependence: A kinetic modeling study. *Geochim. Cosmochim. Acta* **73**, 6757-6770.

Kinetic Monte Carlo simulations of silicate dissolution: model complexity and parameterization

Inna Kurganskaya¹ and Andreas Luttge¹⁻⁴

¹Department of Earth Science, Rice University, 6100 Main Street, Houston, TX, 77005

²Department of Chemistry, Rice University, 6100 Main Street, Houston, TX, 77005

³University of Bremen, MARUM and FB5, PO Box 330 440, 28334 Bremen, Germany

⁴Department of Geology, Babes-Bolyai University, Mihail Kogalniceanu St., Cluj-Napoca, Romania 3400

Prepared for submission to ACS Journal of Physical Chemistry

4.1. Abstract

The overall dissolution of silicate minerals is controlled by multiple surface reaction mechanisms, reflecting the complex structure of the surface at both molecular- and micron-scale levels. This complexity results in a large number of possible local atomic configurations influencing site reactivity, and thus a corresponding variability in surface reactivity. The aim of this study is to elucidate the net kinetic effect of multiple reactions taking place at the silicate-water interface using Kinetic Monte Carlo (KMC) simulations. However, achieving the proper balance for the number of model parameters required to adequately describe a system's evolution versus the size of the system can be difficult. We approach this problem through the development of a sequence of computer models that consider details influencing surface site reactivity. The capabilities of these models is tested by simulating the dissolution of (001), (100), and (101) quartz faces. Quartz is used as a representative mineral for silicate structures because of its simple chemical composition, the availability of *ab initio* calculations, and its widespread distribution in the Earth's crust and surface. The results show how the ability of each model to correctly predict or reproduce experimentally-observed dissolution behavior of these surfaces depends on model complexity, initial surface structure, and model parameterization. The successful analysis of mechanistic relationships between input parameters and simulation results demonstrates the power of KMC methods in evaluating mineral dissolution kinetics and identifying critical dissolution controls.

4.2. Introduction

Silicate minerals are of great importance for both geological and technical systems. Silicate materials are widely used for industrial purposes as building materials, insulators, chemical catalysts, and are important components of glass, porcelain and ceramics. The structure and reactivity of silicate surfaces may control such important processes, such as cement hydration and kinetics of catalyzed reactions. Nano-composite manufacturing also requires knowledge of silicate reactive properties.

Silicates constitute the most abundant group of minerals in the Earth's crust. Dissolution and precipitation of silicate minerals plays a key role in many geochemical processes taking place on the Earth's surface as well as in the deep crust. Some examples of ubiquitous geochemical processes include weathering, soil and sediment formation, metasomatic and hydrothermal rock alteration, leaching of metals from host rocks and re-deposition as ore bodies, development of pore space in sedimentary basins, and many others. Gaining a better understanding of dissolution mechanisms is necessary for the prediction and control of the fate of these materials in natural and man-made systems. In order to apply quantitative models of natural processes at various scales, correct values for dissolution rates are essential.

It is therefore crucial to understand reaction mechanisms at a variety of scales and develop the ability to predict reaction rates under specific conditions through quantitative modeling of the dissolution process. A fundamental problem in this attempt is how to resolve the relationship between dissolution rates observed

at the microscopic level to those observed at larger, macroscopic scales. Part of the problem is the so-called *intrinsic* rate variance caused by the complexity of the surface structure and its resulting heterogeneous reactivity (Luttge et al., 2013). Fischer et al. (2012) and Luttge et al. (2013) have suggested the use of microscopically measured rate spectra that quantify this heterogeneity and show its relationship to spatial variations in surface roughness. Although it is clear that different reaction mechanisms may operate simultaneously over the mineral surface, the cause for the overall rate variance is not understood in any real detail. A critical problem is that the mechanistic controls governing dissolution cannot always be distinguished from other kinetically relevant factors. For instance, changes in solution composition may lead both to changes in molecular exchange rates at reactive sites and to changes in site distribution and density. It is difficult to observe these microscopic surface processes experimentally, and thus we typically cannot predict the total flux of dissolved material from the surface. Therefore recognition of the factors that control the local and overall reactivity of the mineral surface is of critical importance in understanding reaction kinetics.

In many cases, the overall dissolution kinetics cannot be deduced from reactions involving a limited number of surface complexes (Oelkers et al., 2008). Instead, a significant variety of competing processes may operate at various crystallographic sites at any given time. Thus the mineral surface can be viewed as a dynamic set of different energetic sites, which can be organized into reactive groups on the basis of rate. This kinetic representation of the surface is exploited in Kinetic Monte Carlo (KMC) simulations of crystal dissolution. These simulations can show how the reac-

tive system propagates in time from one surface configuration to another, and reveal the factors that control surface morphology and reactive site distribution. For example, Wehrli (1989) demonstrated that bond breaking energy influences overall surface roughness and reactive site populations. Kohli and Ives (1972) showed how quantitative relationships between dissolution probabilities of various surface sites on Kossel crystals may influence etch pit shape. Zhang and Lutge (2009) studied the shape of dissolving feldspar grains as a function of environmental conditions. Thus important information about surface reactivity as a function of structural and environmental controls observed at the microscopic level can be derived from KMC simulations.

An important problem of the KMC approach is the correct determination of the set of processes that control the evolution of the surface. Ideally, a correct KMC simulation should be based on knowledge of the system's potential energy surface (PES) for the calculation of all possible transitions (Voter, 2007). However, if the model system is large and complex that calculation may be not feasible, and the number of reactions of interest must be reduced in such cases. This reduction requires the identification of the most significant factors defining site reactivity. Electronic structure calculations (DFT and *ab initio*) and Molecular Dynamics (MD) simulations can help to solve this problem for select sites on the crystal surface (Xiao and Lasaga, 1994;1996; Wang et al., 2006; Wang et al., 2009; Morrow et al., 2009; Kubicki et al., 2012). Reactivity controls thus recognized can then be implemented in the simulation code. However, this problem is related to that of rate calculation for each "site type". Most of the KMC algorithms scale one activation energy parame-

ter to the number of existing bonds to be hydrolyzed¹⁵⁻¹⁹, while others employ rate parameters calculated from MD (Piana et al., 2005) or DFT (Dkhissi et al., 2008) techniques for specific sites. The first approach overlooks eventually some important controls, e.g., the long-range forces and structure of surface water. The second approach also requires an accurate site classification scheme. Piana and Gale (2006) calculated reaction rates for the sites differentiated by the numbers of first order neighbors. They noted, however, that the rates they obtained varied substantially for the same site-type. As a result they concluded that long-order neighbors must be also considered in surface site differentiation.

In some case the problem of site classification and rate calculation can be overcome by using ad hoc techniques. For example, Nangia and Garrison (2009) offered an alternative KMC algorithm using reactive potentials to calculate probabilities of the surface configuration transitions and simulate quartz nano-grain dissolution. This detailed approach provides accurate results at nanometer scales. However, experimentally observed rate variance involves much bigger areas, i.e., at least several hundreds of microns in lateral extent (Kurganskaya et al., 2012). Such a large size range would be difficult to model explicitly, although surfaces of several square microns containing up to a million surface sites can be achieved (Meakin and Rosso, 2008).

An educated guess of surface site reactivity controls is often an effective parameterization approach allowing us to balance the system size and the simulation accuracy. In an important step, Kohli and Ives (1972) used the numbers of second

order neighbors to identify key reactive differences among the surface sites of cubic crystals. The influence of long-range order neighbors on dissolution probabilities of surface sites was also established for silicates. Pelmenchikov et al. (2000), Criscenti et al. (2006) showed that bond hydrolysis activation energies depend on bond topologies. Kurganskaya and Luttge (2013) incorporated these findings into a KMC model of phyllosilicate dissolution and showed that consideration of the second-order neighbors is necessary for the recognition of various kink and step sites at mica {hk0} faces. Further differentiation of the sites on silicate surface can be achieved by considering other effects, e.g., hydrogen bonding between surface hydroxyls (Murashov, 2005; Yang and Wang, 2006; Nangia and Garrison, 2010), surface relaxation (de Leew et al., 1999; Du and de Leew, 2006), hydrogen bonding network between surface and water (Yang and Wang, 2006; Kubicki et al., 2012) and other structural factors. An important related problem is the determination of the optimal number of factors required to simulate the dissolution process correctly. Thus we must find a reasonable compromise between the surface size that is required to capture important structural variation and the accuracy of the simulation. These decisions define the complexity level of a given KMC model.

In this paper, we critically evaluate the capability of various parameterized KMC models to predict silicate dissolution. Four KMC models that differ in complexity are used to predict experimentally observed dissolution features and reveal important mechanistic controls of α -quartz. The choice of quartz is advantageous for several reasons. Low-quartz is an important mineral in technical and natural sys-

tems, and a large number of experimental results exist for this phase. Most importantly, reliable DFT and *ab initio* data exist for this phase.

4.3. Kinetic Monte Carlo models

As a first step, we developed four KMC models of quartz dissolution. Each model was characterized by a specific set of criteria used to differentiate various surface sites. We used all four models to simulate the dissolution of three quartz faces, i.e., (001), (100), and (101). We then compared the resulting surface and etch pit morphologies from each model with published experimental data. We used the sensitivity of the model results to the number and values of the input parameters to evaluate several effects such as variations of surface site reactivity and the impact on overall dissolution mechanism.

The KMC algorithm simulates the time evolution of a dissolving surface as a series of discrete reaction events. The surface is represented by a set of reactive quartz lattice sites. At each site various reactions may occur at different rates depending on the site type and the environmental conditions. There are three so-called basic reactions possible (Blum and Lasaga, 1987): (i) dissolution, (ii) precipitation, and (iii) surface diffusion. The models presented here are consistent with dissolution under conditions far-from-equilibrium. This simplification is justified because precipitation and surface diffusion are not critical under these conditions.

Lasaga and Luttge (2004) gave a detailed explanation of a simple but general example of a KMC model for mineral dissolution. We applied the same physical

background for our present study. In particular, we used the “flickering bond” concept of Lasaga and Luttge (2004), i.e., it is assumed that all bonds attaching any molecule to a crystal surface are either in an “on” or “off” state. These states correspond to multiple bond hydrolysis-dehydration reactions. A molecule dissolution event happens only when all relevant bonds are simultaneously in the “off” state. Thus the approximate dissolution probability for a molecule having i bonds with the surface is stated as the product of all bond hydrolysis probabilities:

$$P_i = \prod_{j=1}^i P_j \quad (4-1).$$

The log probability of each surface unit to be dissolved is considered to be the sum of probabilities of the individual bonds to be hydrolyzed:

$$P_i = \exp\left(-\frac{\sum_{j=1}^i \Delta E_{ij}}{kT}\right) \quad (4-2),$$

where ΔE_{ij} is an activation energy of the bond hydrolysis.

The simulation algorithm used in this study was developed on the basis of the effective algorithms described by Meakin and Rosso (2008). We used the so-called “divide-and-conquer” algorithm (or BKL, Bortz et al., 1975) because it is well-suited for simulations of large systems.

4.3.1. The First Coordination Sphere (FCS) Model

The simplest type of a KMC model of crystal dissolution or growth was originally derived for a so-called Kossel crystal (Gilmer, 1980), where the crystal lattice (e.g., cubic, primitive lattice) is represented by blocks. Each of the surface blocks

represents an atom or molecule that has i bonds with nearest neighbors ($i = 1$ to 5).

The dissolution activation energy for this site is then calculated as:

$$\Delta E_i = i \frac{\Delta E}{kT}, \quad (4-3),$$

where ΔE is the activation energy of one bond breaking, T is temperature, and k is the Boltzmann constant. The underlying assumption is that the activation energy of each bond-breaking elementary reaction is equal to the same ΔE value. Wehrli (1989) adopted this model for simulations of oxide (silicate) dissolution, where M sites ($M = \text{Si}/\text{Al}/\text{Mg}/\text{Fe}$ and other cations) serve as reactive centers, and i is the number of M - O - M bonds. The same formula can be applied to quartz, assuming that each Si center on the surface may have from 1 to 4 bonds. The surface sites in this model are differentiated by the number of first nearest Si - O - Si neighbors. However, the second coordination sphere and other long-range effects may also play a crucial role for the reactive site recognition (Kohli and Ives, 1972; Piana and Gale, 2006). Particularly, Kohli and Ives (1972) showed how such recognition influences the capability of the model to produce various etch pit shapes observed in experiments. Below, we discuss several ways to incorporate these effects into the KMC models and classify the models according to their complexity.

4.3.2. The Second Coordination Sphere (SCS) Models

Long-range effects on site reactivity are important for silicates. DFT studies of the $-\text{Si}_m\text{-O}_n-$ cluster reactivity revealed a strong dependence of the ΔE_a value on the cluster size (Pelmenschikov et al., 2000; Criscenti et al., 2006). These results

were summarized and discussed by Criscenti et al. (2006), who demonstrated that the bond hydrolysis activation energy is a function of the topology (“connectedness”) of the Si centers. According to the formulation of the Si-centered KMC models (eq. 4-1), evaluation of the influence of bond topology on surface site reactivity requires consideration of at least two $-O-Si-O-Si-O-$ coordination spheres in probability calculations (Fig. 4-1).

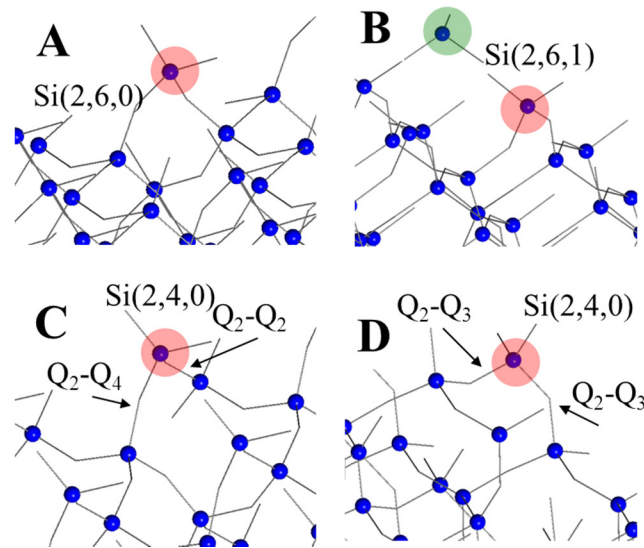


Figure 4-1. Differentiation of the Si (N_1, N_2, N_3) reactive sites (red circles) on the quartz surface used in KMC models. Only Si atoms are shown. N_1 is the number of first order Si-O-Si neighbors, N_2 and N_3 are the numbers of second-order “connected” and “disconnected” (green circle) neighbors. **(A)** and **(B)** show the difference between “connected” and “disconnected” neighbors, **(C)** and **(D)** illustrate two possible bond configurations for a (2,4,0) site. **(A)** (2,6,0) site ; **(B)** (2,6,1) site ; **(C)** Q₂-Q₄;Q₂-Q₂ configuration ; **(D)** Q₂-Q₃;Q₂-Q₃ configuration.

Thus, the presence or absence of the Si2 and Si3 atoms in the O-Si1-O-Si2-O-Si3-O link affects the Si1 site reactivity. Nangia and Garrison (2009) used similar considerations in the development of their KMC algorithm, in terms of the influence of long-range order neighbors. They tested their model with a quartz nanoparticle and concluded that consideration of long-order neighbors do not influence reactive site distribution. We suggest that since that conclusion was made for the very small system size, we must carefully investigate the influence of the second-order neighbors for substantially larger surface sizes.

Another attempt to use a second-coordination sphere for site recognition was made by Ferrando et al. (2012) who developed a Cellular Automata model for quartz etching. The authors used a deterministic simulation procedure, where the dissolution rates for various faces and surface sites were calibrated by macroscopic rates obtained from experiments. The numbers of various second-order neighbors served as parameters for the crystal face recognition. With this approach they successfully produced temporal sequence of etch pits observed in experiments. In this paper we solve another problem: we aim to develop the KMC model that, ideally, would be able to predict surface morphology and dissolution dynamics from the “first-principles”, e.g., from the given reaction set and activation energy values, without using experimental data for model calibration. The proper estimation of the pre-exponential frequency factors for surface reaction rates would also enable calculation of the dissolution rates by using this model.

4.3.2.1. Linear Approximation 1 (SCS-L1) model

In order to incorporate the role of bond topology (Criscenti et al., 2006) introduced above into the KMC model, we differentiated all surface sites based on the numbers of first and second order Si-O-Si links. The dissolution probabilities for each Si(N_1, N_2) site were calculated as the exponential function of the total sum of activation energies required to break all bonds. Ideally, these energies should be calculated for each bond (see section 2.2.3 for further discussion). However, this goal cannot always be achieved. Therefore, the total activation energy (sum of energy terms) should be calculated as a function of the number of nearest neighbors. Kohli and Ives (1972) proposed the simplest (linear) method that we used in this study:

$$\Delta E_{i,j} = i\Delta E_1 + j\Delta E_2 \quad (4-4).$$

This (SCS-L1) model belongs to the class of “linear approximation” models, and the energy sum is calculated as a parametric linear function of the number of contributing neighbors of different types.

4.3.2.2. Linear Approximation 2 (SCS-L2) Model

Since quartz has 3-dimensional framework structure, all crystal faces can be formed by only cutting the crystal lattice parallel to crystallographic planes and rupturing of Si-O-Si bonds. As a result, surface hydroxyls are always present on quartz surface (Du and de Leew, 2006). These hydroxyls may form hydrogen and O..H bonds with each other and water molecules, thus introducing additional controls on

surface site reactivity. Ruptured Si-O-Si bonds at “perfect” (100), (001) and (101) quartz faces cause a change of coordination state for the neighboring atoms. The Si atoms in the first surface layer lose their first-order neighbors, and the atoms in the second layer lose their second-order neighbors. At the same time, some atoms in the first layer lose the direct O-Si₁-O-Si₂-O-Si₃-O connection with their second-order neighbors, gaining instead the O-Si₁-OH..HO-Si₃-O connection. Therefore, in order to differentiate the two different types of connections, we divided second-order neighbors into two types based on their topology. They are thus either “connected” to or “disconnected” from a site of interest (Figs. 4-1A; 4-1B). The state of “connectivity” is purely topological, and is not related to the bond breaking or forming reactions. The “disconnected” second order neighbor is formed if the central Si₂ atom is removed from a fully connected link of the type -O-Si₁-O-Si₂-O-Si₃-O-. In this case, Si₁ becomes a second order disconnected neighbor for Si₃ and *vice versa*. It is important to note that a change in the connectivity state of a second order neighbor may also change the reactivity of a given surface site. This leads to a more advanced model, i.e., the SCS-L2 model. Here, we describe the topology of each surface site by using (N₁,N₂,N₃) notation: N₁ is the number of first order neighbors, N₂ is the number of “connected”, and N₃ is number of “disconnected” second order neighbors. We calculate the total amount of energy necessary for the hydrolysis of all bonds by using equation:

$$\Delta E = n_1 \Delta E_1 + n_{2l} \Delta E_{2l} + n_{2g} \Delta E_{2g} \quad (4-5),$$

where n_1 , n_{2l} and n_{2g} are the numbers of the first order, second order connected and disconnected neighbors respectively, ΔE_1 , ΔE_{2l} , and ΔE_{2g} , are the energetic contributions of each of these neighbors to the total activation energy.

4.3.2.3. The “Direct” Parameterization (SCS-D) Model

Both models described above assume linear approximations of the actual dissolution probabilities for the different surface sites. We can improve these approximations substantially if we use the calculated activation barriers for the bond hydrolysis directly in the probability calculations. This leads to the following equation:

$$\Delta E_{i,j,k} = \frac{\sum_{m=1}^{N_{conf}} \sum_{n=1}^i \frac{\Delta E(Q_i-Q_j n)}{kT}}{N_{config}} + \frac{n_k \Delta E_{2g}}{kT} \quad (4-6),$$

where Q_i-Q_j designates a bond with i and j Si-O-Si links at each Si center that forms a bond²². We then averaged the energy sums over all possible bond configurations and applied it to each (N_1, N_2, X) site type (examples of the two different configurations are shown in Figs. 4-1C and 4-1D). *Ab initio* or MD data relevant to the quantitative influence of the disconnected second-order neighbors are not available at this moment, and thus we use the ΔE_{2g} term representing the effects of the “disconnected” second order neighbors.

4.3.2.4. Model parameters

In our previous work, dedicated to mica dissolution, we optimized parameter values until the experimentally observed etch pit structures were reproduced by the

model (Kurganskaya et al., 2013). In contrast, here we attempt to test the ability of the KMC approach to correctly predict dissolution surface morphologies using parameters derived from the theoretical electronic structure calculations.

In order to parameterize the SCS-D model, we used the activation energy list compiled by Criscenti et al. (2006). To this list, we added interpolated values for the missing bond types (see Table 4-1). We chose the values for the energy parameters in the other three models from a range similar to that of the values of *ab initio* derived energies (Xiao and Lasaga, 1994; Pelmenchikov et al., 2000; Criscenti et al., 2006). In addition, we performed a few simulations with lower activation energy values in order to test the possible influence of catalyzing conditions (e.g., low pH, presence of alkali ions, etc.). All values used in the calculations are presented in Table 1.

Table 4-1. Activation energies of bond hydrolysis and other energetic parameters used in the KMC models, in [kJ/mole].

Bond type	Activation energy	Energetic parameter	Value	
			“pure water”	“catalyzing conditions”
Q1-Q1	71*	$\Delta E(\text{FCS})$	100	30
Q1-Q2	75'	$\Delta E_1(\text{SCS-L1})$	70	20
Q1-Q3	112**	$\Delta E_2(\text{SCS-L1})$	10	5
Q1-Q4	90'	$\Delta E_{21}(\text{SCS-L2})$	10	4
Q2-Q2	78'	$\Delta E_{2g(1)}(\text{SCS-L2})$	0	0
Q2-Q3	80'	$\Delta E_{2g(2)}(\text{SCS-L2})$	5	1
Q2-Q4	92*	$\Delta E_{2g(3)}(\text{SCS-L2})$	10	2
Q3-Q3	162***			
Q3-Q4	138*			
Q4-Q4	205*			

-(*) Pelmeshnikov et al., 2000; -(**) Criscenti et al., 2006; -(***) Wallace et al., 2010, all *-*** values are calculated by using DFT calculations with the B3LYP functional, 6-31G(d) basis set; (')-activation energies calculated by interpolation of the published values.

4.3.3. Surface stabilization and relaxation effects

All models presented above consider only local structural factors influencing site reactivity. However, periodicity of the crystal lattice and surficial hydrogen bond network introduce some additional effects that must be considered here. The most spectacular mineral-water interface effects were found for the (001) face, which was shown to be stabilized by the following effects: (i) hydrogen bonding networks between surface hydroxyls (intra-surface hydrogen bonding, Murashov, 2005; Yang and Wang, 2006); (ii) bonding between surface hydroxyls and water

(Yang and Wang, 2006); and (iii) structuring of the water film that is adsorbed on the surface, i.e., the so-called “water tessellation” effect (Yang et al., 2004). In addition, the (100) face, i.e., the prism face of quartz is further stabilized by hydrogen bond formation, while the (101) face mainly lacks this effect (Murashov, 2005). However, the presence of alkali (Na^+) ions may increase the reactivity of this face by changing the structure of the water layer and inducing the formation of H-bonding between the adsorbed water layer and surface hydroxyls (Kubicki et al., 2012). Therefore, the surface-water structure is specific for each face and its environment. This effect can either increase or decrease the reactivity of specific surface sites.

The relative surface energies of the (001), (100), and (101) faces were calculated by Murashov (2005), who proposed two sequences for relative face stability. In the presence of a hydrogen bond network, the stability of faces increases in the following order: (101) < (100) < (001). However, exclusion of the hydrogen bond energy from face energy calculations gave the inverse order, i.e., (001) < (100) < (101).

Nangia and Garrison (2010) investigated the influence of these important effects on the kinetics of β -cristobalite dissolution. They concluded that the face that is made of Q_2 sites can dissolve even slower than a face that is made of Q_3 sites.

Another known factor that stabilizes the surface is the “surface relaxation” effect caused by the reconstruction of subsurface atomic layers. The relaxation effect for quartz is pronounced particularly for the (001) or basal face (de Leew et al., 1999; Rignanesi et al., 2000; Murashov, 2005; Du and de Leew, 2006), where two-

coordinated Q_2 sites composing this face turn into four-coordinated Q_4 sites. However, this surface structure is stable in vacuum, only, while in the presence of water surface Si-O-Si bonds become broken, so Si-OH surface groups are formed and (001) face re-organizes into a Q_2 structure (Du and de Leuw, 2006). Therefore, the influence of the “relaxation effect” on surface reactivity is probably not significant. In our study, we included the “cumulative” surface effects indirectly by assuming that they stabilize terrace sites with respect to the other reactive surface sites. We applied two distinct methods: 1) the “short-order, long-term” stabilization or S1 method that differentiates the terrace sites and applies a weighting coefficient that reduces their probabilities to dissolve; 2) the “long-order, short-term” stabilization or S2 method, in which we completely “froze” the terrace sites of the starting top layer. With this approach we tested the assumption that the laterally extensive and atomically flat initial surface made from terrace sites is relatively more stable with respect to the newly created surface. Thus, the S2 method is developed to test cases where all of the following takes place: (i) terrace sites of the simulated face are more stable than those of the other faces; (ii) terrace stabilization is considered only for the initial surface, and thus, has a short-term duration. The purpose of this approach is to study the dissolution mechanisms and effects of the relative stability of quartz faces (i.e., their terrace sites) derived by Murashov (2005).

4.4. Results and discussion

We used the four model variations described above to simulate the dissolution of pinacoid, prism, and rhombohedral quartz faces. Pre-opened hollow cores

were introduced along the screw dislocation lines intersecting these faces. In many cases, presence of hollow cores result in the formation of kinematic stepwaves and serve as “long-term” sources for them (Lasaga and Luttge, 2001). Lateral motion and annihilation of the stepwaves cause surface-normal retreat, and thus, drives mineral dissolution according to Lasaga and Luttge’s model. Our simulation results indeed show that stepwaves of various geometries can form on all three quartz faces.

Furthermore, we present simulation results for each face and discuss the influence of model complexity on the observed surface structures. In addition, we discuss the geometry of the stepwaves and the corresponding dissolution mechanisms.

4.4.1. Pinacoid (001) face

Our KMC simulations demonstrate that the surface morphology of the dissolving (001) face is very sensitive to model complexity. Fig. 4-2 shows various the surface topographies that developed in “pure water”. We will discuss these results further, below.

4.4.1.1. Surface morphologies

The FCS model (eq. 4-3) produces a rough surface with a random peak-and-valley topography (Fig. 4-2A). In contrast, the other models produce crystallographically-controlled dissolution patterns. Thus, the use of the SCS-L1 model results in the formation of shallow hexagonal etch pits (e.g., Fig. 4-2B).

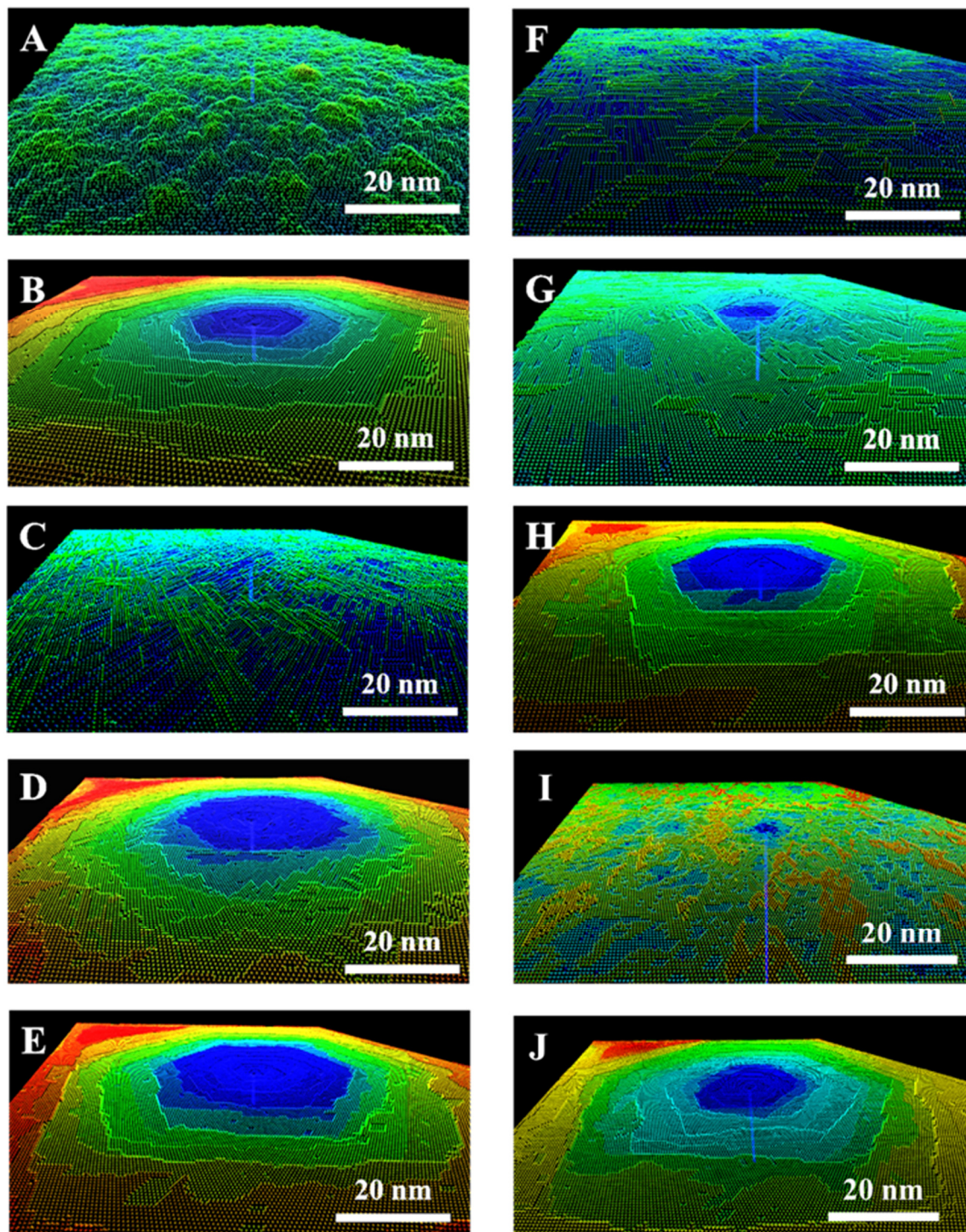


Figure 4-2. KMC simulation of a dissolving (001) quartz face in pure water, neutral pH, T = 25°C (modeling parameters are shown in Table 4-1, a single screw dislocation intersects the surface at the center). Results from: **(A)** the FCS model;

(B) the SCS-L1 model; **(C)** the SCS-L2 model ($\Delta E_{2g} = 0$ kT), and **(D)** the SCS-L2 model ($\Delta E_{2g} = 2$ kT); **(E)** the SCS-L2 model ($\Delta E_{2g} = 4$ kT); **(F)** the SCS-D model ($\Delta E_{2g} = 0$ kT); **(G)** the SCS-D model ($\Delta E_{2g} = 2$ kT); **(H)** SCS-D model ($\Delta E_{2g} = 4$ kT); in case of **I** and **J** the surface is stabilized by adding weight coefficients to the terrace sites (S1 method); **(I)** SCS-D ($\Delta E_{2g} = 0$ kT; S1); **(J)** SCS-D ($\Delta E_{2g} = 2$ kT; S1) model.

The SCS-L2 and SCS-D models produce a variety of different surface morphologies that strictly depend on the ΔE_{2g} values used in the simulations. For example, if we set ΔE_{2g} to 0, the dissolving surfaces become molecular chains oriented along the three crystallographic directions, i.e., [100], [010], and [110] (Figs. 4-2C and 4-2F). The chains periodically change their orientation following the corresponding rotation of the (001) plane around the *c* axis. In contrast, at $\Delta E_{2g} = 2$ kT circular pits with rough edges are formed (Fig. 4-2D). A further increase to values of $\Delta E_{2g} > 4$ kT higher results in straightening of the steps and a change of etch pit morphology from circular to hexagonal shapes (e.g., Figs. 4-2B, 4-2E, 4-2H, 4-2J). The formation of etch pits and steps always results from the anisotropy of the dissolution rate for specific surface sites. Since the (001) face is composed entirely of Q_2 sites, the use of second order neighbors introduces energetic differences between the terrace, ledge, and kink sites on this plane. However, the differentiation of “connected” and “disconnected” second-order neighbors and the reduction of the influence of the latter to zero may result in the complete change of the surface structure, from one characterized by stepwaves emanating from etch pits, to one dominated by straight -O-Si-O- chains. In this case, the stepped topography of the surface is not supported. We suggest that regardless of the absence of the direct Si-O-Si link, the

“disconnected” second-order neighbors may substantially stabilize the surface steps with respect to their kink sites, probably via formation of hydrogen bonds. Consideration of the second-order neighbors in probability calculations can be vital for step stabilization, in case if step and kink site cannot be differentiated using only first coordination sphere (Kurganskaya and Lutge, 2013). The presence of the steps supports the stepwave mechanism (Lasaga and Lutge, 2001) that drives the dissolution of this face in cases shown in Figs. 4-2B, 4-2D, 4-2H, and 4-2J.

4.4.1.2. Etch pit structure

The variety of the observed surface structures presented above ultimately demonstrates that the (001) face may dissolve via three different mechanisms: random molecular removal, dissolution of oriented $-\text{Si-O-Si-O-Si}-$ chains and the stepwave movement. If the latter controls dissolution, the etch pit geometry defined by model parameters also defines more detailed dissolution controls, such as crystallographic direction of steps, step structure and relative step velocities. Experimentally, there were two etch pit shapes observed on basal quartz faces. Chuvyrov and Mazitov (2008) etched the basal face with KOH and documented hexagonal pits formed by steps parallel to the (001) plane. Wegner and Christie (1983) observed triangular shapes on the basal face after etching it with ammonium bifluoride. However, we obtained only hexagonal and circular shapes for the multilayer pits using both “pure water” and “low energy” data sets of activation energies (see Table 4-1). We suggest that the emergence of triangular pit morphologies may reflect be some

additional factors responsible that our relatively simple model does not as yet incorporate.

An important observation is the complex structure of the etch pits in the (001) face. The hexagonal morphology of these pits results from stacking sequences of monolayer pits having a parallelogram shape. The orientation of these parallelograms periodically changes from one (001) atomic layer to the next one. Thus, the formation of the hexagonal shape is the result of the superposition of monolayer parallelogram-shaped pits rotated by 120° with respect to each other. The characteristic step interlacing, or *zigzag* pattern is formed at the corners of the hexagons (see Figs. 4-2B, 4-2H, 4-2J). The step interlacing is a characteristic feature of the pits formed on faces perpendicular to the symmetry rotation axis, the same effect is known for micas (Kuwahara et al., 1998; Aldushin et al., 2006; Kurganskaya et al., 2012).

4.4.1.3. Surface stabilization effects: etch pits and hillocks

The inclusion of the surface stabilization effect (S1 method, +4 kT units to each “terrace” site) changes the surface structure slightly. At $\Delta E_{2g} = 0$ kT monolayer dissolution islands and pits are formed instead of molecular chains (Fig. 4-2I). An increase of ΔE_{2g} to 2 kT causes formation of stable steps and hexagonal pits (Fig. 4-2J). This observation shows that etch pits and steps form at the lower values of ΔE_{2g} if the terrace sites are stabilized. We conclude that both terrace stabilization and hydrogen bonding effects are likely to influence both step structure and etch pit formation.

Fig. 4-3 illustrates a different dissolution scenario. In this case the terrace sites of the initial layer are “frozen” (or excluded from the “reactive surface” lists according to the S2 stabilization method), while all the other surface sites and faces are free to evolve. Polyhedral pits made of rhombohedral faces are formed at the onset of the dissolution process.

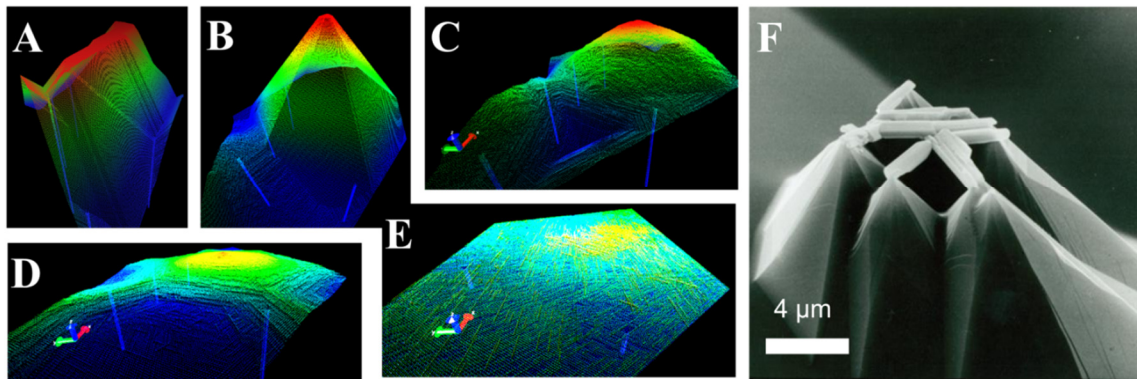


Figure 4-3. **A-E**: KMC simulations of the formation and dissolution of quartz hillocks starting from a “frozen” (stabilized) (001) face of quartz. The SCS-L2 ($\Delta E_{2g} = 0$ kT) model is used for this illustration, 5 screw dislocations parallel to the c^* axis intersect the starting surface. A $(\text{SiO}_4)^{4-}$ -group is removed from the surface during each iteration. **(A)** $8 \cdot 10^6$ iterations; **(B)** $16 \cdot 10^6$ iterations; **(C)** $24 \cdot 10^6$ iterations; **(D)** $32 \cdot 10^6$ iterations; **(E)** $40 \cdot 10^6$ iterations. **(F)*** Hillocks formed on a dissolving quartz surface observed in experiments by Neumann and Luttge (1995).

*-Adapted from the original publication (Neumann and Luttge, 1995, see references) and used with the permission of author (Luttge A.).

Their subsequent coalescence results in the formation of a ridge feature, where the remains of an initial frozen (001) face appear as a long narrow plateau, the rhombohedral faces form the slopes and the valleys shape is controlled by hollow core locations (Fig. 4-3A). Further dissolution produces pyramidal quartz hillocks (Fig. 4-3B). These hillocks are positive surface features, in contrast to negative ones such as etch pits. In this simulation, the polyhedral hillocks are unstable and quickly dissolve at the vertices and edges forming the other rough, rounded hillocks. At the same time, deep triangular pits can form between the hillocks (Fig. 4-3C). Later, the hillocks retreat while the triangular pits change their shape to hexagonal (Fig. 4-3D). Finally, the surface structure returns to the one of the previous structures (Fig. 4-2) defined by the model type and model parameter values (Fig. 4-2C for this case). This dissolution scenario was experimentally observed by Suzuki et al. (2009), who documented the same “ridge-and-valley” surface structure as indicated in Fig. 4-3A on a lapped (001) face. Hillocks of the same or at least very similar morphology as shown in Fig. 4-3B were also observed in high pressure, high temperature experiments conducted by Neumann and Lutge (1995) (Fig. 4-3E). In the latter case, the diopside crystals grew often on the tips of the hillocks. Thus, the authors hypothesized that these crystals would play a stabilizing role. Although all the factors causing hillock appearance are not always known, they clearly can form solely due to different dissolution rates on different faces (Sangwal, 1987) (here basal and rhombohedral). Our KMC results also demonstrate that pyramidal hillocks can form as a result of the coalescence of pits that are made up predominantly by rhombohedral faces, which evolve if the starting basal face dissolves much slower. Another important prerequi-

site for the formation of such features is the enhanced stability of the starting surface that allows the faces to initially evolve. However, in our case there was not such a factor that would have supported the stability of the hillocks. They thus retreated immediately after formation. Nijdam et al. (2001) faced a similar problem when explaining etch hillock formation and stability on the (100) face of silicon. They supposed that adhering semipermeable nm-sized particles caused hillock formation – a similar mechanism to that postulated by Lutge and Neumann (1995). They also achieved similar results from their Monte Carlo simulations: that means the hillocks formed when they applied a semipermeable mask over a small part of the initial surface. In the absence of the mask, the (100) silicon face retreated faster than the other faces and hillocks did not form. Our simulation results suggest that the enhanced stability of the (001) face (Murashov, 2005) can itself cause spontaneous hillock formation. However, the additional lasting stabilization of hillock tips and edges after its formation is required for these features to be preserved during the dissolution process. As mentioned before, the hillock stabilization may be also induced by precipitating crystals that protect the hillock tip from dissolution (Neumann and Lutge, 1995), or by adhering particles as suggested by Nijdam *et al.* (2001).

4.4.2. Rhombohedral (101) face

4.4.2.1. Surface structure

All our models show that the dissolution of the (101) face proceeds through the formation of characteristic isosceles triangular etch pits (Fig. 4-4). At the early stages of surface morphology development the dissolution is controlled by the

movement of triangular stepwaves parallel to the (101) plane (Fig. 4-4A1). At later stages deep triangular pits with steep walls develop (Fig. 4-4B1). The overall pit profile is usually anisotropic, i.e. the pit walls are quite steep, while the bottom is stepped and elongated along the [101] direction (Fig. 4-4B2). When several pits interact with each other, a complex geometric pattern with super-steps can be formed (Fig. 4-4C1). Their subsequent coalescence results in the formation of larger triangular pits (Fig. 4-4C2) with a complex wall structure. A stepped pentagonal pit also forms at the junction between the hollow core and the triangular pit (Fig. 4-4B1).

Similar pit shapes were observed on (101) faces during quartz dissolution and etching experiments. Yanina et al. (2006) documented pseudo-triangular fan-shaped pits formed on (101) face after etching with KOH. These pits had the same characteristic anisotropic profile that we obtained for our KMC simulated pits (e.g., Fig. 4-6B2). However, the pentagonal pits were not reported in this study. At the same time, these pits of semi-pyramidal appearance were observed on rhombohedral faces etched by KOH (Patel et al., 1965) (Fig. 4-4E), where, however, the original triangular pits did not appear. Also, the pits that have a sharp triangular shape were documented on the surface of naturally weathered quartz grains (Brantley et al., 1986).

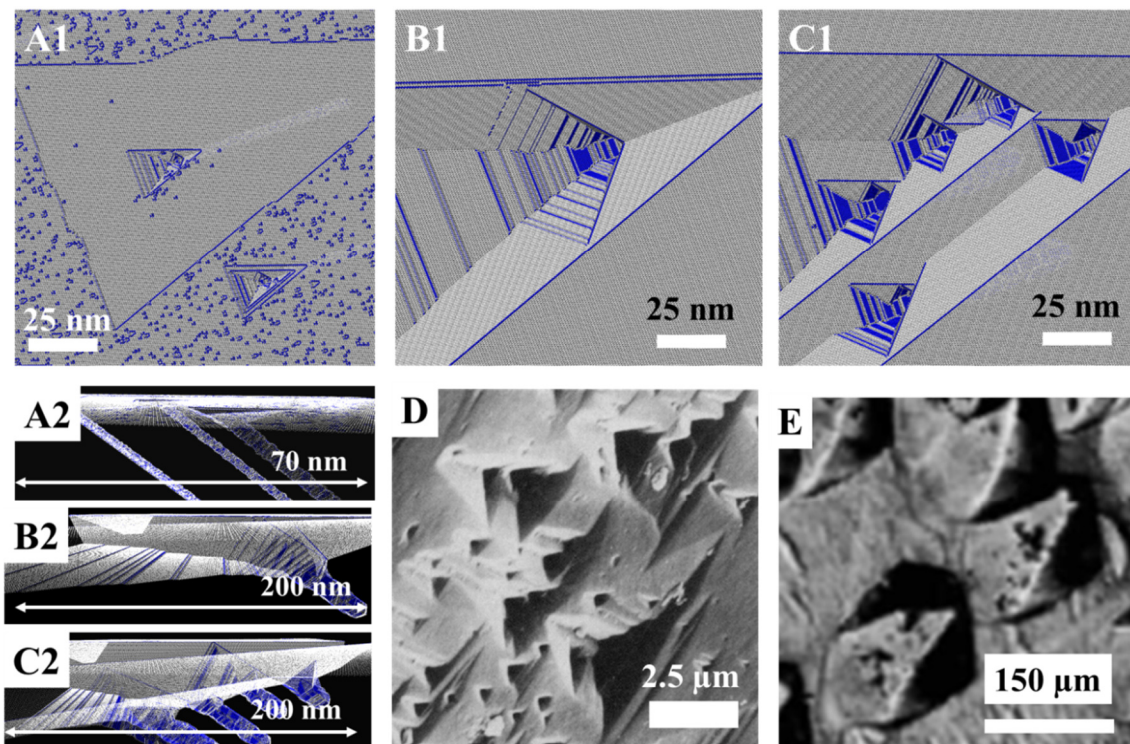


Figure 4-4. **(A)-(C)**: Results of KMC simulations: Etch pits formed on the rhombohedral (101) quartz face in pure water, neutral pH, $T = 25^{\circ}\text{C}$ (energetic parameters are shown in Table 4-1) (blue highlights (3,7) sites), subfigures labeled by “1” present the front views, subfigures labeled by “2” present the side views with hollow cores. **(A)** Surface produced by using the FCS model, 10^6 molecules removed; **(B)** A pentagonal pit developed at the junction between the triangular pit and the hollow core, SCS-D ($\Delta E_{2g} = 0$) model, $2 \cdot 10^6$ molecules removed. **(C)** Polygonal pits formed at the walls of the original triangular pit, SCS-L2 ($\Delta E_{2g} = 0$) model; $12 \cdot 10^6$ molecules removed. **(D)*** Triangular pits observed on the surface of naturally weathered quartz grains (Brantley et al., 1986). **(E)**** Polygonal etch pits observed on rhombohedral quartz surface etched by KOH (Patel et al., 1965).

*Reprinted from *Geochimica et Cosmochimica Acta*, Vol 50/Issue 10, Brantley S.L., Crane S.R., Crerar D.A., Hellmann R. and Stallard R. "Dissolution at dislocation etch pits in quartz", Pages No. 2349-2361 (DOI: 10.1016/0016-7037(86)90087-6) Copyright (1986), permission obtained from Elsevier.

** - This figure is adapted from the original publication, Patel A.R., Bahl O.P. and Vagh A.C. "Etching of rhombohedral cleavages of quartz", *Acta Crystallographica* (1965), Vol. 19, pp. 757-758 (<http://dx.doi.org/10.1107/S0365110X65004322>). Used with copyright permission from IUCr Journals.

We conclude that the two types of evolutionary related pits that we saw in the simulations (triangular and pentagonal) have been observed as independent formations in laboratory investigations. We suggest that this effect may be related to scale-size difference between the simulated and experimentally observed systems. The pentagonal pit is quite small in comparison to the triangular one, and thus may be undetected. In contrast, pentagonal pits may appear as structurally independent features at the later stages of surface development (Fig. 4-4C1).

4.4.2.2. Hollow cores and etch tubes

Hollow cores exhibiting a polygonal geometry is another remarkable feature produced in our KMC simulations of (101) face dissolution. The walls of the hollow cores are decorated by polygonal pits forming specific “ribbon” pattern (Figs. 4-4A2; 4-4B2;4-4C2). The same structure was observed experimentally, too (Nielsen and Foster, 1960; Iwasaki, 1977). However, its formation was attributed to a specific defect type (Nielsen and Foster, 1960) or orientation within the lattice (Iwasaki, 1977). Here, we can show that such “ribbons” are also formed as sequences of steps that are moving along the walls of the hollow cores.

4.4.2.3. Dissolution mechanism: 2D and 3D stepwave movement

While all four models produced the same surface structure, the FCS model's use results in formation of a distinct feature: large number of small monolayer pits that randomly nucleated across the entire surface (Fig. 4-4A1). We relate the ap-

pearance of this feature to the topological identity of “terrace” and “step” sites for the FCS model at the (001) face.

The relative densities of these monolayer pits can be used to determine the relative ages of the surface layers. Indeed, the difference in monolayer pit density for areas inside and outside the triangular kinematic stepwave indicates that the stepwave velocity is much greater than the frequency of the stepwave formation (Fig. 4-4A). As a result, the (101) face retreats through a layer-by-layer mechanism. Most of the time, the observable surface area is intact and once a stepwave has formed the entire layer dissolves during a relatively short time period. The movement of an entire triangular stepwave is driven by the step parallel to the triangle’s base ([010] direction). Steps moving in this direction often form stairs (Figs. 4-4B1; 4-4B2) and generate the steep slope of the pit. The other two sides of the pit create steep walls. The same pattern is also formed on these sides, generating three symmetrical “active” step systems at a single dislocation core. As a result, the pentagonal pit formed at the junction between the hollow core and original triangular pit (Fig. 4-4B1). As we can conclude from this observation, a pentagonal pit develops as a result of the long-term effect of the stepwave movement at the three intersecting rhombohedral planes. The “classic” stepwave model (Lasaga and Luttge, 2001) explains crystal dissolution as movement and coalescence of the 2D stepwaves parallel to a one plane. However, in this case we can conclude that if several stable faces develop on the dissolving surface, the stepwave process may act over all of them. Therefore, a remarkable difference in the dissolution mechanisms between (001) and (101) faces exists. It is defined by the dimensionality of the stepwave propaga-

tion: the stepwaves on (001) face spread within one plane parallel to (001) (2D process), while stepwaves on (101) face travel within several rhombohedral planes (3D process). Thus, (101) face dissolves through the “classic” 2D stepwave mechanism only in the beginning of the process (Fig. 4-4A). At later stages, when the other rhombohedral faces develop, dissolution of the entire surface is controlled by the propagation and coalescence of the stepwaves coming from various faces (Fig. 4-4C1).

4.4.3. Prism (100) face

The prism (100) face of quartz can be formed if we cut crystal parallel to b^* and c^* crystal axis. As a result, we obtain two atomically flat prism faces terminated by the two different types of Si-slices. One is made up of Q_2 sites (α - or Q_2 -termination), another is made of Q_3 sites (β - or Q_3 -termination) (Schlegel et al., 2002). We simulated dissolution of both terminations and noted that the difference in dissolution patterns exists only when surface stabilization is applied. We observed two types of dissolution scenarios at both non-stabilized terminations and a third scenario at Q_2 termination stabilized by S2 method.

4.4.3.1. Dissolution scenario I: striations

Simulations of (100) prism faces in “pure water” (Table 1) showed the same morphology in all four models: long grooves running along the \mathbf{b} axis. The grooves develop from elongated etch pits that formed in the beginning of the dissolution process (Fig. 4-5A). The resulting surface is composed of “stripes” formed by the in-

tersection of $\{10\bar{1}1\}$ and $\{\bar{1}011\}$ rhombohedral planes along the $[010]$ direction. This process creates parallel ridges (Fig. 4-5B) and leads to the formation of striations often observed on dissolving quartz surfaces (Luttge, 1995) (Fig. 4-5E). Several authors have associated these features with crystal dissolution (Luttge, 1995) or growth (Ostapenko and Mitsyuk, 2006) of prism faces.

This surface topography can be sustained as long as screw dislocations intersect the (100) face. At the mature stage of the surface development, the same screw dislocations that produced the grooves serve as the centers of new V-shaped pits (Fig. 4-5B and 4-5C). These pits, in fact, are coupled triangular pits (Fig. 4-4) that develop on neighboring rhombohedral faces. Such V-shaped features were documented on lapped quartz prism face (Suzuki et al., 2009). They are also commonly observed on naturally weathered quartz grains (Schultz and White, 1999). A tetragonal hollow core is another characteristic feature of this face (Figs. 4-5A2; 4-5B2; 4-5C2). The walls of the cores have distinct polygonal structure governed by etch pit formation (Fig. 4-5C2).

4.4.3.2. Dissolution scenario II: rectangular stepwaves

Rectangular pits made from two systems of parallel steps are formed at low activation energies or catalyzing conditions (see “Methods” part and Table 1) and values of $\Delta E_{2g} > 4 \text{ kT}$ (Fig. 4-5D1). The cross section of the pits reveals their internal conical shape (Fig. 4-5D2). The steps moving parallel to the c^* axis have terrace-widths of 10 to 20 nm, while steps moving along the b^* axis are bunched.

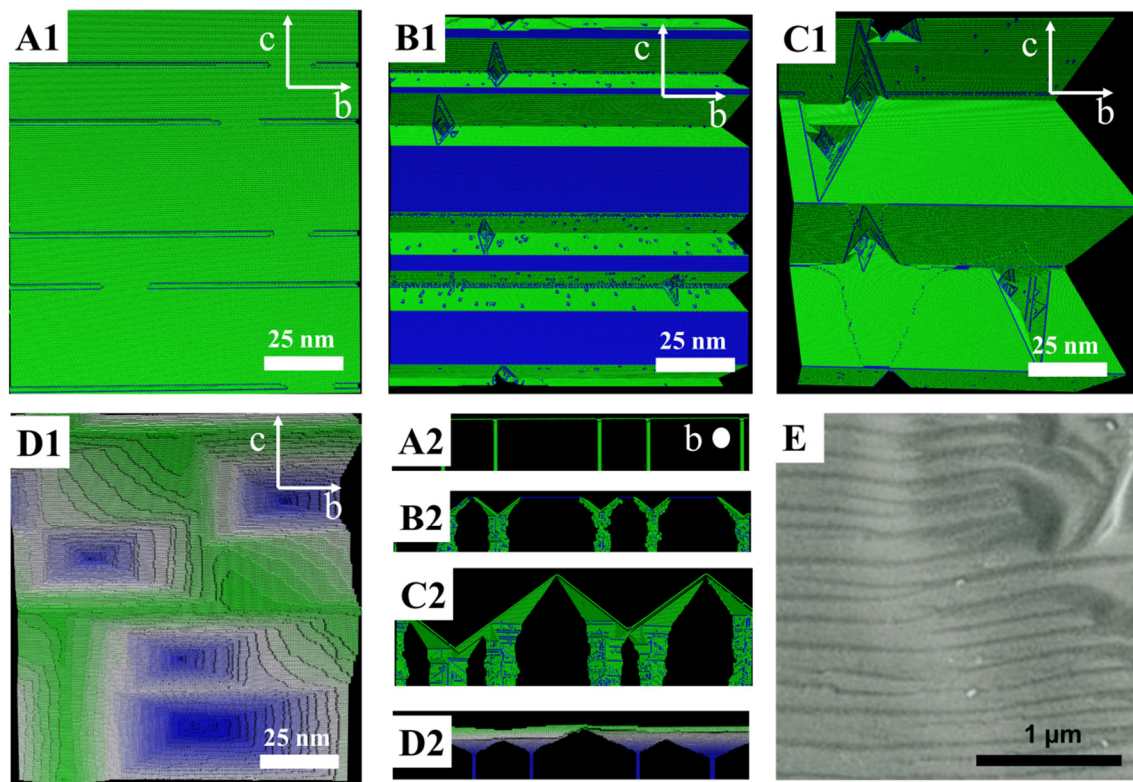


Figure 4-5. (A)-(D): Structures of the dissolving (100) prism face of quartz obtained from KMC simulations (starting from Q_3 termination; pure water, neutral pH, $T=25^\circ\text{C}$, parameters are shown in Table 4-1). Label “1” refers to the front view, label “2” refers to the side view with the etch tubes. (A)-(C)- Surfaces simulated using SCS-D ($\Delta E_{2g} = 0$) model (blue highlights (3,7) sites)), (A) Etch pit opening at the beginning of the simulation (10^4 molecules removed). (B) “Striations” and V-shaped pits appeared at a later stage of the simulation (10^6 molecules removed). (C) The same surface with developed V-shaped pits and rhombohedral faces, $6 \cdot 10^6$ molecules removed. (D) The surface obtained by using SCS-L2 ($\Delta E_{2g} = 4$ kT units) model, with the surface stabilization effect (S2 method) and parameter values $\Delta E_{1-} = 20$ kJ/mol, $\Delta E_{21} = 1$ kJ/mol; $\Delta E_{2g} = 10$ kJ/mol. (E)* Striations formed on the quartz surface dissolved at hydrothermal conditions. The face and direction could not be identified (Luttge, 1995).

*-this figure is adapted from Luttge (1995) with the permission of author (Luttge A.).

The coalescence of the rectangular stepwaves results in the formation of curved circular steps (Fig. 4-5D1). A similar surface structure was reported by Yanina et al. (2006), but they gave another orientation of pits and steps with respect to the crystallographic axis.

4.4.3.3. Surface stabilization effect: dissolution scenario III

The S2 stabilization does not change the surface structure and dissolution mechanism for Q₃ termination. On contrast, we observed a wide range of etch pit morphologies for Q₂ termination (Fig. 4-6). In this case, a unique morphology was obtained for each version of the model and each parameter set. We summarized the observations regarding etch pit shape and the faces forming these pits in Tables 4-2a and 4-2b. A common observation is that the pits produced by FCS and SCS-L1 models are made of rhombohedral faces, while pits with prism faces can be developed using SCS-L2 and SCS-D models. The relative size of the prism faces with respect to the rhombohedral ones can be controlled by varying ΔE_{2g} value (Fig. 4-6D-H; 4-6M-N). We suggest that the appearance and dominance of the prism faces at elevated values of ΔE_{2g} happens because the stability of this face is sensitive to the strength of the intra-surface hydrogen bonds. Therefore, newly forming prism faces can be better stabilized by the increase of this parameter.

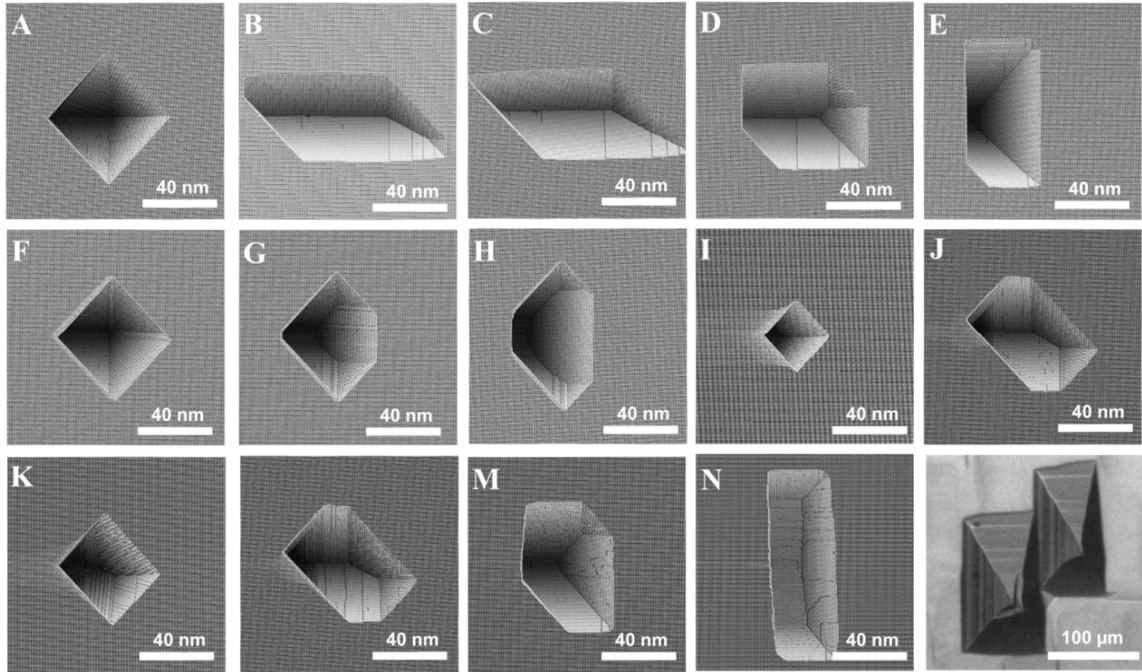


Figure 4-6. **(A)-(N)**: KMC simulations: Etch pits formed at a (100) prism face (starting from Q_2 termination, top layer is frozen, 10^6 atoms removed in each case, the length of the screw dislocation hollow core is 200 unit cells). **A-H**: “Pure water”, various models used (see text); **(A)** FCS model; **(B)** SCS-L1 model; **(C)** SCS-L2 model ($\Delta E_{2g} = 0$ kT); **(D)** SCS-L2 model ($\Delta E_{2g} = 6$ kT) model; **(E)** SCS-L2 model ($\Delta E_{2g} = 10$ kT); **(F)** SCS-D model ($\Delta E_{2g} = 0$ kT); **(G)** SCS-D model ($\Delta E_{2g} = 2$ kT); **(H)** SCS-L2 model ($\Delta E_{2g} = 4$ kT); **I-N**: low activation energy, or “catalyzing” environment, various models used. **(I)** FCS model; **(J)** SCS-L1 model; **(K)** SCS-L2 model ($\Delta E_{2g} = 0$ kT); **(L)** SCS-L2 model ($\Delta E_{2g} = 2$ kT); **(M)** SCS-L2 model ($\Delta E_{2g} = 4$ kT); **(N)** SCS-L2 model ($\Delta E_{2g} = 6$ kT); **(O)*** Rectangular-pyramidal pits formed on the prism faces of quartz etched by KOH (Gratz et al., 1990).

*Reprinted from *Geochimica et Cosmochimica Acta*, Vol 54/Issue 11, Gratz A.G., Bird P. and Quiro G.B. "Dissolution of quartz in aqueous basic solution, 106–236°C: Surface kinetics of "perfect" crystallographic faces", Pages No. 2911-2922 (DOI: doi:10.1016/0016-7037(90)90109-X) Copyright (1990), permission obtained from Elsevier.

The use of SCS-D model applied for “pure water” conditions results in formation of unique asymmetric pits (Figs. 4-6G, 4-6H). The remarkable difference between the pit morphologies obtained using SCS-D and SCS-L2 models at the same conditions clearly indicates that stability of various faces can be very sensitive to the quantitative difference between dissolution probabilities for various surface sites.

Despite the large variety of pit shapes observed in the simulations (Table 4-2 and Fig. 4-6), the number of polyhedral pit shapes discovered in experimental studies is limited. Gratz et al. (1990) observed rectangular-pyramidal pits after etching quartz prism face in KOH (Fig. 4-6O). The same shape was obtained in the simulations for “pure water” conditions, SCS-L2 model (Fig. 4-6E). We suggest that the similarity between the shapes obtained for these two different conditions is caused by similar quantitative relationships between the dissolution probabilities for the most important sites in these two cases. Also, since the prism faces appearing in experimentally obtained pits can be formed in the simulations via increasing strength between surface hydroxyls, we conclude that this effect also plays important role in stabilization of this face.

Table 4-2. Morphological characteristics (shape and composing faces) of polyhedral etch pits formed on Q₂ termination of prism (100) quartz face in KMC simulations. The initial surface was stabilized by S2 method (see description in text), modeling parameters are shown in Table 1. R-rhombohedral; m-prism faces.

(a) “pure water” conditions;

ΔE_{2g} , kT	FCS	SCS-L1	SCS-L2			SCS-D		
			0-4	6	8-10	0	2	4
Shape	Square	Parallelogram	Parallelogram	Pseudo-hexagonal	Rectangular	Square	Pentagonal	Pseudo-hexagonal
Faces	6 R	4 R	4 R	4 R, 2 m	2 R, 2 m	6 R	6 R, 1 m	6 R, 2 m

(b) “catalyzing” conditions.

ΔE_{2g} , kT	FCS	SCS-L1	SCS-L2			
			0	2	4	6
Pit shape	Square	Rectangular	Rectangular	Pseudo-hexagonal	Pseudo-hexagonal	Rectangular
Faces	4 R	6 R	6 R	6 R	4 R, 2 m	2 R, 3 m

4.4.4. Model complexity: conclusions and prospective

Ability of a KMC model to correctly predict surface morphology, reactivity and net dissolution rates depends on whether or not *all* kinetically important reactions are considered in this model. The surface morphology ultimately controls the probability distribution for surface reactions, since all probabilities in these models are functions of surface site topology. The probability distribution may influence on the reaction order. This order may define surface morphology as well as dynamics of its alteration. Therefore, surface morphology and reaction probability distribu-

tion form a feedback loop according to the scheme: surface structure \rightarrow reactive site distribution \rightarrow probability distribution \rightarrow reaction sequence \rightarrow surface structure.

Since the reaction probability distribution depends on model complexity and the parameter set, the latter two factors may significantly influence on surface morphology. At the same time, the structure of the initial surface and the topology of the Si-site network parallel to the simulated face influence the probability distribution as well.

In this study complexity of a KMC model is defined by setting a threshold for the extent of topological detail about surface sites. For example, FCS model considers only number of bonds at a Si site, while SCS models consider the topology of Si-O-Si bonds binding this Si site to the surface. The number of parameters used to differentiate reactive sites defines the variety of these sites in a KMC model. As a consequence, the amount of topological information about surface sites defines the number of the possible reaction types and the corresponding probability distributions. Description of this network of sites and possible reactions may be necessary for production of accurate simulation results, or conversely may only complicate the simulation algorithm without making any improvement in comparison to a simpler model. Therefore, the key question with respect to this problem is to what extent addition of such details change the probability distribution for all kinetically important reactions, such that new surface morphologies can be formed. This also raises the question of whether these new morphologies are relevant to those observed experimentally. Here we define an optimal model complexity as the mini-

imum detail, e.g. numbers of various neighbors and their contributions to the activation energy for dissolution of a Si-site, necessary for an accurate prediction of the dissolution kinetics. The above simulation results produced using four different models serve as an illustrative example of the derivation of an optimal model complexity for quartz dissolution at far from equilibrium conditions. A very similar approach can be used for the other silicate minerals, with the appropriate inclusion of other chemical elements in different crystallographic coordination, e.g. Al^{3+} , Al^{4+} (as for muscovite, see earlier studies by Kurganskaya and Luttge, 2013), Fe^{2+} , Mg^{2+} , etc.

As we can see for (001) face, the number of model parameters substantially influences the model's ability to produce the range of surface morphologies observed in experiments. The values of the parameters are also important. The most remarkable changes in surface morphology are observed when we vary the value of ΔE_{2g} parameter, considering steric and hydrogen bonding influence on site reactivity. The value of this parameter defines step roughness and curvature.

In contrast, surface morphology of the rhombohedral (101) face does not depend on the model complexity and parameter values. In this case, the topology of the network of (101) surface sites completely defines the available dissolution mechanisms, such that the model complexity and parameter values do not influence the reaction sequence. Thus the dissolution mechanism of this face is determined completely by the crystal structure of this face.

The (100) face can be considered an intermediate case between the two end-member (001) and (101) faces with respect to sensitivity to model complexity. Dis-

solution of (100) face in “pure water” is insensitive to model complexity (Fig. 5A-C) unless surface stabilization is applied to Q_2 termination. At “catalyzing” conditions rectangular etch pits are formed as new steps along [001] direction are stabilized. The overall switch in surface morphology is caused by the change of the reaction probability distributions under these conditions. The [001] and [010] steps are made up of (3,6,0) and (2,4,2) sites correspondingly. The decrease of the contribution of the first order neighbors to the probability of surface site dissolution at “catalyzing” conditions makes dissolution probabilities for these sites comparable, so the frequency of kink site formation at [010] step becomes comparable to those for [001] step. The aspect ratio of these pits depends on the values of ΔE_{2l} and ΔE_{2g} parameters. These parameters define relative velocities for the steps moving along [010] and [001] directions through their influence on kink site nucleation and propagation rates. A significant change was observed when stabilization was applied to Q_2 termination of this face. This effect causes formation of a large spectrum of new pit shapes that are extremely sensitive to model complexity and parameter values (Fig. 4-6 and Table 4-2). The case of the (100) face illustrates the fact that the probability distribution may exhibit substantial dependency on model complexity and parameter values in only specific areas of the parametric field.

According to these observations, the complexity and parameter values of a KMC model play a crucial role in its ability to produce observed surface morphologies. In some cases these factors may not be important (as in case of (101) face)). However, general consideration of the second-order neighbors connected either via direct Si-O-Si links or Si-OH..O-Si bonds, as well as surface stabilization effects in-

duced by the surface water structure in the KMC models, plays a vital role in determining the correct order of surface reactions. Consideration of the intrasurface hydrogen bonding is of particular importance here, because this bonding plays a crucial role for stabilization of prism and basal faces of quartz (Murashov, 2005). In our KMC models the influence of this bonding is considered by assigning ΔE_{2g} parameter to the sites having “disconnected” second-order neighbors. Because surface hydrogen bonding network can be perturbed by the presence of water ions (Kubicki et al., 2012), this parameter should depend on environmental conditions. As a consequence, the surface morphology and etch pit structure would also depend on environmental conditions, because of both ligand or charge-promoted decrease of activation energy for bond hydrolysis, as well as the effects of solvent composition on surface hydrogen bond network.

Parameters additional to those described here should also be incorporated into simulation algorithms. These factors include surface site charge distribution as a function of pH conditions (Morrow et al., 2009), chemistry and coordination of the surface sites, influence of alkali ions on the structure and reactivity of the mineral-water interface (Kubicki et al., 2012), the kinetic relationships between the structure of particular mineral faces and water layers (Murashov, 2005; Yang and Wang, 2006). Particular attention should be given to the quantitative influence of these factors to the activation energies of surface sites dissolution. These activation energies can be derived from *ab initio* and MD calculations using realistic models of the silicate-water interface. An important step in this approach would be characterization of the key surface features, e.g. step and kink sites.

4.5. Conclusions

The KMC method can successfully predict a vast range of dissolution morphologies for various faces of the quartz crystal. It can be used as a powerful tool for the recognition of important aspects of the dissolution mechanisms and their controls with molecular resolution at various environmental conditions. The lattice resistance effect, surface hydrogen bonding network, and surface stabilization effects substantially influence the reactivity of the surface sites of silicates and must be considered in KMC algorithms. Parameters for the probability equations ideally should be obtained from the corresponding *ab initio* calculations for all kinetically important surface sites. If such theoretical data are not available, we may utilize functional approximations using numbers of influential surface groups as arguments and some energetic constants as variable parameters. This approach generally produces satisfactory results. However, in some specific cases more detailed knowledge about the dissolution rate at particular sites may be also required.

4.6. Acknowledgements

We would like to thank Dr. Cornelius Fischer for his help in revising and improving the manuscript. Also, we thank James Keenan who proofread this manuscript and made linguistic corrections. We acknowledge generous support from the Global Climate and Energy Project (GCEP) at Stanford University (award # 25580430-48513-A).

4.7. References

- Aldushin K., Jordan G. and Schmahl W.W. (2006) Kinematics of apophyllite leaching- A terrace-ledge-link process within phyllosilicate interlayers. *J. Cryst. Growth* **297**, 161-168.
- Blum A.E. and Lasaga A.C. (1987) Monte Carlo Simulations of Surface Reaction Rate Laws, in *Aquatic surface chemistry* (John Wiley & Sons, 1987), 255-292.
- Bortz A.B., Kalos M.H., and Lebowitz J.L. (1975) A new algorithm for Monte Carlo simulation of Ising spin systems. *J. Comp. Phys.* **17**, 10-18.
- Brantley S.L., Crane S.R., Crerar D.A., Hellmann R. and Stallard R. (1986) Dissolution at dislocation etch pits in quartz. *Geochim. Cosmochim. Acta* **50**, 2349-2361.
- Chuvyrov A.N. and Mazitov R.M. (2008) Structure and properties of quartz crystals grown from fluoride solutions: I. The Morphology of Basal Pinacoidal Habit. *Crystallography Reports* **53**, 894-899.
- Criscenti L. J., Kubicki J.D. and Brantley S.L. (2006) Silicate glass and mineral dissolution: calculated reaction paths and activation energies for hydrolysis of a Q³Si by H₃O⁺ using ab initio methods. *J. Phys. Chem. A* **110**, 198-206.
- de Leew, N. H., Higgins, F.M. and Parker, S.C. (1999) Modeling the surface structure and stability of alpha-quartz. *J. Phys. Chem. B* **103**, 1270-1277.
- Dkhissi A., Esteve A., Mastail C., Olivier S., Mazaleyrat G., Jeloica L. and Rouhani M.D. (2008) Multiscale modeling of the atomic layer deposition of HfO₂ thin film grown

on silicon: how to deal with a Kinetic Monte Carlo procedure. *J. Chem. Theor. Comp.* **4**, 1915-1927.

Du Z. and de Leuw N.H. (2006) Molecular dynamics simulations of hydration, dissolution and nucleation processes at the α -quartz (0001) surface in liquid water. *Dalton Trans.* **22**, 2623-2634.

Iwasaki F. (1977) Line defects and etch tunnels in synthetic quartz. *J. Cryst. Growth* **39**, 291-298.

Ferrando N., Gosálvez M.A. and Colóm L.J. (2012) Evolutionary continuous cellular automaton for the simulation of wet etching of quartz. *J. Micromech. Microeng.* **22**, 025021.

Fischer C., Arvidson R.S. and Lutge A. (2012) How predictable are dissolution rates of crystalline material? *Geochim. Cosmochim. Acta* **98**, 177-185.

Gilmer G.H. (1980) Computer models of crystal growth. *Science* **208**, 355-363.

Gratz A.J., Bird P. and Quiro G.B. (1990) Dissolution of quartz in aqueous basic solution, 106-236°C: Surface kinetics of "perfect" crystallographic faces. *Geochim. Cosmochim. Acta* **54**, 2911-2922.

Kohli C.S. and Ives M.B. (1972) Computer simulation of crystal dissolution morphology. *J. Cryst. Growth* **16**, 123-130.

Kubicki, J.D., Sofo, J.O., Skelton, A.A. and Bandura, A.V. (2012) A new hypothesis for the dissolution mechanism of silicates. *J. Phys. Chem. C*, **116**, 17479-17491.

Kurganskaya I., Arvidson R.S., Fischer C. and Luttge A. (2012) Does the stepwave model predicts mica dissolution kinetics? *Geochim. Cosmochim. Acta* **97**, 120-130.

Kurganskaya I. and Luttge A. (2013) A comprehensive stochastic model of phyllosilicate dissolution: structure and kinematics of etch pits formed on muscovite basal face. *Geochim. Cosmochim. Acta*, in press

Kuwahara Y., Uehara S. and Aoki Y. (1998) Surface microtopography of lath-shaped hydrothermal illite by Tapping Mode and Contact Mode AFM. *Clays Clay Miner.* **46**, 547-582.

Lasaga A. C. and Luttge A. (2001) Variation of crystal dissolution rate based on dissolution stepwave model. *Science* **23**, 2400-2404.

Lasaga A.C. and Luttge A. (2004) Mineralogical approaches to fundamental crystal dissolution kinetics. *Amer. Mineral.* **89**, 527-540.

Luttge A. (1995) in *Habilitationsschrift "Untersuchungen zur Kinetik von Mineral- und Austauschreaktionen"* (Institut für Mineralogie, Petrologie und Geochimie, Wilhelmstraße 56, 72074 Tübingen), **1995**, p. 62.

Luttge A., Arvidson R.S. and Fischer C. (2013) A stochastic treatment of crystal dissolution kinetics. *Elements* **9**, 177-182.

Meakin P. and Rosso K. M. (2008) Simple kinetic Monte Carlo models for dissolution pitting induced by crystal defects. *J. Chem. Phys.* **129**, 204106.

Morrow C. P., Nangia S. and Garrison B. J. (2009) Ab initio investigation of dissolution mechanisms in aluminosilicate minerals. *J. Phys. Chem. A* **113**, 1343-1352.

Murashov V.V. (2005) Reconstruction of pristine and hydrolyzed quartz surfaces. *J. Phys. Chem. B* **109**, 4144-4151.

Nangia, S. and Garrison, B. J. (2009) Advanced Monte Carlo approach to study evolution of quartz surface during the dissolution process. *J. Am. Chem. Soc.* **131**, 9538-9546.

Nangia S. and Garrison B. J. (2010) Role of intrasurface hydrogen bonding on silica dissolution. *J. Phys. Chem. C* **114**, 2267-2272.

Neumann U. and Luttge A. (1995) Mechanism and kinetics of a decarbonation reaction: A comparison of single crystal experiments with powder and rock cylinder experiments, in *Habilitationsschrift "Untersuchungen zur Kinetik von Mineral- und Austauschreaktionen"*, (Institut für Mineralogie, Petrologie und Geochemie, Wilhelmstraße 56, 72074 Tübingen), p. 146.

Nielsen J.W. and Foster F.G. (1960) Unusual etch pits in quartz crystals. *Am. Mineral.* **45**, 299-310.

Nijdam A.J., van Veenendaal E., Cuppen H. M., van Suchtelen J., Reed M. L., Gardeniers J. G. E., van Enckevort W. J. P., Vlieg E. and Elwenspoek M. (2001) Formation and stabilization of pyramidal etch hillocks on silicon {100} in anisotropic etchants: Experiments and Monte Carlo simulation. *M. J. Appl. Phys.* **89**, 4113.

Oelkers E.H., Schott J., Gauthier J.-M., and Herrero-Roncal T. (2008) An experimental study of the dissolution mechanism and rates of muscovite. *Geochim. Cosmochim. Acta* **72**, 4948-4961.

Ostapenko G.T. and Mitsyuk B.M. (2006) Asymmetry of growth and dissolution on basal, minor rhombohedral and prism faces of quartz. *J. Cryst. Growth* **294**, 330-338.

Patel A.R., Bahl O.P. and Vagh A.S. (1965) Etching of rhombohedral cleavages of quartz. *Acta Cryst.* **19**, 757-758.

Pelmenschikov A., Strandh H., Pettersson L.G.M. and Leszczynski J. (2000) Lattice Resistance to Hydrolysis of Si-O-Si bonds of silicate minerals: *ab initio* calculations of a single water attack onto the (001) and (111) β -cristobalite surfaces. *J. Phys. Chem. B* **104**, 5779-5783.

Piana S., Reyhani M. and Gale J.D. (2005) Simulating micrometer-scale crystal growth from solution. *Nature* **438**, 70-3.

Piana S. and Gale J.D. (2006) Three-dimensional kinetic Monte Carlo simulation of crystal growth from solution. *J. Cryst. Growth* **294**, 46-52.

Rignanese G.-M., De Vita A., Charlier J.-C., Gonze X. and Car R. (2000) First-principles molecular-dynamics study of the (0001) α -quartz surface. *Phys. Rev. B* **61**, 13250-13255.

Sangwal, K. (1987) *Etching of crystals: theory, experiment, and application* (North-Holland pub.), in Defects and Solids series (ed. S.Amelinckx-J.Nihoul), **15**, pp. 22-23; p. 89.

Schlegel M.L., Nagy K.L., Fenter P. and Sturchio N.C. (2002) Structures of quartz (1010)-and (1011)-water interfaces determined by X-ray reflectivity and atomic force microscopy of natural growth surfaces. *Geochim. Cosmochim. Acta.* **66**, 3037-3054.

Schulz M. S. and White A. F. (1999) Chemical weathering in a tropical watershed, Luquillo Mountains, Puerto Rico III: Quartz dissolution rates. *Geochim. Cosmochim. Acta.* **63**, 337-350.

Suzuki T., Sugihara N., Teshima K., Oishi S. and Kawasaki M. (2009) Specific surface free energy and etch pit density of synthesized quartz crystal. *J. Cryst. Growth* **311**, 719–721.

Voter A.F. (2007) Introduction to the Kinetic Monte Carlo method” in “*Radiation Effects in Solids*” (ed. K.E. Sickafus and E.A. Kotomin), *NATO Science Series* 235, 1.

Wallace A. F., Gibbs G.V., and Dove P. M. (2010) Influence of ion-associated water on the hydrolysis of Si-O bonded interactions. *J. Phys. Chem. A* **114**, 2534–2542.

Wang J., Kalinichev A.G. and Kirkpatrick R.J. (2006) Asymmetric hydrogen bonding and orientational ordering of water at hydrophobic and hydrophilic surfaces: A comparison of water/vapor, water/talc, and water/mica interfaces. *Geochim. Cosmochim. Acta.* **70**, 562.

Wang J., Kalinichev A.G. and Kirkpatrick R.J. (2009) Effects of substrate structure and composition on the structure, dynamics and energetics of water on mineral surfaces: a molecular dynamics modeling study. *J. Phys. Chem. C* **113**, 11077.

Wegner M.W. and Christie J.M. (1983) Chemical etching of deformation substructures in quartz. *Phys. Chem. Minerals* **9**, 67-78.

Wehrli B. (1989) Monte Carlo Simulations of Surface Morphologies during Mineral Dissolution. *J. Colloid Interface Sci.* **132**, 230-242.

Yanina S.V., Rosso K. M. and Meakin P. (2006) Defect distribution and dissolution morphologies on low-index surfaces of α -quartz. *Geochim. Cosmochim. Acta.* **70**, 1113-1127.

Yang J., Meng S., Xu L.F. and Wang E.G. (2004) Ice tessellation on a hydroxylated silica surface. *Phys. Rev. Lett.* **92**, 146102.

Yang J. and Wang E.G. (2006) Water adsorption on hydroxylated α -quartz (0001) surfaces: From monomer to flat bilayer. *Phys. Rev. B* **73**, 035406.

Xiao Y. and Lasaga A. C. (1994) Ab initio quantum mechanical studies of the kinetics and mechanisms of silicate dissolution: $H^+(H_3O^+)$ catalysis. *Geochim. Cosmochim. Acta* **58**, 5379-5400.

Xiao, Y. and Lasaga, A.C. (1996) Ab initio quantum mechanical studies of the kinetics and mechanisms of quartz dissolution: OH^- catalysis. *Geochim. Cosmochim. Acta.* **60**, 2283-2295.

Zhang L. and Luttge A. (2009) Morphological evolution of dissolving feldspar particles with anisotropic surface kinetics and implications for dissolution rate normalization and grain size dependence: A kinetic modeling study. *Geochim. Cosmochim. Acta* **73**, 6757-6770.

Chapter 5

Summary and Conclusions

In this work I used experimental studies and *ab-initio* powered Kinetic Monte Carlo simulations as complimentary tools combined into a multi-scale approach to study silicate dissolution kinetics. I used muscovite and quartz as representatives of phyllosilicate and tectosilicate groups.

The results of experimental observations lead to the following conclusions about phyllosilicate dissolution kinetics:

1. Dissolution of phyllosilicate minerals takes place at both basal and edge faces. Screw dislocations formed during phyllosilicate mineral growth cause the formation of etch pits on basal faces. Stepwaves emanating from the opened hollow cores dissolve the phyllosilicate minerals in a process of multiple step movements. In combination with stepwave annihilation, this process causes surface normal retreat. The same stepwave mechanism (Lasaga and Luttge,

2001) controls the dissolution of framework silicates, e.g., feldspars (Beig and Luttge, 2006; Zhang and Luttge, 2007; 2008a; b; 2009) and quartz (Yani-na et al., 2006).

2. Surface roughness and reactivity of dissolving muscovite basal face change both in space and time. This spatio-temporal heterogeneity is common for many minerals, e.g., calcite (Arvidson et al., 2003; Fischer et al., 2012), and considered to be an inherent property of crystalline systems (Luttge et al., 2013).
3. Reactivity of the $\{hk0\}$ edge faces of phyllosilicates depends on the face index. Differential reactivity of $\{hk0\}$ faces is reflected in velocity anisotropy of the steps formed on muscovite basal face. At basic pH conditions, the most stable steps run along the $[110]$ direction in even (upper) layers and along $[1\bar{1}0]$ direction in even (lower) layers of the $2M_1$ polytype. The other stable but faster steps are formed along the $[100]$ and $[1\bar{1}0]$ directions within the same layer. Steps that are rotated by 120 degrees are stable in the odd layer.

The connection between the dissolution reaction taking place at the muscovite surface, etch pits, and step structures was studied by using computer simulations.

I developed a general Kinetic Monte Carlo (KMC) model of phyllosilicate dissolution and applied it to the mica structure. I utilized similar reaction probability

formulations described in Zhang and Luttge (2007; 2008a; b; 2009), Lasaga and Luttge (2004a; b). A sequence of different model versions considered an increasing number of details that I used to differentiate between surface sites. I wrote all programs in Fortran90. Then, I compared the surface morphologies produced with the simulations with my experimental results. Below are the main conclusions:

4. Simulation results for muscovite dissolution agreed fully with the stepwave mechanism that we derived earlier from our experimental studies.
5. The correct etch pit orientation can be achieved if we use activation energies of bond hydrolysis calculated for alkaline conditions by Morrow et al. (2009) [applied to the most simple model and considering the first coordination sphere, only].
6. The additional stable steps along $[100]$ and $[1\bar{1}0]$ directions observed in experiments can be generated with simulations, only if we consider the influence of the second-order neighbors on the activation energies of surface site dissolution.
7. Also, analysis of the step and kink site topologies along $[100]$ and $[1\bar{1}0]$ steps shows that the kinetic difference between dissolution rates of step and kink sites may exist only if we consider second coordination sphere influence.
8. A variety of kink and step sites with different topology and reactivity exists on the phyllosilicate surface. The differences in kink site formation and prop-

agation rates along different steps define step velocity anisotropy within mica layers.

9. Finally and most importantly, KMC methods combined with experimental observations can be used as a powerful tool for the recognition of important kinetic controls of silicate dissolution.

The results of the KMC simulations showed that the values of bond hydrolysis activation energies used as model parameters substantially influence, both, the etch pit morphology and the relative step velocities. This conclusion was an important prerequisite that allowed me to conduct the next study that was focused on the problem of model parameterization and the use of optimal model complexity.

In order to evaluate these issues, I developed four KMC models of quartz dissolution and tested their individual ability to reproduce experimental data from the literature. The models differ by the degree of complexity and/or by the number of parameters used to differentiate the surface sites. I simulated the dissolution of (001) basal, (100) prism and (101) rhombohedral faces of quartz by using all four models implemented in Fortran90 programs. In addition, I run calculations for initially “frozen” faces in order to test the influence of surface stabilization effects on the dissolving surface morphology. The simulation results showed the following:

1. The number and values of parameters in KMC models substantially influence the surface morphology and structure of etch pits.

2. Only models with increased complexity possess the ability to produce the various surface morphologies observed in experiments at different environmental conditions.
3. It is important to differentiate between two types of second-order neighbors-connected via direct Si-O-Si bonds or via hydrogen or hydroxyl bonds. As in the case of mica, the topology of the surface sites plays a key role in their reactivity.
4. The hydrogen bonding between surface hydroxyls seems to substantially influence the stabilization of steps and faces.
5. Surface stabilization effects can be very important in order to reproduce experimentally observed dissolution patterns. Therefore, additional corrections to the site reactivity are necessary.

My work demonstrates the effectiveness of our multi-scale approach for a much more comprehensive understanding of silicate dissolution kinetics. KMC methods can be used to establish a connection between the surface reactions at the molecular scale, the formation of steps and etch pits, stepwave propagation, and resulting etch pit morphologies. AFM observations of step and pit structures can test the correctness of model predictions and parameterization schemes. Surface topography measurements at larger scales conducted with VSI provide additional important kinetic information about the spatial distribution of surface reactivity and the temporal alteration of morphologies.

I suggest that a future development of this multi-scale approach should focus on the following problems:

1. The sources of spatial reactivity variance.
2. The correct timing of KMC surface reactions and calculation of the dissolution rates.
3. Estimation of bond hydrolysis activation energies for all kinetically important sites calculated by using *ab initio* and MD methods, e.g., step and kink sites having various topological characteristics. Long-range order neighbors, surface stabilization, structure of bonding network with water should be taken in account.
4. The problem of optimal model complexity is still not fully solved and requires further work including but not limited to the implementation of surface charge distribution (pH influence, see Nangia and Garrison, 2010), perturbation of the hydrogen bonding network by alkali ions (Kubicki et al., 2012), the influence of saturation state, and bond order-disorder phenomena (e.g., Zhang and Luttge, 2007).
5. A parallel implementation of the KMC algorithms should help to solve the problem of limited system size and substantially boost the development of multi-scale approaches.

5.1. References

Arvidson R.S., Ertan I.E., Amonette J.E. and Luttge A. (2003) Variation in calcite dissolution rates: A fundamental problem? *Geochim. Cosmochim. Acta* **67**, 1623–1634.

Beig M.S. and Luttge A. (2006) Albite dissolution kinetics as a function of distance from equilibrium: Implications for natural feldspar weathering. *Geochim. Cosmochim. Acta* **70**, 1402–1420.

Fischer C., Arvidson R.S. and Luttge A. (2012) How predictable are dissolution rates of crystalline material? *Geochim. Cosmochim. Acta* **98**, 177-185.

Kubicki, J.D., Sofo, J.O., Skelton, A.A. and Bandura, A.V. (2012) A new hypothesis for the dissolution mechanism of silicates. *J. Phys. Chem. C*, **116**, 17479-17491.

Lasaga A. C. and Luttge A. (2001) Variation of crystal dissolution rate based on dissolution stepwave model. *Science* **23**, 2400-2404.

Lasaga A.C. and Luttge A. (2004a) Mineralogical approaches to fundamental crystal dissolution kinetics-Dissolution of an A3B structure. *Eur. Jour. Miner.* **16**, 713-729.

Lasaga A.C. and Luttge A. (2004b) Mineralogical approaches to fundamental crystal dissolution kinetics. *Amer. Mineral.* **89**, 527-540.

Luttge A., Arvidson R.S. and Fischer C. (2013) A stochastic treatment of crystal dissolution kinetics. *Elements*, **9**, 177-182.

Morrow C.P., Nangia S., and Garrison B.J. (2009) Ab Initio Investigation of Dissolution Mechanisms in Aluminosilicate Minerals. *J. Phys. Chem. A* **113**, no. 7, 1343-1352.

Nangia S. and Garrison B.J. (2010) Theoretical advances in the dissolution studies of mineral-water interfaces. *Theoretical Chemistry Accounts* **127**, 271-284.

Yanina S.V., Rosso K. M. and Meakin P. (2006) Defect distribution and dissolution morphologies on low-index surfaces of α -quartz. *Geochim. Cosmochim. Acta.* **70**, 1113-1127.

Zhang L. and Luttge A. (2007) Al,Si order in albite and its effect on albite dissolution process: A Monte Carlo study. *Amer. Mineral.* **92**, 1316-1324.

Zhang L. and Luttge A. (2008) Aluminosilicate dissolution kinetics: A general stochastic model. *J. Phys. Chem. B* **112(6)**, 1736-1742.

Zhang L. and Luttge A. (2009a) A general kinetic model of plagioclase dissolution. *Geochim. Cosmochim. Acta* **73**, 2832-2849.

Zhang L. and Luttge A. (2009b) Morphological evolution of dissolving feldspar particles with anisotropic surface kinetics and implications for dissolution rate normalization and grain size dependence: A kinetic modeling study. *Geochim. Cosmochim. Acta* **73**, 6757-6770.